NOVEL SMART MODULES FOR IMAGING, COMMUNICATIONS, AND DISPLAYS

by

PHILIP JOHN MARRACCINI

B.Sc. (Hons.) University Central Florida, 2008

M. Sc. CREOL, University of Central Florida, 2010

A dissertation submitted in partial fulfilment of the requirements

for the degree of Doctorate of Philosophy

in the Department of Electrical and Electronic Engineering

at the National University of Ireland, Cork, Ireland

June 2013

Head of Department and Major Supervisor:

Professor Nabeel A. Riza

Contents

philipmarraccini@ieee.org

The thesis submitted is the candidate's own work and has not been submitted for another degree, either at University College Cork or elsewhere.

Signature: _____ Date: _____

ABSTRACT

This dissertation proposes and demonstrates novel smart modules to solve challenging problems in the areas of imaging, communications, and displays. The smartness of the modules is due to their ability to be able to adapt to changes in operating environment and application using programmable devices, specifically, electronically variable focus lenses (ECVFLs) and digital micromirror devices (DMD). The proposed modules include imagers for laser characterization and general purpose imaging which smartly adapt to changes in irradiance, optical wireless communication systems which can adapt to the number of users and to changes in link length, and a smart laser projection display that smartly adjust the pixel size to achieve a high resolution projected image at each screen distance.

The first part of the dissertation starts with the proposal of using an ECVFL to create a novel multimode laser beam characterizer for coherent light. This laser beam characterizer uses the ECVFL and a DMD so that no mechanical motion of optical components along the optical axis is required. This reduces the mechanical motion overhead that traditional laser beam characterizers have, making this laser beam characterizer more accurate and reliable. The smart laser beam

characterizer is able to account for irradiance fluctuations in the source. Using image processing, the important parameters that describe multimode laser beam propagation have been successfully extracted for a multi-mode laser test source. Specifically, the laser beam analysis parameters measured are the M^2 parameter, w_0 the minimum beam waist, and z_R the Rayleigh range. Next a general purpose incoherent light imager that has a high dynamic range (>100 dB) and automatically adjusts for variations in irradiance in the scene is proposed. Then a data efficient image sensor is demonstrated. The idea of this smart image sensor is to reduce the bandwidth needed for transmitting data from the sensor by only sending the information which is required for the specific application while discarding the unnecessary data. In this case, the imager demonstrated sends only information regarding the boundaries of objects in the image so that after transmission to a remote image viewing location, these boundaries can be used to map out objects in the original image.

The second part of the dissertation proposes and demonstrates smart optical communications systems using ECVFLs. This starts with the proposal and demonstration of a zero propagation loss optical wireless link using visible light with experiments covering a 1 to 4 m range. By adjusting the focal length of the ECVFLs for this directed line-of-sight link (LOS) the laser beam propagation parameters are adjusted such that

the maximum amount of transmitted optical power is captured by the receiver for each link length. This power budget saving enables a longer achievable link range, a better SNR/BER, or higher power efficiency since more received power means the transmitted power can be reduced. Afterwards, a smart dual mode optical wireless link is proposed and demonstrated using a laser and LED coupled to the ECVFL to provide for the first time features of high bandwidths and wide beam coverage. This optical wireless link combines the capabilities of smart directed LOS link from the previous section with a diffuse optical wireless link, thus achieving high data rates and robustness to blocking. The proposed smart system can switch from LOS mode to Diffuse mode when blocking occurs or operate in both modes simultaneously to accommodate multiple users and operate a high speed link if one of the users requires extra bandwidth. The last part of this section presents the design of fibre optic and free-space optical switches which use ECVFLs to deflect the beams to achieve switching operation. These switching modules can be used in the proposed optical wireless indoor network.

The final section of the thesis presents a novel smart laser scanning display. The ECVFL is used to create the smallest beam spot size possible for the system designed at the distance of the screen. The smart laser scanning display increases the spatial resolution of the display for any given distance. A basic smart display operation has been tested for

red light and a 4X improvement in pixel resolution for the image has been demonstrated.

To my parents, Philip Marraccini and Patricia Marraccini,

and my grandparents,

Philip and Mary Marraccini and Walter and Ginny Keller.

ACKNOWLEDGEMENTS

First of all I would like to thank my family. The biggest thanks go to my parents, Philip and Patricia Marraccini, for all their love, guidance, and support. Without them I would not have been able to make it to where I am today. Thank you for your constant encouragement and advice. I would also like to thank my sisters Christina and Michelle. I am grateful to my grandparents for guiding me and instilling me with a passion for learning. I would also like to thank my Aunt Flip and Aunt Norma whom are very dear to me and watched over me when I was in Orlando. I also thank Uncle Ron and Aunt Jane for all their support throughout the years. Thank you to the rest of my family for being an important part of my life. I love all of you.

Next I would like to thank my advisor, Professor Nabeel A. Riza, for his guidance and support since I first walked into his undergraduate class over 5 years ago. He has watched over me during my Ph. D degree and made sure he did everything he could to make sure I received my degree. I thank him his guidance to apply for an internship at General Electric, bringing me to Ireland to setup a new lab at the University College Cork, and his patience throughout my studies. I also would like to thank fellow workers past and present in the group, Dr. Mumtaz Sheikh, Dr. Syed Azer Reza, and Muhammad Junaid Amin for their help, support, and friendship. I would like to thank Mumtaz and Azer for reminding me that I needed to take breaks from work and forcing me out of the lab to relax. I also thank them for their contributions to my thesis and the work I did with them. I thank Dr. Nader Behdad, Dr. Rajesh Paryani, Dr. Mudar Al-Joumayly, and the UCF RF Lab for teaching me microwave engineering, antenna design, and electromagnetics.

Thank you to all my colleagues at UCF and UCC. I thank Rachel Franzetta at the University of Central Florida (UCF) for her hard work and friendship. Without our second “mom” looking out for us at CREOL we would be lost. I am thankful to my professors from UCF for their instruction, especially, Professors Ron Eaglin, Sergey Stolbov, Demetrios Christodoulides, Ayman Abouraddy, Boris Zeldovich, and Jim Moharam. I thank all the students I helped in their coursework for giving me the opportunity to improve my teaching skills. Next I thank Geraldine Mangan, Niamh O’Sullivan, Mary Costello, Ralph O’Flaherty, Michael O’Shea and Timothy Powers for their help at UCC. I thank Prof. Domenico Zito, Prof. Nabeel A. Riza, Prof. Michael Peter Kennedy, and Dr. Alan Morisson for their support of the UCC IEEE Student Branch. I would like to thank Firecomms, Dr. Frank Peters, and Dr. Kevin

McCarthy for hardware used to perform the experiments in Chapter 6. I would also like to thank my thesis committee Prof. Michael Peter Kennedy from UCC and Prof. Harm Dorren from the Eindhoven University of Technology.

Next, I would like to thank General Electric Research and Development in Niskayuna for a wonderful internship experience and all that I learned. I would like to thank everyone there for their help. I am especially thankful to the Photonics Lab, my project partners, and the other interns for their friendship and fruitful discussions. I would also like to thank Mr. Silva and Mrs. Silva for welcoming me to Schenectady and for their friendship throughout. I thank First Presbyterian Church in Schenectady for their support during this time.

I give special thanks to Frank Peters and Jo Peters for all their guidance and support. Thank you for your friendship, welcoming me to Cork, your help during tough times, and all the hard work you do for others. Thank you to Nick, Jonathan, Sarah, Matthew, and Timothy for their friendship. Thank you to my friends Branden and Maggie Bettger, John Benzie, Martinus Meela, and the UCCCU for their help.

I would like to thank the rest of my friends whom also hold a special place in my heart and mind. Sadly, there is not space to mention you all, but thank you to all of the UCF Swing Knights for the wonderful dances and times. Thank you to my friends whom inspired and encourage me. To all of my friends from high school and college thank you for your continued friendship. Thank you to Jonathan and Cristina Bravo, Becky and Luis Markovich, Anna Scharnagl, Merrick Hurst, Stef Kanipe, Lydia Fernandez, Cynthia Llegra, Laura Hernandez, Monica Hernandez, Erik Horne, Lane and Lauren Martin, Umar Piracha, Rehan Ahmed, Sonny Vo, Aly Megahed, and Jonathan Hamilton. Special thanks to my housemates in Orlando, Gerard Pianta and Kumel Kawagala. Being able to live with good friends spoiled me. Lastly, I am thankful to my friend Christian Mendoza. You made life much more enjoyable and more importantly were there to point out the many times when I was being stubborn. I greatly appreciate and value your friendship.

,

This velocity is so nearly that of light, that it seems we have strong reason to conclude that light itself (including radiant heat, and other radiations if any) is an electromagnetic disturbance in the form of waves propagated through the electromagnetic field according to electromagnetic laws.
James C. Maxwell

God said, "Let there be light," and there was light.
Genesis 1:3

NOVEL SMART MODULES FOR IMAGING, COMMUNICATIONS, AND DISPLAYS

CHAPTER 1

INTRODUCTION

Light has long been of interest to human beings. Some ancient civilizations worshiped the sun and the stars while others thought they were connected to their ancestors through them. People wondered why the sun was brighter than the moon. They contemplated why perfectly straight objects seem bent if you put them partway underwater. Questions continued such as: What is light? How is light generated? When was it made? Does gravity affect light? As time has passed we have gained more and more understanding of light. Maxwell predicted that light was an electromagnetic wave and then in the 20th century with the theory of relativity, quantum theory, and modern cosmology many more questions were answered. Today, with our current understanding we know that light is quantized, that it has a wave-particle duality, and that the four fundamental forces of nature originated much less than a second after the Big Bang. More about the nature of light is still being discovered, but during the past 150 years our understanding of its nature

has greatly advanced. With this increased understanding so have the applications using light.

This leads to discussing photonics systems, which we will broadly use to describe any light based system. They are used in a wide variety of applications including imaging, communications, displays, sensing, biology, healthcare, and test and measurement systems. Specifically, this dissertation presents novel smart photonic modules for the following areas: imaging, communications, and displays. The modules demonstrated are designed to smartly adapt to changes in the operating environment and application. The modules achieve their smartness by using programmable devices, specifically, an Electronically Variable Focus Lens (ECVFL) and a Digital Micromirror Devices (DMD).

Electrowetting ECVFLs have found their use in cell phone cameras and the DMD is commercially used in high definition (HD) televisions and projection systems. Thus these devices are already known to have good reliability and repeatability. The success of these devices has also led to their proposal for use in other applications. DMDs have been proposed for use in modules for imaging, communication, sensors, test and measurement [1], [2], [3], [4], [5], [6], [7], [8]. ECVFLs have been proposed for use in modules for communication, optical networks, remote sensing, and test and measurement [6] - [9], [10]. This dissertation presents additional applications in which the use of ECVFLs

and DMDs are useful. The dissertation is separated into three sections discussing: Novel Smart Modules for Imaging, Novel Smart Modules for Communications, and Novel Smart Modules for Displays. A brief introduction for these sections follows and also gives a brief overview of the contents of each chapter.

1.1 Novel Smart Modules for Imaging

Some roots of modern imaging date back to ancient Greece. In about 300 B.C. Euclid published his work Catoptrics. Here he observed that refraction occurred, but he could not explain it. However, he was able to come up with the law of reflection which states that the angle of incidence is equal to the angle of reflection [11]. A few centuries later, Alhazen made great strides in understanding the field of imaging and laid the groundwork that enabled the advancements in optics that were made in Medieval Europe [11]. For his valuable contributions to the field he is known as the "Father of Modern Optics." The imaging equation was derived by Isaac Newton around 1670, enabling easier optical system design [11]. Eventually, the first imagers that could transfer the image to a "permanent medium" were demonstrated. In 1802 Thomas Wedgewood used silver nitrate to transfer images onto a "permanent medium" [12]. While there is still debate among researchers as to whether Thomas Wedgewood was able to "permanently" fix images using the process he developed, by 1827 Nicéphore Niépce had

developed a process of “permanently” fixing images on a medium [13]. Photography was a niche area for the following years, since it was highly specialized. In 1888 this started to change when George Eastman introduced the first easy-to-use consumer camera. This camera used roll film and was able to take 100 photographs before being sent for development [14]. It was not too long until systems which converted photons to electrical signals were developed, such as the camera tube [15], [16], [17] and later the silicon pn junction photo-diode in 1940 [18]. The charge coupled device (CCD) imager was invented in AT&T Bell Labs during 1969 [19] and followed years later by the complementary metal oxide semiconductor (CMOS) imager in the early 1990s [20], [21]. Today these two sensors are still the dominant ones used in digital camera systems.

While the CMOS imager and CCD imager work well, they have a few problems in some applications. The CCD imager has a limited dynamic range. While attenuators can be used to reduce the irradiance of the scene they can distort the image and if used for high powered laser beams, thermal lensing can occur. Additionally, this does not solve the problem of having a high dynamic range in a single scene (it just provides an irradiance offset) where there is an extremely bright object along with an extremely dark object. In such cases, all values above the dynamic range of the CCD will be truncated while those below the

dynamic range will register as noise. Thus detail of the scene is lost. While signal processing helps to improve the quality of images, these details cannot be recovered since the data about irradiance at the high or low levels is lost. Additionally, CCD imagers suffer from “spillover.” This happens when the electrons from one pixel spill over to the adjacent one. This can cause neighboring pixels to register incorrect irradiance values. CMOS imagers, on the other hand, have a high dynamic range. However, they have more advanced circuitry and newer ones required modifying the standard CMOS process making them more expensive [22]. They also suffer from pixel offset since each pixel (or groups of pixels) has its own amplifier. CCD and CMOS imagers are also narrowband devices and can be costly devices.

Another type of imaging system, the optical-mechanical line scanning camera, was originally developed for lunar imaging [23], [24]. Lunar imaging required cameras that had a high dynamic range. Additionally, a small bandwidth and memory storage space were required for lunar imaging [23]. As seen in Fig. 1.1 these devices contained a point photosensor, a lens for collecting light, and a scanning mechanism. In Fig. 1.1 the scanning mirror would be tilted to scan a line, then the system rotated and the next line scanned, and this would continue similar to raster scanning in television sets. The irradiance at each point would be transmitted and the whole image would be constructed once the

scanning was done. Using photo-diodes, a high dynamic range can easily be achieved. Low data rates and a small amount of memory storage are needed for this type of camera since the information for each pixel can be sent sequentially instead of capturing the whole image at once. Of course, these devices are limited by the speed at which they can scan. Since it raster scans an image instead of capturing it all at once, fast changing scenes cannot be captured and it can introduce artifacts such as motion blur.

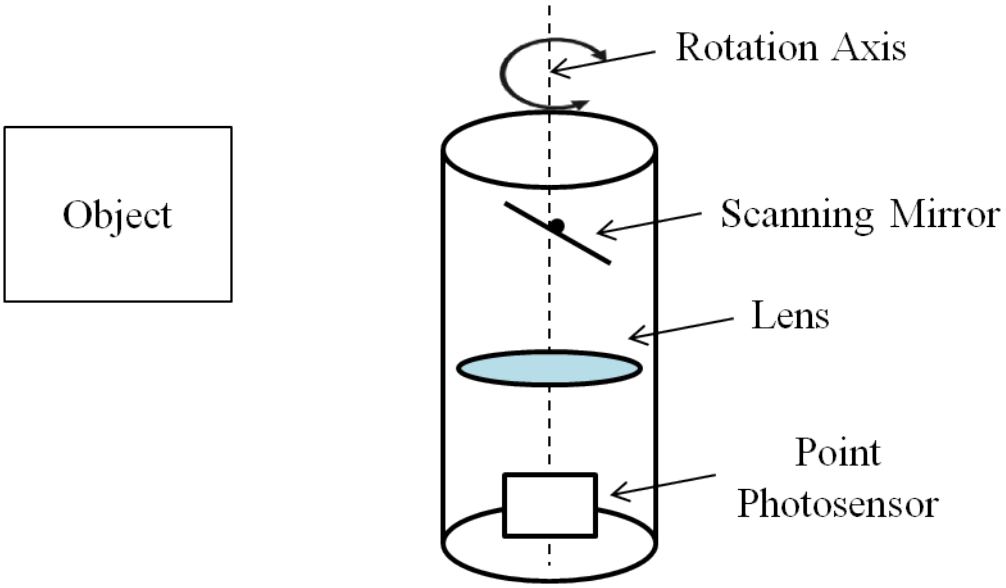

Fig. 1.1. An optical-mechanical imaging system.

Laser beam profiling is an area where high power and a high dynamic range can occur. Multiple measurements of the beam waist must be taken to solve an equation to find the parameters needed to describe laser beam propagation. Traditional laser beam profilers require multiple measurements of the laser beam waist, as seen in Fig. 1.2. Thus a large

range of mechanical motion is required along the optical axis. Additionally, most contain a mechanically moving pinhole. This large mechanical motion overhead can lead to repeatability and reliability issues. To overcome these issues, a laser beam analyzer using a DMD with a point photo-detector was proposed and demonstrated [1]. The point photo-detector was able to achieve a high dynamic range while the DMD improved pinhole repeatability and reliability [1]. Then the use of two photo-diodes was demonstrated to take into account fluctuations in the laser source over time [2]. To eliminate this movement the use of an ECVFL to change beam size by varying the focal length was proposed for single mode laser beams [25]. Comparing the DMD based laser beam profiler (see Fig. 2.2) and traditional optical mechanical scanning device, it is noticed that the laser beam profiler is in actuality an optical-mechanical imager, where the DMD removes the need for the mechanical scanning mirror and rotation of the system. Instead, the DMD creates the scanning mechanism using the two mirror states. This reduces the mechanical motion overhead that these devices have and also increases the speed of scanning of some of these devices since the DMD can refresh at rate of 32 kHz.

This background leads into the first section of the thesis on novel smart modules for imaging. Here smart modules for laser beam characterization/coherent imaging, incoherent imaging, and image

boundary detection are presented. These modules make use of a DMD and/or ECVFL along with other programmable devices. This includes being able to adapt to variations in irradiance, change resolution, and efficiently manage data.

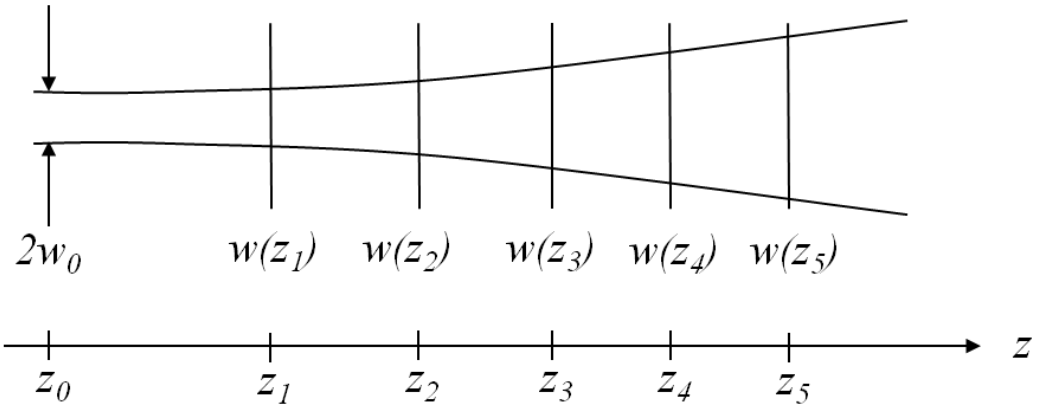

Fig. 1.2. Measurements of the laser beam waist *w* must be made at multiple locations along the optical axis (z-axis).

Chapter 2 presents the first demonstration of a motion-free electronically controlled multimode beam propagation analyzer using a DMD and a liquid ECVFL that serve as digital and analog agile optics, respectively [26]. In this broadband system, the agile optics smartly direct light for measurements so that an image can be constructed. The focal length of an ECVFL is varied and the analyzer measures the beam waist size for these different setting. Using an equation describing laser beam propagation along with the measurements taken the minimum beam waist size, minimum waist location, divergence and the M^2

parameter can be found. This is demonstrated for a 500 mW green (532 nm) laser source.

Chapter 3 presents a novel imaging system for both incoherent and coherent sources [27]. It builds upon the work for the laser beam analyzer to create a general purpose imager. Imaging smartness arises from the ability to control the focus using an ECVFL and the ability to use the DMD to adjust spatial sampling aperture size (sampling resolution), shape, and location. Dual port single-point photo-detection design provides imaging operation robustness to the global light irradiance variations such as via environmental effects, e.g., moving clouds. As the Texas Instruments (TI) DMD can provide light modulation over 400 nm to 2500 nm wavelengths, visible, Near Infrared (NIR), and Short-Wave Infrared (SWIR) bands can be simultaneously processed to generate three independent band images via three point photo-detectors.The presented imager can handle high power. Current DMDs are able to withstand short laser pulses with irradiances >2 kW/cm^2 for a 13.68 μm pixel DMD and >4 kW/cm^2 for a 7.56 μm pixel DMD (assuming the temperature of the DMD array without illumination is 50^{O}C) with the limit on average irradiance (continuous wave laser irradiance) being 25 W/cm^2 [28]. A proof-of-concept experiment in the SWIR band at 1580 nm is conducted using an incoherent heart shaped target that is sampled using the DMD imager set for a 68.4μm side

square moving pin-hole. A 5 x 5 pixels image from the proposed imager produces a 0.94 cross-correlation peak when compared to an optically attenuated heart shape image produced by a near 9 μm pixel size phosphor coated Charge Coupled Device (CCD) imager. Using the dual-detection method, robust 633 nm visible light imaging of an Air Force (AF) Chart figure is successfully demonstrated for 3 Hz global light fluctuation. Applications for the proposed imager include optical sensing in the fields of astronomy, defense, medicine, and security.

Chapter 4 presents a novel optical image scene object boundary mapping sensor using combined space-time processing within the framework of a Digital Micromirror Device (DMD) [29]. Sensor operation data efficiency is generated by smart spatial scanning of the image plane combined with single-pixel basis time delay electronic processing. In effect, compressed sensing is achieved using a hybrid optical-electronic means. Experimental results for target boundary detection are demonstrated for visible light illuminated rectangular and multi-square shaped targets. The presented remote imaging sensor is ideal for use in environments where brightly illuminated or radiating objects require shape-detection imaging within hazardous extreme environments of radiation, heat, cold, and harmful machine parts.

1.2 Novel Smart Modules for Communications

The development of optical wireless communication started in the 1880s when it was first demonstrated by Alexander Graham Bell and Charles Tainter that data could be transmitted by modulating sunlight [30]. Although this method was developed near the same time as the first RF wireless demonstration [31], it was not until the development of better light sources in the 1960's (i.e., the laser and LED) that optical wireless again became a highly active area of research in the public sector (there were military projects demonstrating the use of lamps and flash lamps for optical wireless applications before the advent of the laser). In 1978 it was proposed to use an infrared LED to communicate by filling a whole room with infrared radiation [32]. This method became known as diffuse (DF) optical wireless communications that is also robust to physical blocking. However, since DF optical wireless communications uses light travelling in multiple paths this method is highly power inefficient and has a limited data rate. To address the limitations of diffused infrared (DFIR) optical wireless, a technique using line-of-sight paths to communicate between users was proposed in 1985 [33], [34]. This technique became known as line-of-sight (LOS) wireless and directed beam IR (DBIR) wireless [35]. Later, more methods were developed and classified based upon the degree of directionality of the transmitter and receiver and whether the link used LOS or non-LOS

paths [35]. For example, the non-directed LOS transmitter uses a LOS wide area coverage beam versus a directed LOS transmitter that uses a narrow directed LOS beam pointed at the receiver. Later, new types of hybrid methods were proposed such as combining optical and RF wireless links to increase robustness to physical blocking [36], the use of multiple beams [37], [38], [39], etc. In addition to the papers already mentioned interested readers are referred to some review articles of the field [40], [41], [42], [43].

Today, optical wireless is still being investigated as an alternative to or good addition to RF wireless networks since RF wireless has some current issues. Issues of RF wireless include directionally insecure communication, sensitivity to RF electromagnetic interference (EMI), and a spectrum that is government regulated [35], [40], [44]. The severity of these problems depends on the application requirements. Directionally insecure communication means eavesdroppers can easily detect a signal and recover secure data once decryption is achieved. Secure communications is of the utmost importance in wireless networks for hospitals, banks, governments, and military. In some scenarios they do not want an eavesdropper to even be able to detect the signal. RF EMI in the environment can have adverse affects on RF wireless communication such as jamming communications. Since the number of wireless devices is constantly increasing the problems associated with

RF EMI are likely to degrade the performance of RF wireless devices. RF wireless is easily able to travel through walls, this means that wireless devices in neighbouring rooms or houses can also affect your personal devices. Additionally, RF EMI can be used to block communications maliciously. Lastly, there are different government regulations for the RF spectrum in different regions of the world. These government regulations can be costly and/or prohibitive in terms of compliance as the particular spectrum band licensed for a particular application may not be suitable and designs need to comply with the regulations in the different regions. Examples of the governing organizations for RF licensing include the Federal Communications Commission (FCC) and the National Telecommunications and Information Administration (NTIA) in the USA, Ofcom in the UK, and the Commission for Communications Regulation in the Republic of Ireland. Although methods for solving spectrum licensing issues have been proposed and researched [45], [46], [47], [48], they are still far from being implemented since they have to be tested and approved by the governmental regulators in a process that can be quite lengthy. On the other hand, optical wireless is directionally secure, insensitive to RF EMI, and has a spectrum that is license free. Additionally, optical wireless is easily able to achieve high data rates since it has a much higher carrier frequency and thus can carry wide RF bandwidths with

ease. Thus, optical wireless is an attractive alternative to RF wireless in many applications. However, optical wireless does have its limitations. Optical wireless is not able to cover large areas and is not robust to physical blocking. In addition, most of the optical wireless methods mentioned make poor use of limited light energy.

Fig. 1.3 illustrates what is meant by poor use of limited light energy. In traditional optical wireless links the system is made for a particular distance, but once this distance is exceeded then energy is wasted, as seen in Fig. 1.3. Additionally, if the receiver is too close in distance to the transmitter then the Gaussian beam imaging conditions are not met and there is a loss of optical power [49]. To adapt to a new distance, mechanical motion of the lens or a multiple lens systems can be implemented. However, in practice this is usually not the case and a large range of motion for the lenses would be needed to achieve a good range of distances. Another problem with optical wireless is it is not robust to physical blocking. If something is moved into the way of a LOS beam, communication is cut off. Having a system that is robust to physical blocking and makes good use of limited light energy is desirable. Chapters 5 and 6 focus on addressing these issues in optical wireless systems.

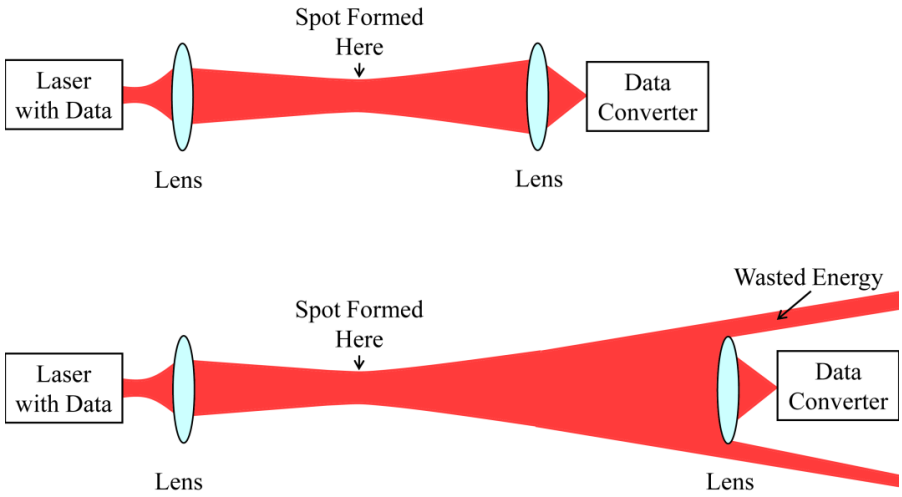

Fig. 1.3. Optical wireless link using a fixed lens. The lens fixes the distance that the laser beam spot forms. The top picture shows the link operating at its designed range, whereas in the bottom picture that range is exceeded and energy is wasted. *Figure from reference* **[50]**.

Chapter 5 presents the design of a power smart in-door optical wireless link that provides lossless beam propagation between Transmitter (T) and Receiver (R) for changing link distances [51]. Each T/R unit uses a combination of fixed and variable focal length optics to smartly adjust the laser beam propagation parameters of minimum beam waist size and its location to produce the optimal zero propagation loss coupling condition at the R for that link distance. An Electronically Controlled Variable Focus Lens (ECVFL) is used to form the wide field-of-view search beam and change the beam size at R to form a low loss beam. The T/R unit can also deploy camera optics and thermal energy harvesting electronics to improve link operational smartness and efficiency. To demonstrate the principles of the beam conditioned low

loss indoor link, a visible 633 nm laser link using an electro-wetting technology liquid ECVFL is demonstrated for a variable 1 to 4 m link range. Applications for this power efficient wireless link includes mobile computer platform communications and agile server rack interconnections in data centres.

Chapter 6 presents the design of a smart multiple mode in-door optical wireless system that combines line-of-sight (LOS) and non-LOS optical wireless methods to adapt smartly to changes in environment and application. The proposed design is able to operate in three optical wireless modes called directed LOS, non-directed LOS, and diffuse non-LOS. These modes smartly accommodate for changes in the number of users and their mobility, along with providing optimal light coverage area and increased robustness to receive light blocking. Experiments demonstrate for the first time demonstrate the use of multi-mode light sources in the proposed smart links using Electronically Controlled Variable Focal Length Lenses (ECVFLs).

Chapter 7 proposes a liquid lens technology-based 2x2 free-space optical switch using a pair of Electronically Controlled Variable Focus Lenses (ECVFLs) [52]. By controlling the focal lengths of two cascaded liquid ECVFLs independently, the two input optical beams are adjusted spatially to couple to their respective output beam ports.

1.3 Novel Smart Modules for Displays

The history of displays starts long ago when ancient storytellers used their hands or shadow puppets to make shadowy figures on the wall as they told their tales. These storytellers made use of their “projectors” to liven up their stories much the same as people do today when making presentations or telling tales to their kids. Now fast forward to the 1800’s when the modern photographic process was being developed indicating that the modern display has its roots in the history of photography. Predecessors to motion pictures include the Projection Praxinoscope developed by Charles-Émile Reynaud in 1877 which projected color animated drawings [53] and later a photograph projector developed by Eadweard Muybridge [54]. Eventually the cathode ray tube (CRT) display was developed which allowed for images to be displayed via an electronic signal. Today electronic displays are everywhere in many parts of the world. They are found in televisions, movie theatres, computers, cell phones, cars, and even household appliances. The dominant technologies in most display applications today are the liquid crystal display (LCD) and digital micromirror device (DMD) display. Another type of display used in some applications is the laser scanning display (LSD).

Today LCD, DMD, or LSD technology is used in projectors. Normally in projector systems the projector is designed for a certain

distance range. LCD, DMD, and old CRT projectors used a series of imaging lenses which required mechanical motion to focus at different distances. In laser scanning displays a lens is used to focus the laser beam to have specific beam size and divergence characteristics. The laser beam is raster scanned (or vector scanned) to form an image on the screen. Since the minimum laser beam waist occurs at a fixed distance and after this distance the laser beam is diverging there is a loss in image resolution as distance is increased. In addition, there can even be a difference in the resolution within the same image since some parts of the screen are farther than others. Thus it would be ideal to have a laser scanning display projector that maintains a high resolution for changing screen distances and could be adapted to keep the same resolution throughout the display. Such a design is presented in the last section of this dissertation.

Chapter 8 proposes and demonstrates a smart design for a Two Dimensional (2-D) optical display using 2-D laser scanning and an electronically programmable Three Dimensional (3-D) beam forming lens element [55]. Specifically, an Electronically Controlled Variable Focal Length Lens (ECVFL) has its focal length adjusted to produce the smallest focused beam spot on the display screen within the designed variable screen distance range. Since the screen distance is known, the angular scan range for the scan mirrors can be computed to generate the

desired number of scanned spots in the 2-D display. Thus a smart display with the smallest pixel spot size is formed, leading to the highest spatial resolution display for any given distance. Furthermore, if the scan angles are increased, a larger size display of higher pixel count can be formed without sacrificing display pixel size at this larger display size. A proof-of-concept smart display optics system is designed and demonstrated for a red 633 nm laser wavelength.

CHAPTER 2

MULTIMODE LASER BEAM ANALYZER USING ELECTRICALLY PROGRAMMABLE OPTICS

2.1 Introduction

Single mode Gaussian beams are the most commonly encountered laser outputs. They can be completely characterized by the values of minimum beam waist radius, the location of the minimum beam waist, and the wavelength of the light [56]. While many lasers are designed to have a single mode Gaussian distribution, in general, lasers with higher transverse order Gaussian modes and/or non-Gaussian distributions exist and the knowledge of the mentioned measurement values to characterize the laser beam is important in many applications. Additionally, any real laser beam is not truly a single mode Gaussian beam and for some applications these lasers need to be more accurately characterized. Characterization of these laser beams is done using the M^2 beam propagation parameter [57], [58], [59], [60]. For accurate characterization of the M^2 parameter, access to both sides of the minimum beam waist is required [60]. When access to both sides of the

minimum beam waist is not directly available, a lens is placed in the laser beam path to realize a secondary minimum beam waist such that direct beam waist access on both sides of the auxiliary beam waist is possible [60]. These prior-art methods not only require placement of a lens with a given focal length, but also require physical movement of the laser beam profiler assembly over a span of distances along the beam axis. Additionally, a translating mechanical pinhole within the profiler assembly is used to characterize the second-moment beam radii, adding to the mechanical motion overhead of the overall mechanism for multimode beam characterization [61], [62]. This physical movement can lead to errors in system alignment. Hence, the mentioned alignment error can affect the measured beam parameters since alignment of the laser beam with respect to the beam profiler can affect measured beam parameters [63], [64]. Hence these prior-art processes are time consuming, tedious, and most importantly, prone to poor measurement reliability.

Recently, a beam analyzer using a Digital Micromirror Device (DMD) and an Electronically Controlled Variable Focus Lens (ECVFL) has been proposed and demonstrated for the characterization of single mode Gaussian laser beams [25], [65]. The fundamental design of the deployed beam analyzer is based on the earlier proposed DMD-based optical imager used for irradiance mapping of coherent laser beams [1],

[2], [66], [67], [68], [69], [70] and optical targets illuminated by incoherent light [27]. The purpose of this chapter is to extend the earlier proposed DMD-ECVFL beam analyzer instrument for the characterization of laser beams using the M^2 beam propagation parameter. Specifically, the chapter presents the theory and demonstration of the DMD-ECVFL beam analyzer for measuring the M^2 parameters of a laser beam without requiring the movement of the beam analyzer to different planes along the direction of propagation of the laser beam, thus providing instrument features such as robustness, high repeatability, and improved speed of measurement.

2.2 Proposed Multimode Beam Analyzer Using Electrically Programmable Optics

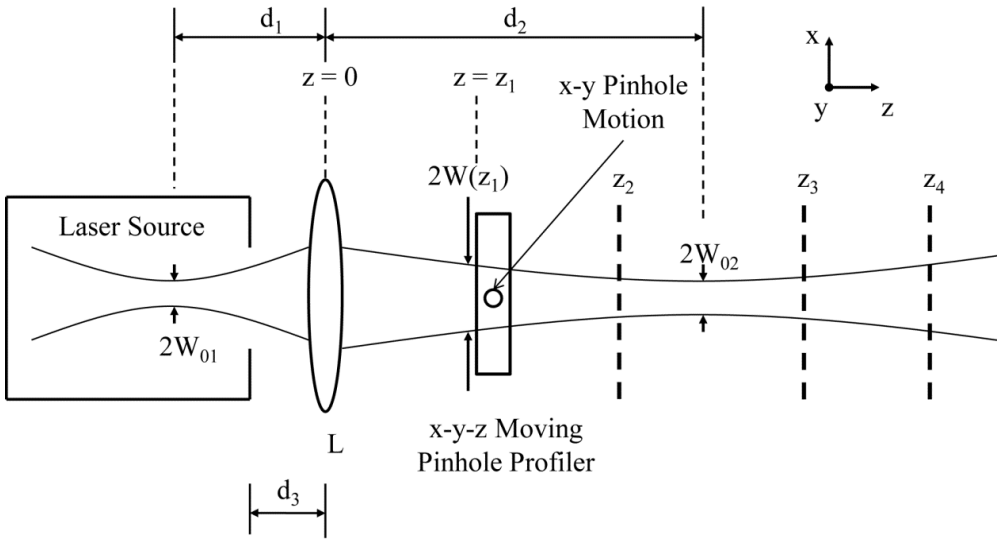

Fig. 2.1. The traditional moving optics beam analyzer method to determine the M^2 beam parameter. In the analyzer operation, as shown, the profiler imaging plane is moved along the z-axis and the beam waists are measured at multiple planes such as z_1, z_2, z_3, z_4, etc. Lens L has a fixed position and focal length *F*.

Fig. 2.1 shows the classic prior art method of an M^2 beam propagation parameter beam analyzer operation using a fixed position and focal length lens L to form an auxiliary waist outside of the laser using on-axis translational motion of the classical pinhole profiler along the laser beam. Additionally, an alternate design of the Fig. 2.1 analyzer involves keeping the profiler location fixed while translating lens L along the beam axis as is done in a commercial instrument [71]. The International Standards Organization (ISO) recommends approximately ten measurements on each side of the minimum beam waist [72], but using the four cuts method [60], a minimum of four beam profile measurements is sufficient to characterize the beam. Additional measurements can be taken to reduce the error as is done in commercial devices [60], [71].

The proposed multimode laser beam characterization instrument is shown in Fig. 2.2 for three cases of a typical laser minimum beam waist location with respect to the proposed instrument agile optics components [26]. The DMD operates as a digital mode moving pinhole image plane point sampler while the ECVFL acts as the variable focal length lens operating in analog-mode. The distances d_1 and d_2 are the location of the initial minimum beam waist W_{01} and the distance between the ECVFL and the DMD, respectively. In Fig. 2.2(a), the input laser beam is located inside the laser assembly and has its minimum beam waist $2W_{01}$

at location d_1. The ECVFL is operated with a positive (or convex lens) focal length F. This causes an auxiliary beam waist $2W_{02}$ to be formed. The laser beam travels along the optical axis and upon reaching the DMD plane, the beam waist is given as $W(F,d_2)$ which is dependent upon F, since d_2 is fixed in this design. DMD sampled light is reflected to the point photo-detectors PD1 and PD2 and optical power measurements are normalized to eliminate possible laser power temporal fluctuations during the course of the full 2-D beam profile generation. The test beam reflections to PD1 and PD2 are based upon the digital tilt states of the DMD micromirrors. Specifically, the micromirrors have two states, namely, the +θ state which reflects light to PD1 and the –θ which reflects light to PD2. The +θ and –θ states correspond to the reflections from the moving pinhole micromirrors and the non-pinhole micromirrors, respectively. In contrast to Fig. 2.2(a), Fig. 2.2(b) shows the case where d_1 is after the DMD and Fig. 2.2(c) shows a case where d_1 is between the ECVFL and DMD. Note that if the laser minimum beam waist location d_1 is between the ECVFL and DMD, as is shown in Fig. 2.2(b), an ECVFL with negative and positive focal lengths is required to form the necessary auxiliary minimum beam waists, since $W(F,d_2)$ measurements need to occur on both sides of its minimum value for accurate characterization. In Fig. 2.2(c), an ECVFL with negative and positive focal lengths might be required to generate the necessary

auxiliary minimum beam waists if the initial minimum beam waist $2W_{01}$ is close (i.e., within a few Rayleigh ranges) to the DMD.

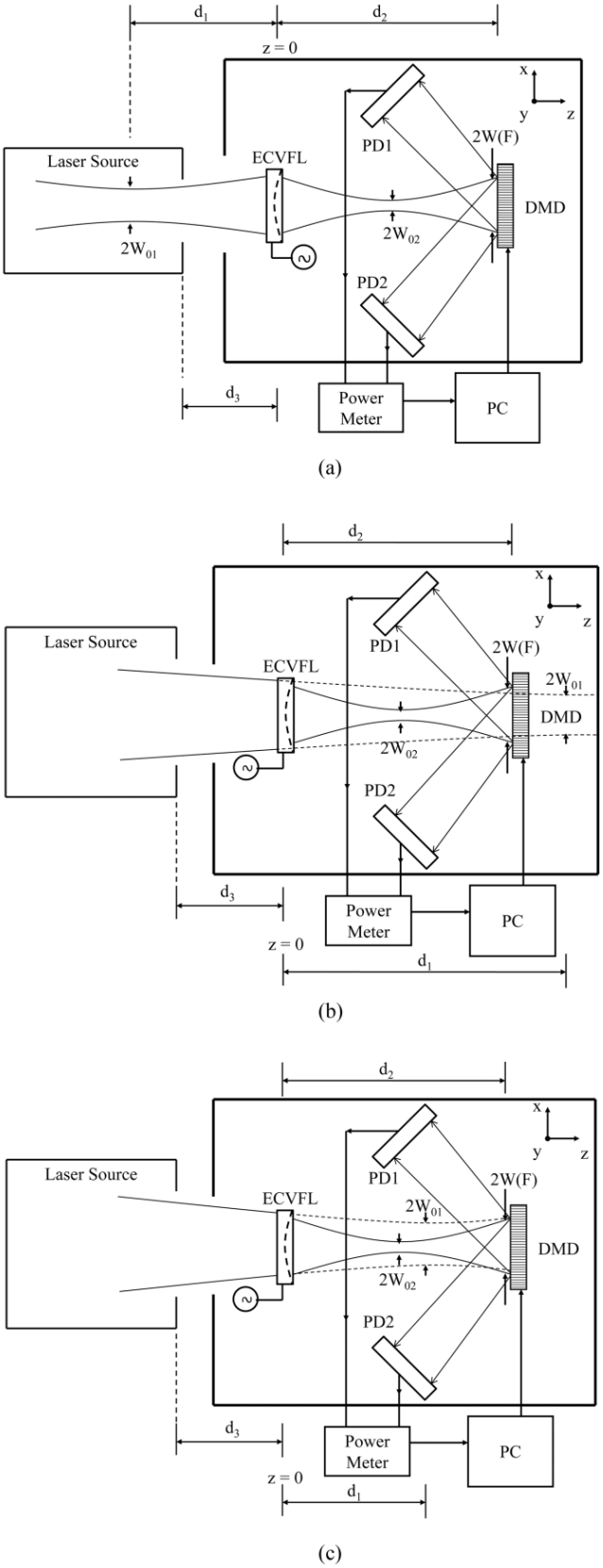

Fig. 2.2. The proposed multimode beam analyzer when the laser minimum beam waist forms (a) before the ECVFL, (b) after the DMD, and (c) between the ECVFL and DMD.

According to references [57]- [59], the propagation of a laser beam can be analytically described using the fundamental Gaussian beam mode and the M^2 beam propagation factor. In general, multimode beam radii at the beam waist can be written as:

$$W(z) = Mw(z) \tag{2.1}$$

where *w(z)* is the embedded fundamental Gaussian mode second-moment radius definition of the beam irradiance. Now, starting with the analysis for the fundamental Gaussian beam, the multimode beam can be described. The fundamental Gaussian beam optical field can be described according to Ref. [56] as:

$$\psi(r,z) \alpha\, exp\left(\frac{-jkr^2}{2q(z)}\right), \tag{2.2}$$

where α stands for proportional, the beam is traveling along the z direction, *r* is the radial distance from the optic axis, *k* is the wave number, and the complex *q* parameter is defined by:

$$\frac{1}{q(z)} = \frac{1}{R(z)} - j\frac{\lambda}{\pi w^2(z)} \ , \tag{2.3}$$

where λ is the wavelength of the light and *R(z)* the radius of curvature. At the minimum beam waist, the radius of curvature is infinite and the *q* parameter at d_1 reduces to:

$$\frac{1}{q_{01}} = -j\frac{\lambda}{\pi w_{01}^{\ 2}} \ . \tag{2.4}$$

The q parameter at the DMD plane can be found according to Ref. [56] as:

$$\frac{1}{q_1} = \frac{Cq_{01} + D}{Aq_{01} + B}, \tag{2.5}$$

where A, B, C, and D are the ABCD matrix elements describing the transfer of paraxial rays through an optical system. According to Ref. [25], this is given by:

$$\begin{bmatrix} A & B \\ C & D \end{bmatrix} = \begin{bmatrix} 1 - d_2/F & d_1 + d_2 - d_1 d_2/F \\ -1/F & 1 - d_1/F \end{bmatrix}. \tag{2.6}$$

Now according to Ref. [25] using equations (2.4)-(2.6), one can find that:

$$w^2(F, d_2) = w_{01}{}^2 \left[(1 - d_2/F)^2 + \left(\frac{\lambda(d_1 + d_2 - d_1 d_2/F)}{\pi w_{01}{}^2} \right)^2 \right]. \tag{2.7}$$

Substitution of Eqn. (2.1) into Eqn. (2.7) and solving for the beam waist at the DMD plane gives:

$$W^2(F, d_2) = W_{01}{}^2 \left[(1 - d_2/F)^2 + \left(\frac{M^2 \lambda(d_1 + d_2 - d_1 d_2/F)}{\pi W_{01}{}^2} \right)^2 \right]. \tag{2.8}$$

Now the full angle divergence and Rayleigh range of the multimode beam before the system can be written as:

$$\Theta_{01} = \frac{2\lambda M_{01}{}^2}{\pi W_{01}}. \tag{2.9}$$

$$z_{R1} = \frac{\pi {w_{01}}^2}{\lambda} = \frac{\pi {W_{01}}^2}{{M_{01}}^2 \lambda} \tag{2.10}$$

All beam waist measurements are defined using second order moments since this is what the M^2 beam parameter is based upon [72]. According to references [73], [74], [75], [76], [77], this definition is valid for many arbitrary real laser beams. The ISO also recommends using this second order moment in laser beam measurements [72]. Now using a pinhole for measurements, this beam radius can be written as [25], [58]:

$$W_H(F, d_2) = 2\sqrt{\frac{\sum_x \sum_y I(x,y)(x - x_0)^2}{\sum_x \sum_y I(x,y)}} \tag{2.11}$$

for the horizontal beam waist at the DMD plane. Here *I(x,y)* is the irradiance falling on the DMD pinhole located at the point *(x,y)* and x_0 is the centroid of the beam in the x direction given as:

$$x_0 = \frac{\sum_x \sum_y I(x,y)\, x}{\sum_x \sum_y I(x,y)}. \tag{2.12}$$

Similarly for the vertical beam waist radius,

$$W_V(F, d_2) = 2\sqrt{\frac{\sum_x \sum_y I(x,y)(y - y_0)^2}{\sum_x \sum_y I(x,y)}} \tag{2.13}$$

where y_0 is the centroid of the beam in the y direction given as:

$$y_0 = \frac{\sum_x \sum_y I(x,y)\, y}{\sum_x \sum_y I(x,y)}. \tag{2.14}$$

As shown in Fig. 2.2, to measure the beam waist, a moving pinhole is created using a DMD-based profiler [27], [65], [70]. The DMD-based profiler creates a digital moving pinhole which is highly repeatable, accurate, and has a spatial mapping resolution equal to one pixel pitch of the DMD. When compared to prior macro-motion mechanical profiling techniques, the DMD-based profiler offers 100% accurate digital spatial mapping repeatability. Using software control, the DMD realized pinhole scans across the test beam at the DMD plane and the instrument calculates the beam waists $W_H(F,d_2)$ and $W_V(F,d_2)$ for the horizontal and vertical directions using equations (2.11)-(2.14). Note that d_2 is a chosen fixed value for the measurement. Once the beam waists have been measured at a given F value of the ECVFL, F is changed while keeping d_2 fixed and the beam at the DMD plane is profiled again. This process is continued until several (e.g., four or more) beam waist measurements for different F values have been taken to provide a good data fit to equation (2.8). The curve fitting to equation (2.8) gives values for W_{01}, d_1, and M^2. Next, using equation (2.9) and (2.10) with the experimentally determined curve fit values, the divergence and Rayleigh range of the multimode beam can be found. Hence, using the proposed Fig. 2.2 instrument and the steps described for the operation of the instrument, the multimode test beam is completely characterized.

2.3 Experimental Demonstration

To characterize the multimode laser beam the Fig. 2.1 prior art method was implemented using a 500 mW Nd:YAG frequency doubled laser source λ = 532 nm with a lens L of focal length 15 cm, and a DMD based profiler. This visible band TI DMD has θ = 12º, a pixel pitch of 13.68 µm, and 1024 by 768 micromirrors. The distance between the laser aperture and L was d_3 = 16.7 cm and the laser beam was attenuated, for eye safety, using a neutral density filter with a 1% transmission. The light reflected off the DMD was spatially filtered so that only the 1st order reflections of the diffraction pattern were captured by PD1 and PD2. These detectors are 1 cm^2 active area 918D-UV detectors from Newport connected to a 2931C Newport Power Meter. The required beam irradiance $I(x,y)$ measurements were taken at multiple d_2 values along the z axis. Using the DMD profiler with this measured d_2 dependent $I(x,y)$ data and using Eqns. (2.11)-(2.14) the experimentally deduced values of $W_v(F,d_2)$ and $W_H(F,d_2)$ are computed and displayed in Table 2-I. Next, as shown in Fig. 2.3, curve fitting of the Table 2-I data is applied to Eqn. (2.8) and the parameters W_{01}, d_1, M^2 are found to be equal to 241.47 µm, -44.39 cm, 1.337 and 302.93 µm, -48.48 cm, 2.095 for the horizontal and vertical directions, respectively. Fig. 2.3 shows the Eqn. (2.8) plotted with the fitted parameters and experimental data. The negative sign on distances mean that the beam waist occurs after the

ECVFL. Next, using Eqns. (2.9) and (2.10) with the experimentally determined curve fit values of W_{01}, d_1, and M^2, the divergence and Rayleigh range of the multimode Gaussian beam are found to be 1.875 mrad, 25.76 and 2.342 mrad, 25.87 cm for the vertical and horizontal directions, respectively. Note that all *I(x,y)* have a spatial error/tolerance of one pinhole size, which in this case is one micromirror pitch (i.e., 13.68 μm) of the DMD.

Table 2-I. Second-Moment Beam Radii as a Function of d_2 with F = 15 cm.

d_2 (cm)	W_V (μm)	W_H (μm)
7.96	165.701	223.305
8.46	151.984	202.412
8.96	121.902	165.093
9.46	114.136	149.015
9.96	93.199	126.767
10.46	76.555	105.068
11.46	56.863	74.962
12.46	62.95	74.114
13.46	85.65	100.283
14.46	121.24	145.05
15.46	155.899	192.288
16.46	198.144	252.744
17.46	242.807	307.636
19.96	328.184	433.399

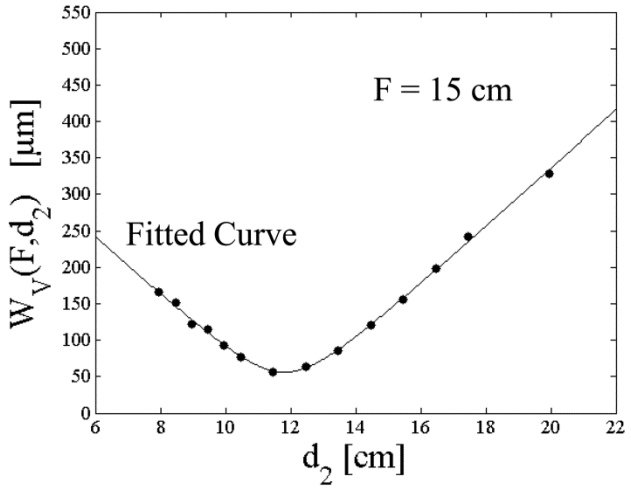

(a)

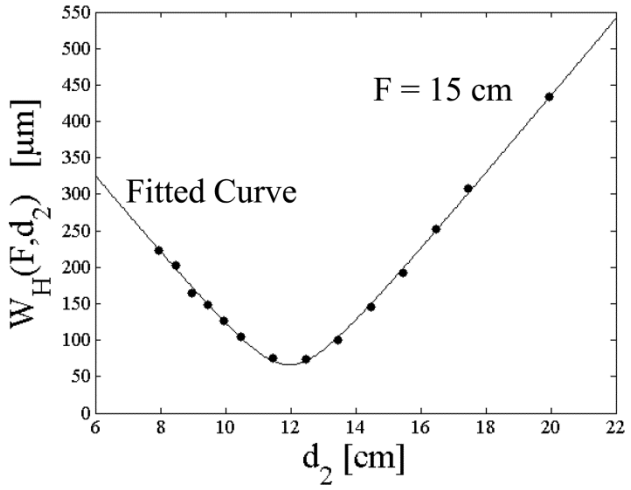

(b)

Fig. 2.3. Characterization of the multimode laser beam using the classic prior-art method with physical motion of the analyzer (i.e., the DMD) to measure the second-moment irradiance beam radii $W_v(F,d_2)$ and $W_H(F,d_2)$ at different d_2 positions. Data plots are for (a) the vertical (or y-direction) beam waist and (b) the horizontal (or x-direction) beam waist.

Next, the proposed multimode beam analyzer in Fig. 2.2(a) was setup using the same Fig. 2.1 DMD, laser source, detectors, and power meter. The lens L in the Fig. 2.1 setup is replaced by the ECVFL in Fig. 2.2. The distances d_1 and d_3 are the same as in the Fig. 1 experiment. The distance between the ECVFL and DMD was fixed to d_2 = 32 cm. The

ECVFL used is a Varioptic Artic France Model 320 liquid lens, which has a 2.8 mm clear aperture and can operate as a concave or convex lens [78]. The Varioptic voltage controller with a drive signal was used to adjust F from 8 cm to 36 cm. When aligning the system, it is important to note that according to references [63] and [64], any changes in the alignment of the transverse beam axes with respect to the beam profiler axes and off axis propagation can affect the measured beam parameters. One can right away see that such a problem can be very severe using classic prior art methods like Fig. 2.1 where many moving optics are deployed.

Using the DMD profiler with this F dependent measured $I(x,y)$ data and using Eqns. (2.11)-(2.14) the experimentally deduced values of $W_V(F,d_2)$ *and* $W_H(F,d_2)$ are computed. Next curve fitting the Table 2-II data to equation (2.8), as shown in Fig. 2.4, W_{01}, d_1, and M^2 are found to be equal to 257.61 μm, -46.53 cm, 1.600 and 326.67 μm, -48.99 cm, 2.587 for the vertical and horizontal directions, respectively. Fig. 2.4 shows the Eqn. (2.8) plotted with the fitted parameters and experimental data. Next, using equations (2.9) and (2.10) with the experimentally determined curve fit values, the divergence and Rayleigh range of the laser beam are found to be 2.103 mrad and 24.50 cm for the vertical direction and 2.682 mrad and 24.36 cm for the horizontal direction.

Table 2-II. Second-Moment Beam Radii as a Function of F with d_2 = 32 cm.

$\boldsymbol{F}$ (cm)	$\boldsymbol{W_V}$ (μm)	$\boldsymbol{W_H}$ (μm)
9.0	272.612	333.124
11.5	153.630	216.444
13.0	114.228	161.864
15.5	76.470	114.233
17.0	62.985	79.437
20.2	88.700	97.943
22.2	159.705	207.131
34.6	286.000	354.599

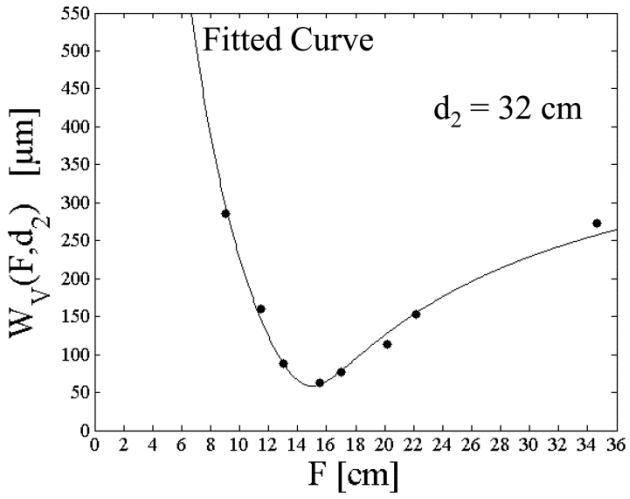

(a)

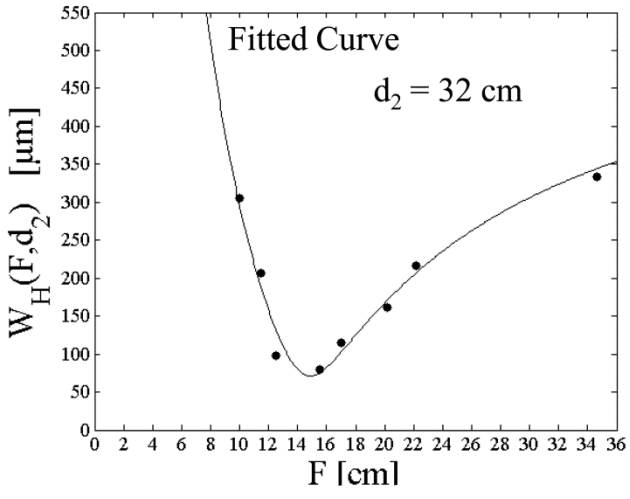

(b)

Fig. 2.4. Characterization of a multimode laser beam using the proposed DMD-ECVFL beam analyzer. Data shown are: the second-moment irradiance beam waist radius as a function of the ECVFL focal length F for (a) the vertical (or y-direction) and (b) the horizontal (or x-direction) beam.

The proposed design is compared with the traditional method in Table 2-III. Since the traditional scan method using the DMD profiler has a maximum error of one micromirror and the proposed DMD-ECVFL based method has a maximum error of one micromirror for each beam waist measurement, the maximum possible error between the measurements from the two instruments should be two micromirrors (i.e. 27.36 μm). Thus it is seen from Table 2-III that the two instrument experimental difference is within this two micromirror tolerance for W_0 for which the difference is 16.14 μm and 23.74 μm for the vertical and horizontal directions, respectively. It is important to remember that measurements be taken on both sides of the minimum of $W_v(F,d_2)$ and $W_H(F,d_2)$ as is seen in Fig. 2.4. Also increasing the number of measurements near the minimum increases the accuracy of the minimum beam waist size.

Table 2-III. Multimode Beam Propagation Parameters via the experimentally demonstrated traditional and proposed multimode beam analyzers.

	Horizontal		**Vertical**	
	Traditional	**Proposed**	**Traditional**	**Proposed**
$\boldsymbol{W_0}$ (μm)	302.93	326.67	241.47	257.61
$\boldsymbol{\Theta}$ (mrad)	2.342	2.682	1.875	2.103
$\boldsymbol{d_1}$ (cm)	-48.48	-48.99	-44.39	-46.53
$\boldsymbol{z_{R1}}$ (cm)	25.87	24.36	25.76	24.50
$\boldsymbol{M^2}$	2.095	2.587	1.337	1.600

2.4 Conclusion

Presented for the first time, to the best of the authors' knowledge, is a multimode beam analyzer using an Electronically Controlled Variable Focus Lens and a programmable digital spatial light modulator. The analyzer can be used to determine the beam waist size, the minimum beam waist location, the beam divergence, and the M^2 parameter of a laser beam [79]. Because the analyzer is electronically controlled, it does not require precision motion mechanics, increasing its reliability, speed, and repeatability. Specifically, having no moving macro-optics gives an advantage over traditional multimode beam analysis methods as misalignment of the beam propagation axis with the optical system as the lens or profiler is moved can affect the measured multimode beam propagation parameters. Experiments conducted with a 532 nm laser beam show that the multimode beam parameters using the proposed analyzer closely match the characterization results obtained using a traditional mechanically moving scan method.

http://dx.doi.org/10.1063/1.3669535

CHAPTER 3

DIGITAL MICRO-MIRROR DEVICE-BASED BROADBAND OPTICAL IMAGE SENSOR FOR ROBUST IMAGING APPLICATIONS

3.1 Introduction

Two Dimensional (2-D) imaging of luminous or illuminated objects in the visible, near infrared (NIR) and short wave IR (SWIR) bands are desired in numerous applications including astronomy, biological diagnostics, chemical sensing, food production, wireless communications, space-station instrumentation, and aerospace and defense systems. These wavelengths of observation typically range from 400 nm to 2500 nm. In the visible region and up to the 1100 nm NIR region, the silicon substrate-based CCD and CMOS sensor chips are the work horses for 2-D imaging applications [80], [81], [82], [83]. A typical CCD and CMOS sensor is a 2-D array of photo-sensitive pixels that capture the entire 2-D image without physically scanning the sensor device. To extend operations to NIR wavelengths, some industrial CCD designers use anti-Stokes phosphor coatings on the active area, thus producing visible band photons [84]. This indirect viewing of infrared radiation (such as at the 1500 nm optical fiber telecommunication band) has imaging limitations caused by the non-linear effects in the phosphor

film’s optical response and high inter-pixel crosstalk due to light flooding in the film layer. To transfer the elegant multi-pixel properties of the CCD to the NIR (700 nm- 1100 nm) and SWIR (1100 nm - 2500 nm) regions, other materials such as Indium Gallium Arsenide (InGaAs) for NIR and Cadmium Telluride (CdTe) for SWIR detection have been used to realize Focal Plane Array (FPA) detectors [85], [86], [87], [88], [89]. Both CCD and FPA sensors are highly sensitive devices that easily saturate at moderately low optical power levels, thus requiring attenuation of the incoming incoherent light image irradiance to prevent sensor saturation effects. As image attenuation optics can induce distortions in the original image, researchers since the 1960’s have resorted to using various optical scanning methods for high irradiance image detection [23], [24]. The most powerful such method involves physical motion of the optical image or sensor device in synchronization with a fixed position high dynamic range single point detector to accumulate pixel-by-pixel the optical image data and to process the data by computer to construct the final image [90]. As an optical attenuator can be placed after the image has been point sampled spatially (e.g., via a moving physical or virtual pin-hole) at the sampled image pixel site, one can adjust the optical attenuation on a pixel by pixel level, thus limiting image distortion. Furthermore, low light power level black out of the imager can be prevented by using high gain point photo-detectors

and optical and electronic amplification of the detected pixel-specific signal. Note that the required image transverse motion in such scan-based passive or object ambient light imagers can be optically implemented in a variety of ways including using scanning mirrors [91] and detector motion mechanics with extensions to multi-wavelength imaging [92]. Furthermore, Three Dimensional (3-D) optical scanners with a laser object illumination source and a single-point detector can be used for active (or laser-based) imaging of 3-D objects [93], [94]. Here, wavelength-to-space mapping allows 3-D spatial sampling including the use of optical amplification in the signal processing chain. Wavelength diversity has been suggested for endoscopic imaging applications such as ultrasonic [95] and optical imaging probes (with 1-D and 2-D scanning) [96], [97], [98], [99], [100], including optical amplification-based surgical (or optical knife) applications [101]. Various methods have been suggested to speed up the image acquisition time for these wavelength-coded imagers such as via multi-wavelength parallel processing optical detection channels [101] and more recently by use of single fiber channel wavelength dispersed time stretched serial processing [102], [103], [104]. Although wavelength diversity techniques for imaging have promise and can do away with mechanical moving parts, these wavelength encoded imaging systems involve complex optical and electronic hardware, making them high end

specialty imagers that also assume that the unknown sample under imaging operations has minimal spectrally varying characteristics. Thus, the single point photo-detector-based mechanical scan imager continues to have promise due to its simple and wavelength-coding free design. Nevertheless, robustness to the mechanical scanning operation of such an imager is required for reliable long-life imaging. Thus prior-art use of analog control of the scan mirror or point-detector motion mechanics over high pixelation counts (e.g., 1000 x 1000 pixels) to produce a quality image is a non-robust imager design, particularly over imager long operation life-times and environmentally challenging conditions, e.g., Vibration and temperature fluctuations.

Earlier, a Texas Instruments (TI) Digital Micro-Mirror Device (DMD)-based optical system was proposed and demonstrated as a moving aperture (e.g., knife-edge, slit, and pin-hole) spatial image sampler used to reliably produce the 2-D image power profiles of laser beams [1], [2], [66], [67], [68], [69], [70]. The DMD was also used for scene dynamic range and field of view control [4] and compressive imaging [105]. Because the DMD is an inherently all-digital device, the proposed image scanning and recovery process is 100% repeatable and therefore robust. Indeed, this original all-digital Spatial Light Modulator (SLM)-based laser beam profiler concept [1], [66] is applicable to simultaneous spectral bands imaging of luminous or illuminated objects

using incoherent light in the Visible, NIR, and SWIR bands, including imaging in variable light conditions such as weather related light temporal modulation. Thus, this chapter demonstrates the DMD-based optical image sensor within the context of imaging objects illuminated by incoherent light that includes imaging under temporally varying light conditions. The proposed imager features pixel-based imaging as well as high and low power handling, CCD/FPA competitive spatial resolution, moderately fast image acquisition times dependent presently on the specific DMD micromechanics and its electronic drive conditions, and potential for super-resolution imaging. Given that three point photo-detectors are used for the three wavelength bands instead of three large pixel count 2-D FPA/CCD sensors, the proposed imager is also suited for versatile hyper-spectral imaging. The chapter is organized as follows: description of the DMD-based smart imager optical design, a proof-of-principle experiment using an object radiating in the SWIR band, a second proof-of-principle experiment using an object radiating with variable light power in the visible band, and extensions of the imager design to other optical scanning device technologies including the ability for super-resolution imaging [67].

3.2 Basic DMD-Based Optical Image Sensor Design

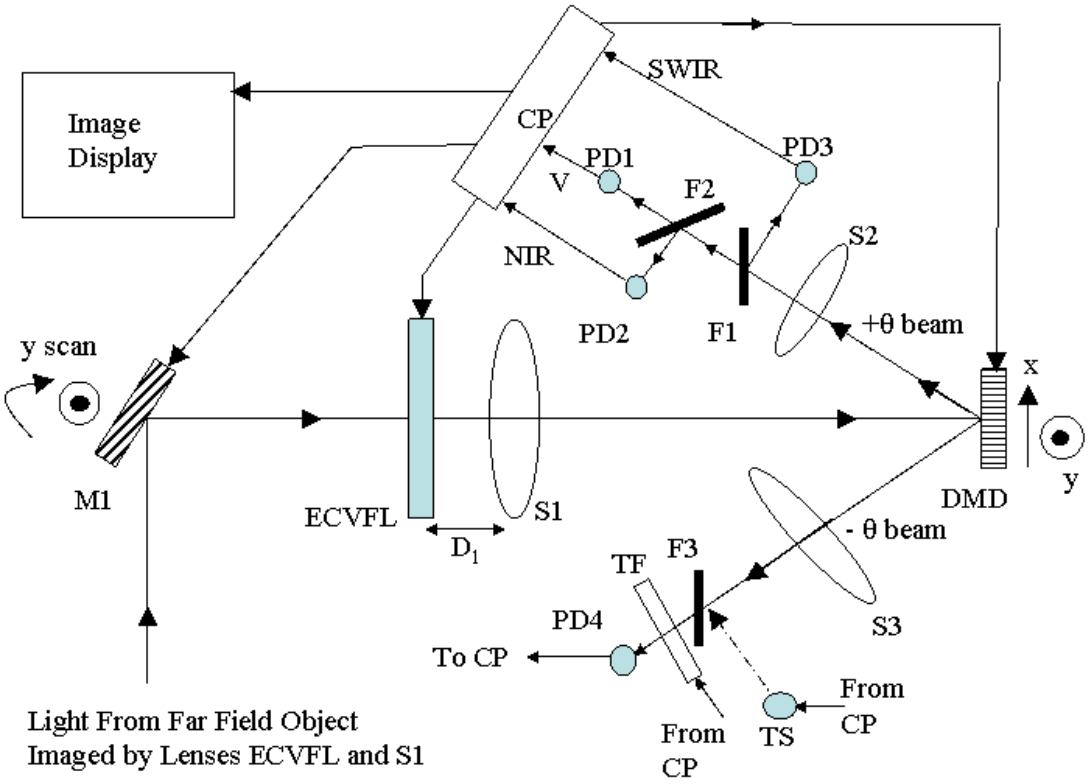

Fig. 3.1. Proposed DMD-based broadband optical image sensor for robust imaging.

Fig. 3.1 shows the design of the proposed DMD-based broadband image sensor [106]. The imager design is motivated via TI specified data indicating that the DMD with aluminum-alloy micromirrors and its glass window can operate with > 50 % transmission efficiency from near 400 nm to about 2700 nm. This means the TI DMD can be used for broadband applications spanning the visible, NIR, and SWIR bands. The imaging lens S1 along with the optional Electronically Controlled Variable Focus Lens (ECVFL) acts as the agile frontend imaging optics with the ECVFL providing a variable focal length by electronic control

such as via a liquid lens. Light from the object plane to the image plane travels via the optional y-scan mirror M1 to pass through the ECVFL and S1 to be imaged onto the DMD. The focal length F_{ECVFL} of the ECVFL is adjusted to form an imaging system with the DMD plane being the image plane. F_{ECVFL} depends on the distance '*P*' between the object plane and the ECVFL/S1 principal plane. The imaging equation between the object plane and the DMD image plane is given as:

$$\frac{1}{P}+\frac{1}{Q}=\frac{1}{F_{Eq}}. \tag{3.1}$$

Here '*Q*' is the distance from the principal plane of the ECVFL/S1 imaging system to the DMD plane. F_{Eq} is the equivalent focal length of this imaging system and it is given by:

$$\frac{1}{F_{Eq}}=\frac{1}{F_{S1}}+\frac{1}{F_{ECVFL}}-\frac{D_1}{F_{S1}F_{ECVFL}}.$$

(3.2)

F_{S1} is the focal length of S1 and D_1 is the distance between the ECVFL and S1. The image formed on the DMD plane is magnified by a ratio '*M*' given by:

$$M=\frac{Q}{P} \tag{3.3}$$

The DMD provides a moving pin-hole in a 2-D grid to sample the entire irradiance of the image with the selected +θ micro-mirror state light directed by the micromirrors towards a collection lens S2 and the

two dichroic beam splitters F1 and F2. M1 can be used to move the entire image on the DMD plane in the y-direction as the DMD scans a pin-hole in the x-direction, thus allowing faster image acquisition versus the classic 2-D grid pin-hole motion that requires many more frames of DMD full frame image updates. F1 physically separates the sampled image light into the visible/NIR and the SWIR bands while F2 separates the image light into its visible and NIR bands [86]. Hence the point detectors (PDs) PD1, PD2, and PD3 provide optical power data for the Visible (V), NIR, and SWIR bands, respectively. Each PD can have optional amplifiers to improve Signal-to-Noise Ratios (SNRs). The image plane -θ micro-mirror state light from the DMD is directed towards a focusing/collection lens S3 to pass through the dichroic beam splitter F3 and a Tunable Filter (TF) to fall on another point photo-detector PD4. F3 is designed to pass through the visible/NIR/SWIR bands while deflecting a specific laser wavelength. The TF is designed to electronically select one of the V, NIR, and SWIR light bands. Hence, compared to the simultaneous light bands detection mechanism in the DMD +θ beam port, the DMD –θ beam port uses a time-multiplexed light detection option via PD4. Note that the PD4 optical power reading can be combined with the PD1/PD2/PD3 optical power reading to give the total scaled optical power in the image falling on the DMD. When the entire image optical irradiance stays stable during the DMD image

scanning process, only optical power from the +θ beam port set of PDs is required for image reconstruction. Under temporally unstable image light conditions, data from PD4 is required for power corrected image processing as each PD power measurement is calibrated using the sum of optical powers from the PDs. This powerful calibration feature of the proposed imager in Fig. 3.1 is critical in real optical viewing environments where one does not have control of the targeted object illumination such as when there is a varying cloud cover during the imager total scan time. Thus, using the dual-port optical detection method, a passive-mode robust and reliable DMD-based imager is realized using the ambient light illuminating a target or emanating from the target. The design in Fig. 3.1 also shows an optional target illuminator source TS such as a targeting laser whose beam is collimated by S3 and then directed through S1-ECVFL to illuminate the target. In this case, the entire zone where the targeting light hits the DMD is set to the –θ micro-mirror state. One can also use the DMD to shape the targeting beam for optimal light-target interaction. The entire imager is controlled by a Control Processor (CP) that engages with the PDs, DMD, and optional devices ECVFL, M1, and TS to form a smart imager.

Today, the XGA format visible band optimized DMD has 768 x 1024 micromirrors with each pixel being a square with a 13.8 μm side. The

DMD can handle high optical powers in many Watts as the device has been used with high power lamps for movie projection displays. As mentioned earlier, in prior works that involved scanned image acquisition to handle high irradiance targets, one either moved the image with a scanning mirror or moved the point PD to sample the image. These traditional scan methods are prone to positional errors and scan speed limitations given a typical large 0.5 million pixel count for the desired image. In the proposed approach, the pinhole motion positions are fixed on the DMD pixel grid, and the pixel/pin-hole active operation on the DMD is controlled by software. This all-digital control of the location, size, and shape of the DMD-based pin-hole in-turn provides robustness to the proposed imager. Note that TI has recently produced hardware and software to control the DMD at 22,727 frames per second (fps). As a typical 2-D CCD sensor operates at a real-time rate of 30 fps, the DMD has a 758 times faster operation than real-time CCDs. Real-time CCDs also have a finite 33 ms integration time per pixel (for full image capture), so there can be image motion on the CCD pixel zone given a moving target. The same is true for any scanned imager solution like the proposed DMD imager and motion artifacts to a large degree can be removed by post-processing. As each pin-hole image on the DMD corresponds to one image frame on the DMD, a total of 22,727 pin-holes can be produced in 1 second. The actual speed of a complete image scan

will depend on the number of pixels produced by the x and y scans. The acquired image produced by the control processor CP after image processing is output on a display like an LCD panel. One assumes that there is no image optical irradiance variation during the DMD-based pinhole light acquisition time used to capture the irradiance value of a chosen pixel in the observed image.

3.3 Stable SWIR Source Imaging Experiment

For a first proof of concept experiment, the Fig. 3.1 imager without the optional components and dichroic optics is built in the laboratory for a SWIR demonstration given that visible and NIR band imaging is more common place. The IR optimized DMD used has 768 x 1024 micromirrors with each pixel being a square with a 13.68 μm side and $\theta=\pm 9.2°$ micromirror tilt state. A target object in the shape of a heart is created as a SWIR source at 1580 nm using a collimated laser beam, a heart-shaped spatial filter and an optical diffuser to form a spatially incoherent SWIR target. The target is placed a distance of 20 cm from lens S1 with focal length of 10 cm. The distance between S1 and the DMD is 20 cm, forming a 1:1 imaging system between the target and the DMD plane. A 10 cm focal length collection lens S2 is deployed along with a large area 3 mm diameter Germanium (800 nm to 1800 nm band) 2 μs response Newport 818-IR free-space detector. The 90 dB dynamic

range PD is connected to a Newport power meter Model 1830-C that is interfaced to a data acquisition computer P which controls the DMD and the power meter. The experiment uses a 0.15 mW/cm^2 power damage threshold Spiricon, Inc. Model 1550M (1440 nm – 1600 nm band) phosphor coated CCD imager with 30 dB dynamic range, a pixel size of 8.4 μm x 9.8 μm (5.4 mm x 4.7 mm active zone), and 640 X 480 2-D pixel grid. Fig. 3.2 shows a set of CCD images of the heart shaped target that are taken with varying (i.e., 3.81 dBm to 9.9 dBm) laser feed power levels. Fig. 3.2(c) shows the 640 x 480 pixels image just when it begins to saturate and is therefore used as the reference image while Fig. 3.2(e) indicates the full saturation image of the target.

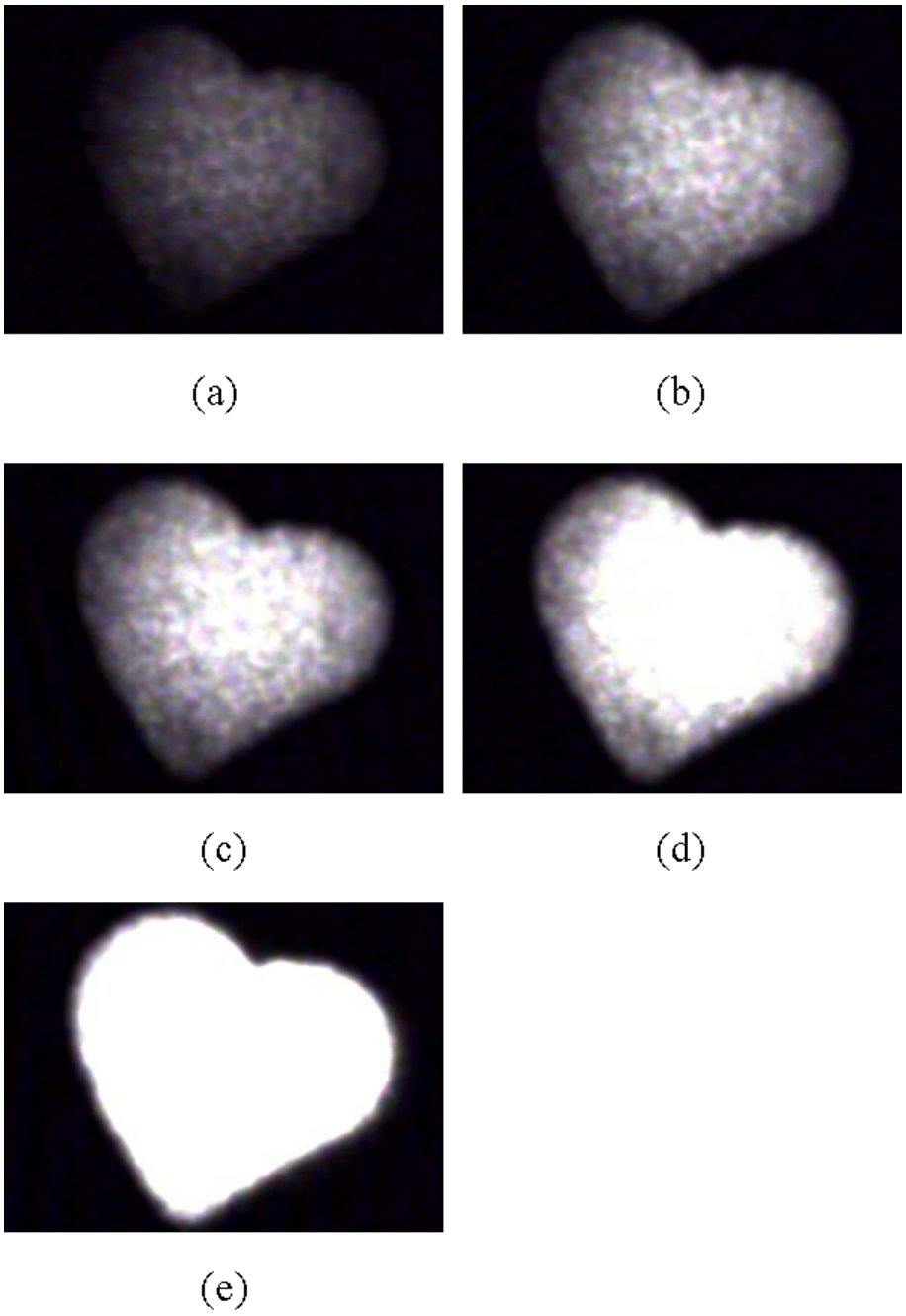

Fig. 3.2. Saturation-free to full saturation SWIR CCD images at 1580 nm of the heart shaped target produced with illumination laser powers of (a) 3.81 dBm, (b) 5.38 dBm, (c) 6.21dBm, (d) 8.00 dBm, and (e) 9.9 dBm.

Using the 9.9 dBm (~ 10 mW) laser power level that saturated the CCD, the DMD-based imager is deployed for imaging the target using a variety of decreasing size square-shaped test pinholes with pinhole sides of 20 micro-mirrors, 10 micro-mirrors, and 5 micro-mirrors to give physical pinhole sizes of 273.6 μm X 273.6 μm, 136.8 μm X 136.8 μm, and 68.4 μm X 68.4 μm, respectively. After optical power data processing by the computer, Fig. 3.3 shows the DMD imager acquired SWIR images of the heart shaped target, clearly showing the improvement in image quality with smaller pin-hole sizes. More importantly, the variable power distribution across the heart shaped target has also been recovered and is visible in the Fig. 3.3 images. To cover the approximately 4.75 mm x 4.82 mm boxed zone (see Fig. 3.3(d)) that encloses the heart shaped target, Fig. 3.3(a), (b) and (c) show constructed images using DMD pin-hole counts of 20 x 20, 10 x 10, and 5 x 5, respectively. Smaller pin-hole sizes may be used to achieve higher resolution.

To estimate the quality of target image matches between the unsaturated SWIR CCD image capture and the DMD imager acquired images, an image correlation operation is performed by the computer. The image discrete cross-correlation function $h(j,k)$ for two image functions $f(n,m)$ and $g(n,m)$ is given by:

$$h(j,k) = f * g = \sum_{n=-\infty}^{\infty} \sum_{m=-\infty}^{\infty} f(n,m) g(n+j, m+k). \qquad (3.4)$$

Here the function shifts j and k are in the n-direction and m-direction, respectively.

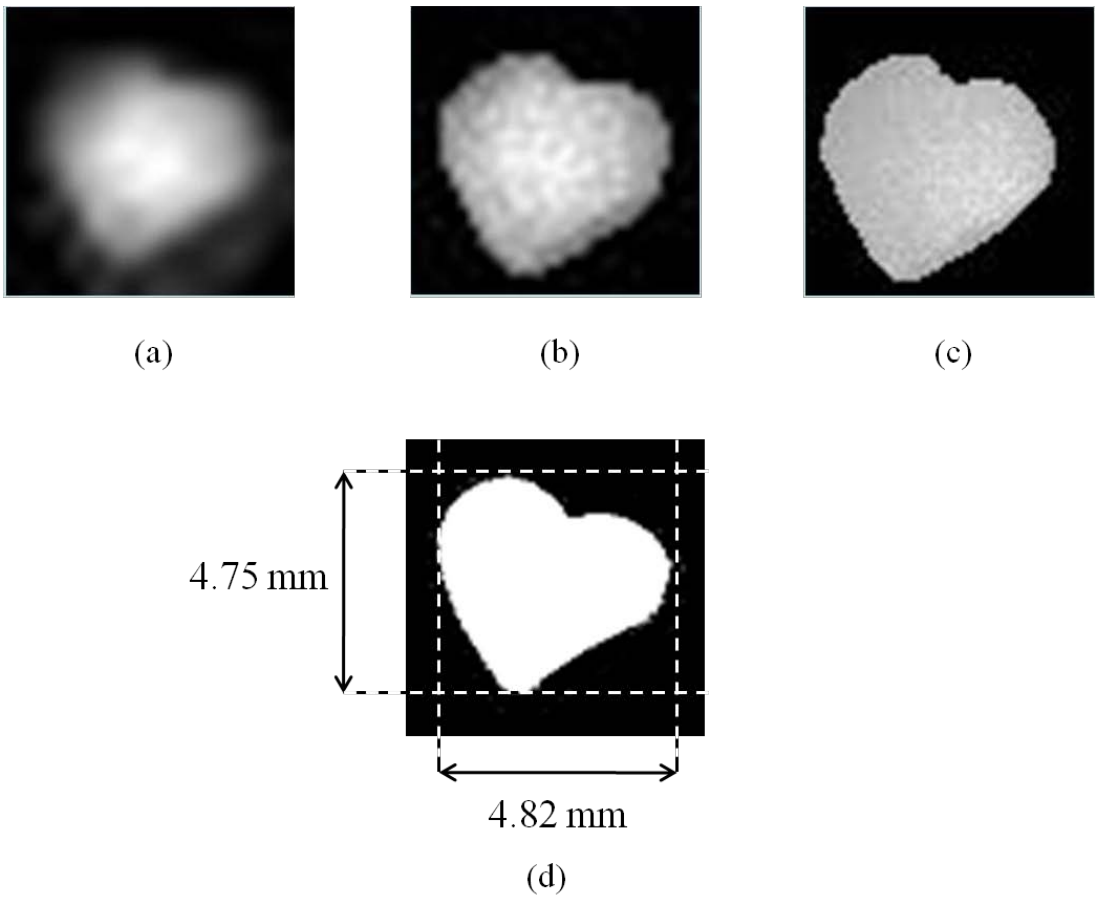

Fig. 3.3. Heart shaped target images acquired with the proposed DMD-based imager when the target illumination laser power of 9.9 dBm is saturating the CCD. The images shown are constructed with DMD pin-hole sizes of (a) 273.6μm X 273.6μm, (b) 136.8μm X 136.8μm, and (c) 68.4μm X 68.4μm. (d) The CCD image shows the 4.82 mm x 4.75 mm box zone that contains the heart shaped target.

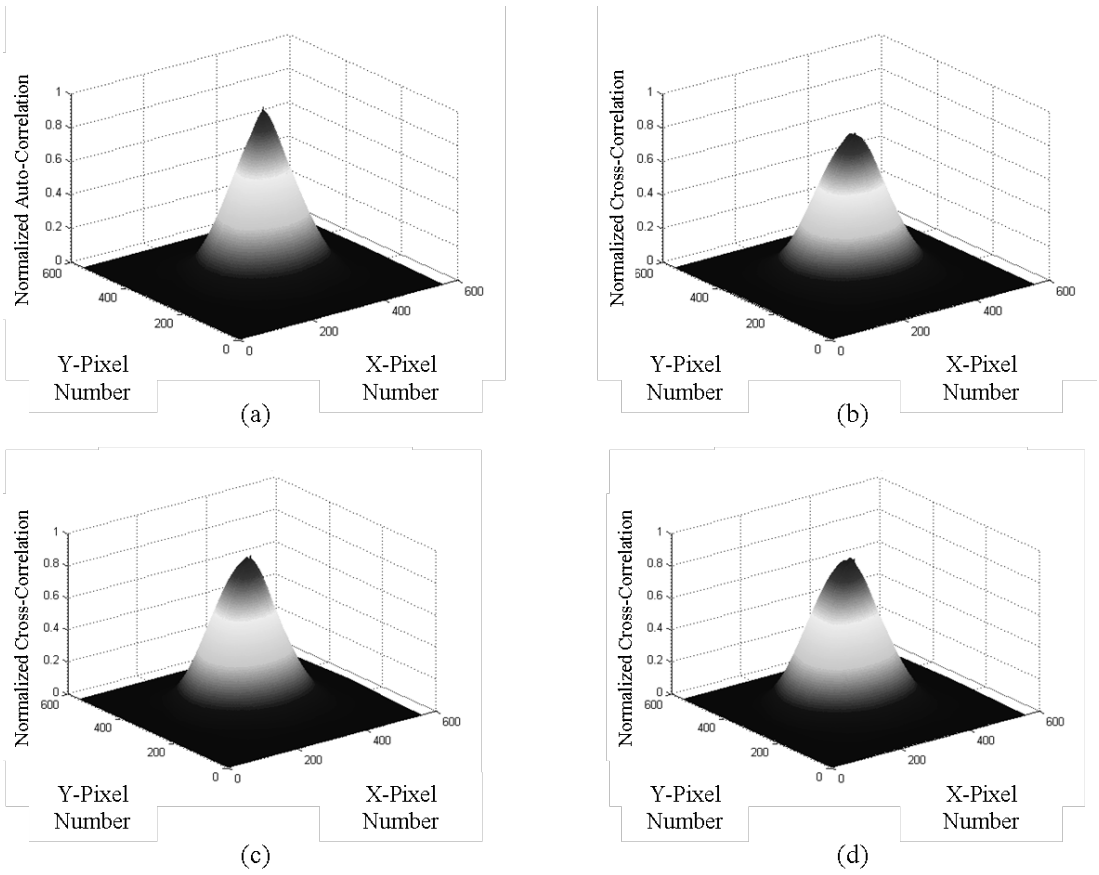

Fig. 3.4. (a) 2-D image correlation plot for CCD image auto-correlation using Fig. 3.2(c) image. In addition, shown are 2-D image cross-correlations with reference CCD image Fig. 3.2(c) and the DMD imager provided images uses DMD pinhole sizes of (b) 20X20, (c) 10X10, and (d) 5X5 micromirrors.

Fig. 3.4(a) shows the image auto-correlation plot of the reference image (i.e., Fig. 3.2(c)) while Fig. 3.4(b)-(d) shows the image cross-correlation plots with the reference image and the Fig. 3.4 images from the DMD imager. The results of Fig. 3.4 indicate that the peak cross-correlation values are 0.94, 0.93, and 0.84 for DMD pinhole sizes of 273.6 μm X 273.6 μm, 136.8 μm X 136.8 μm, and 68.4 μm X 68.4 μm, respectively. Note that the ideal cross-correlation peak of unity would be possible if a higher than 20 x 20 pin-holes (sampler pixels) image was

acquired by the proposed DMD imager. Fig. 3.3(c) also indicates a fine jaggedness in the heart shape image boundary and this boundary will be smoother if the pixel sampling size deployed the smaller 13.68 μm pixel size limit of the present DMD individual micromirror. As the DMD has 786,432 pixels, high quality imaging is possible by the proposed imager. Presently, the imager's data acquisition and post-processing was not fully automated and hence not performed in real-time.

3.4 Unstable Visible Source Imager Experiment and Design Extensions

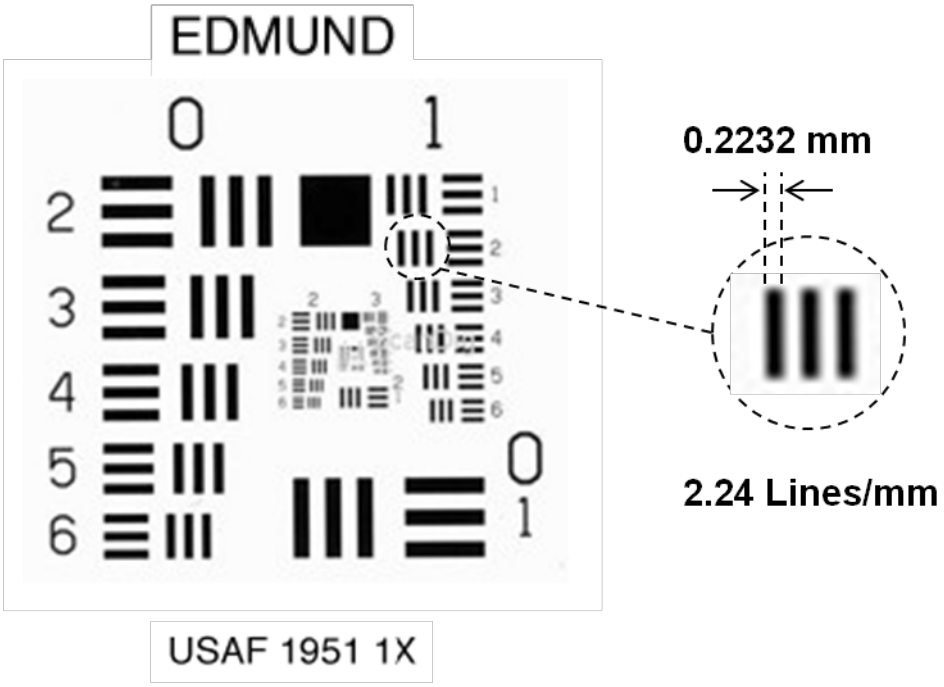

Fig. 3.5. Air Force (AF) target 3-bar zone indicated by the dashed circle. This circled zone is used as the illuminated incoherent visible band test object subjected to DMD-based imaging.

A second experiment using a similar optical set-up as in Section 3 is conducted using a visible band optimized DMD with 768 x 1024 micromirrors with each pixel being a square with a 13.8 μm side and θ=±12° micromirror tilt state. A stable 10 mW 633 nm linear polarization He-Ne laser collimated beam is used to illuminate a 1951 Air Force target 3-bar zone shown in Fig. 3.5. A diffuser is placed after the target to form an incoherent diffused target. A 7.5 cm focal length S1 lens is used in a 2F-2F configuration to form a 1:1 imaging system between the AF target and DMD plane separated by 30 cm. The collimated laser beam is intensity modulated at 3 Hz using a Twisted Nematic Liquid Crystal (TNLC) polarization modulator. This 3 Hz sine wave modulation of the optical laser beam power produces a 20% reduction in laser optical power at the null of the sine wave, thus simulating a target with a slowing varying illumination source such as a slowly moving day-time cloud cover. The DMD is programmed for a scan pixel update rate of (1/75) kHz with a sampling pixel made up of 5 x 5 micromirrors with a pixel size of 68.4 μm x 68.4 μm. Lenses S2 and S3 of 5 cm focal lengths are used as the collection lenses. Newport Model-818 1 cm^2 active area silicon PDs with response times of < 3 μs and Newport power meters are used to record the PD1 and PD4 optical power levels for CP-based image reconstruction. A Black & White SONY XC-77 8.8 mm x 6.6 mm sensing area CCD imager (Pixel size 11

μm by 13 μm and Pixel Count of 768 X 493 pixels) is used to record the zero temporal modulation diffused visible AF target at the DMD plane as shown in Fig. 3.6(a). With the Fig. 3.1 system operating in its standard one PD data gathering mode (i.e., PD1 collecting optical power data) and the 3 Hz target light variation turned on, Fig. 3.6(b) shows the image obtained from the proposed DMD-based imager. Fig. 3.6(b) clearly shows that the image obtained is not a good match with the original AF target image in Fig. 3.6(a). Next, the DMD imager is operated in its dual-detector mode using both PD1 and PD4 and the obtained image is shown in Fig. 3.6(c). Clearly, one can see a significantly better match between the DMD-based image in Fig. 3.6(c) and the original target image in Fig. 3.6(a).

A 2-D correlation operation with the Fig. 3.6(a) reference image is conducted indicating correlation values of 0.64 and 0.91 for the signal images of Fig. 3.6(b) and Fig. 3.6(c) images, respectively. Fig. 3.7(a), (b), and (c) show the 2-D correlation plots for image auto-correlation (for Fig. 3.6(a)), image Fig. 3.6(a) and Fig. 3.6(b) cross-correlation, and image Fig. 3.6(a) and Fig. 3.6(c) cross-correlation, respectively. These proof-of-concept experiments clearly point to the powerful robustness of the proposed imager using the dual-detector mode that is naturally possible via the 2-port beam operations of the ±θ deflection states of the DMD. Note that improved image quality can be achieved using smaller

pixel sizes including a single micromirror, although at the expense of longer image scanning times.

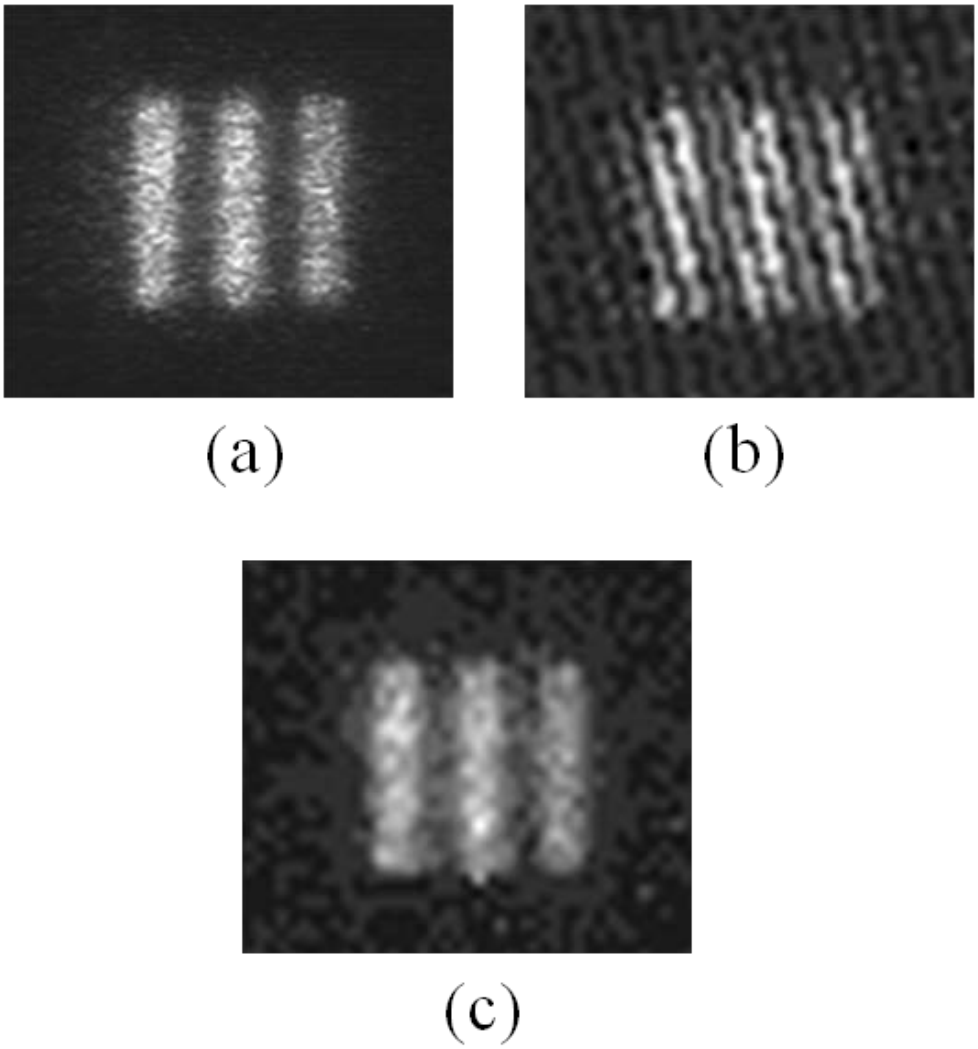

Fig. 3.6. (a) AF target image acquired with a CCD imager. (b) Single photo-detector and (c) two photo-detector based imaging of the bar target via the DMD-based imager. The (b) and (c) images are acquired using a 5x5 micromirrors pin-hole size and a 3 Hz light power variation of the target illumination source.

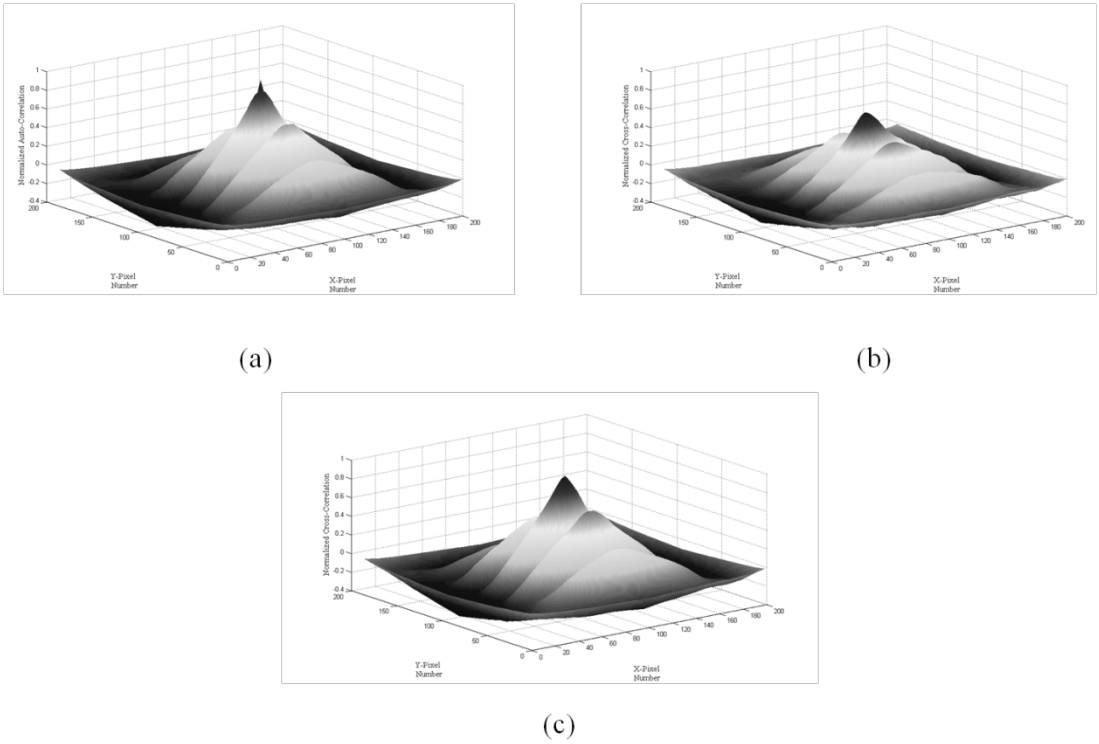

Fig. 3.7. The 2-D image correlation plots for (a) CCD image auto-correlation using Fig. 3.6(a) image. 2-D image cross-correlations with reference CCD image Fig. 3.6(a) and the DMD imager provided images from (b) single detector mode and (c) dual-detector mode.

Another SLM device technology that has broadband optical modulation capabilities is Liquid Crystal (LC)-based SLMs [107]. Unlike the reflective DMD, LC SLMs are generally transmissive optical devices with a single output port where the PD is placed to record optical power data as a moving pixel is programmed to implement the image scanning operation. Hence, the transmissive LC SLM-based imager naturally has only one port to place the PD. Fig. 3.8 shows a novel design of a LC-SLM-based optical image sensor to enable operation of a dual-detection mode for full imaging robustness.

Specifically, a Polarizing Beam Splitter (PBS) is placed after the LC SLM to produce two spatially independent beam ports where the pixel-on and pixel-off portions of the light irradiance on the SLM plane are directed for optical power measurements needed for PD1 and PD4 calibrations. Light coming from an ambient light illuminated object has naturally both p (horizontal) and s (vertical) polarizations. The polarizer P in front of the LC SLM makes sure that one linear polarization (e.g., p) passes into the LC SLM. Each pixel in the LC SLM can be programmed to either flip the input polarization by 90° (pixel on-state) or keep the polarization unchanged (pixel off-state). Next, the p/s polarized light strikes the PBS with the p-polarization light passing straight through the PBS while the s-polarization light is deflected by the PBS. The p-polarization light passes through collection lens S2 to fall on PD1 while the s-polarization light passes through collection lens S3 to fall on PD4. The Fig. 3.8 system is shown using some basic components of the Fig. 3.1 DMD imager to demonstrate a basic design using a transmissive LC SLM to deliver the 2-PD robust imager design.

The proposed SLM-based imager designs can take advantage of super-resolution image processing techniques such as sub-pixel shift image capture [108]. Specifically, these sub-pixel entire image shifts in the x and y directions of the image plane can be achieved by a number of methods such as x-y mechanical motion of scan mirror M1 (in Fig. 3.1

and Fig. 3.8) or SLM motion [67], [109]. Another option is use of a tilting optical flat or a variable refractive index LC cell placed between the SLM and S1 that use Snell's law to cause the image to translate on the SLM plane. Because these sub-pixel shifts are very small (e.g., < typical pixel size of 14 μm), the pixel shift process can be relatively fast.

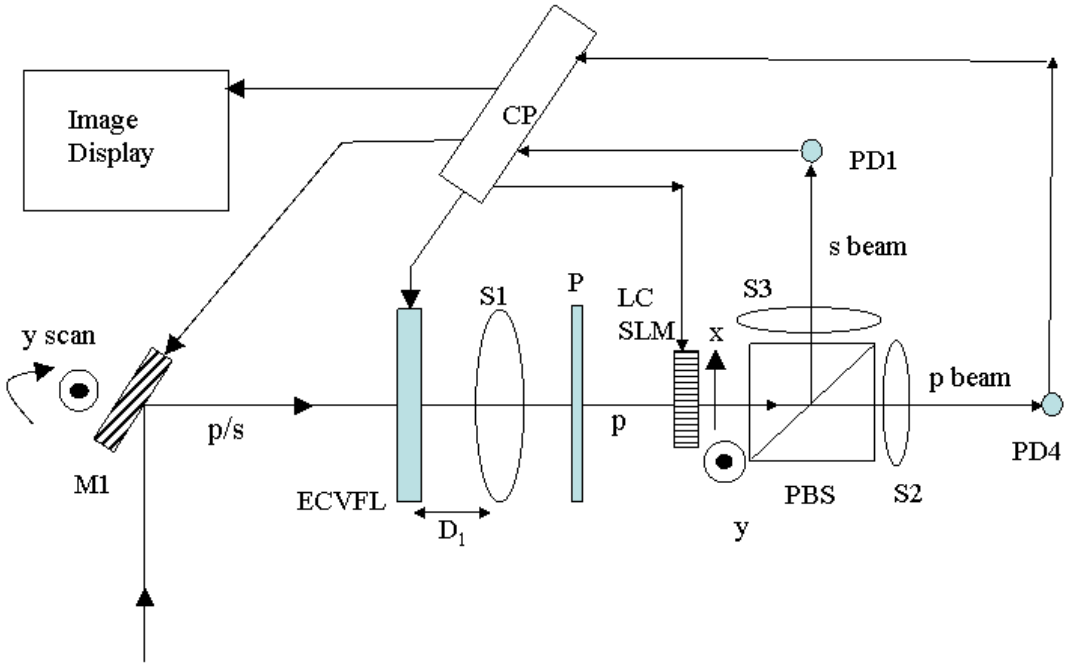

Fig. 3.8. Liquid Crystal Spatial Light Modulator-based robust optical image sensor design using the dual-detection mode.

Finally, note that because the proposed imager uses an ECFVL in the frontend optics, 3-D imaging is also possible by controlling the far-field spot size of the illuminating beam or via control of the imaged distance along the light propagation direction, thus adding further smartness to the imager design [25], [65], [110], [111], [112].

3.5 Conclusion

To the best of the authors' knowledge, demonstrated for the first time is a DMD-based optical image sensor for visible, NIR and SWIR applications. Basic imager smartness comes from the full programmability of the shape, size, and position of the moving aperture that samples the incident image to construct a high dynamic range broadband irradiance distribution. Robustness of the imager operations comes from the all-digital 100% repeatable pinhole motion and its independence to imaged light temporal fluctuations during the pinhole image scan process. First stage experiments have been completed for SWIR wavelength incoherent target imaging and temporally varying light conditions visible target imaging. Future work will optimize all aspects of the proposed DMD-based optical image sensor to realize a robust, fast response, high optical power handling broadband imager that can empower optical image sensing applications in a variety of scientific and industrial applications.

http://dx.doi.org/10.1016/j.optcom.2010.08.078

CHAPTER 4

DATA EFFICIENT DIGITAL MICROMIRROR DEVICE-BASED IMAGE EDGE DETECTION SENSOR USING SPACE-TIME PROCESSING

4.1 Introduction

Boundary or edge detection is an important field of research in image processing with applications within the military, medical, and computer vision arenas. Traditionally, the entire optical image frame is captured by an optical camera and then the full image frame data set is sent for electronic post-processing using software based edge detection algorithms. Current algorithms cover a wide range in terms of complexity, speed, and performance. Some methods involve finding the gradient of the image [113], [114], [115] whereas others rely on simple differencing of pixels [116], [117]. Once the entire image data set is processed, an edge-mapped image can be obtained. The quality of detecting a boundary in the original scene depends not only upon the algorithms used to detect the edges, but also the imager hardware used to capture the original object. Thus, preprocessing techniques for edge detection by modifying the optical system have also been considered [118]. Currently, most imagers use a CCD or CMOS technology multi-pixel Two Dimensional (2-D) optical imaging device where image data

for all the pixels in the 2-D imager chip are simultaneously captured, stored, and transmitted to produce the full frame image signal required for post-processing. CCDs have problems with saturation due to their limited dynamic range. On the contrary, very high 115 dB dynamic range CMOS imager chip device designs have been demonstrated [119], but this increase in dynamic range comes at the cost of increased complexity and larger pixel sizes. Furthermore, both CCDs and CMOS optical detectors are limited by their narrow operational wavelength range, e.g., 400 nm to 700 nm for a visible light CCD chip. Hence, for imaging applications where large amounts of data are stored for post processing such as for the proposed target boundary detection operation, it would be beneficial to have an imager hardware design that intelligently finds and stores only the target edge information during the real-time optical irradiance mapping process of the imager. In effect, one has directly implemented compressed [120], [121] boundary detection sensing in the optical domain as one no longer requires storage of the whole image per frame acquisition, leading to lower power consumption of the sensor given the smaller data storage capacity and lower sensor data bandwidth. With this goal in mind of compressed boundary detection sensing, presented is a novel optical sensor architecture using intelligent space-time hardware embedded processing to realize a robust target edge detection sensor suited for mapping edges of targets in

extreme environments of high dynamic range backgrounds and wavelength diversity. Example targets can be flying objects (planes, rockets, etc) in a sky background or hot machine parts undergoing industrial inspection in uniform backgrounds. The proposed sensor design is based on an earlier proposed DMD-based imager [1], [2], [27] and incorporates the dual-detector DMD single-pixel intelligent spatial optical scan in collaboration with pixel-delay based electrical processing to produce the vital edge detection data directly. The rest of the chapter describes the sensor design and a basic proof-of-principle laboratory sensor operation of visible target edge detection. Do note that point-detector (or single pixel) based imaging dates back to the 1960s [23], [24] and the DMD has been proposed for classical imaging [4] as well as for compressive sensing using pseudorandom binary patterns [105]. Traditional compressive sensing [105], [120], [121] involves under-sampling the signal and using this smaller sample set with reconstruction algorithms for recovery of the original scene. Hence an objective of compressed sensing is to use the smallest data set possible to adequately represent the original signal. The proposed system in this chapter also seeks this objective, although without using under-sampling of the original signal.

4.2 Space-Time Processing Image Edge-Detection Sensor

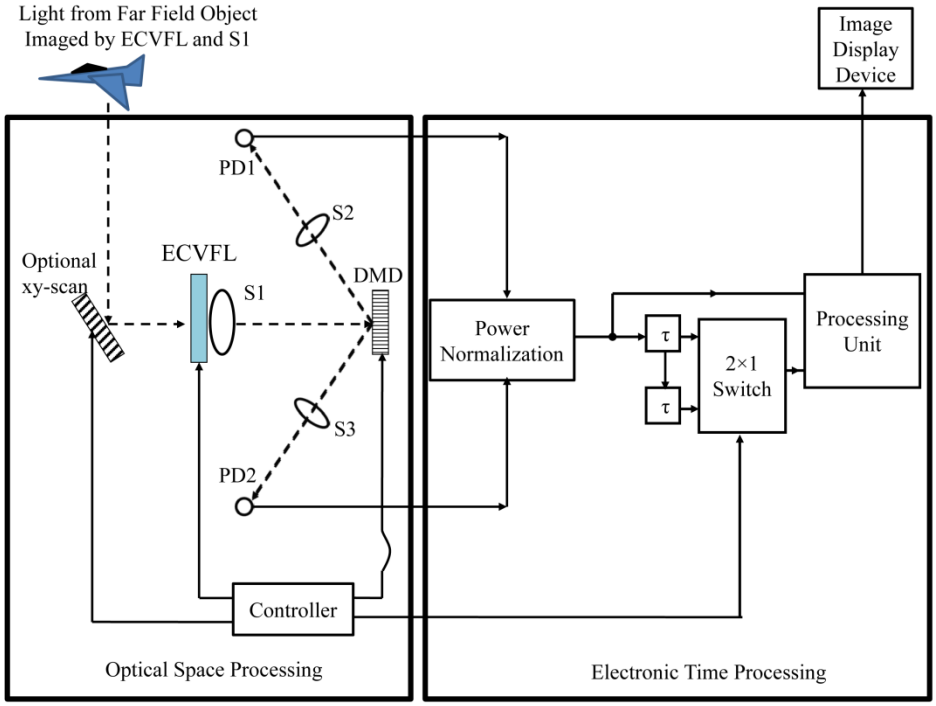

Fig. 4.1. The proposed space-time processing based edge detection sensor using the dual point optical detectors and single DMD operations.

Shown in Fig. 4.1 is the proposed boundary mapping sensor using space-time signal processing implemented via electronically controlled variable optical focal length and 2-D irradiance pinhole scanning devices in combination with dual point-detection optical hardware, pixel delay, and programmed comparator electronic devices [29]. Specifically, the imaging lens S1 and the Electronically Controlled Variable Focus Lens (ECVFL) form the imaging optics for the sensor. Adjusting the focal length of the ECVFL gives the system variable focusing capabilities. Light from the in-focus target plane enters the sensor system by the

optional xy-mirror scanner and is imaged by the imaging optics onto the DMD plane. The DMD is a wavelength diverse device operating over a wide 400 nm to 2500 nm band [122]. This optical device is programmed to form a digital pinhole which scans across the 2-D image plane sampling the irradiance with a pinhole. The pinhole is formed by adjusting the ±θ tilt state of the mirrors. The lens S2 collects the light power P_{PD1} representing the sampling pinhole via the +θ state of the micro-mirrors that directs the pinhole sampled light to point photo-detector PD1. Simultaneously, the –θ state optical power P_{PD2} from the DMD non-pinhole zone is collected by S3 and focused onto point photo-detector PD2. Next, the P_{PD1} optical power detected by PD1 is normalized with respect to the total detected optical power $P_{PD1}+ P_{PD2}$ to take into account any variations in irradiance during the scan of the pinholes on the DMD [2]. Hence, the normalized pinhole scan data power P_N provided by PD1 is given by $P_{PD1}/(P_{PD1}+ P_{PD2})$. Due to the high maturity of today's point photo-detector technology, the dual point detectors can handle very high optical dynamic ranges (e.g., > 120 dB) at fast data acquisition rates and hence the sensor can also operate with high dynamic ranges. As shown in Fig. 4.1, this normalized optical power reading signal from the pinhole scanning imager is electrically split into three paths, namely, a direct wired path to the processing unit, a second wired path with a 1 pixel or τ relative electrical delay time, and

a third wired path with a 2 pixel or 2τ relative electrical delay time. A 2×1 electrical switch controls whether the electrical signal representing the normalized pinhole scan optical power data is delayed by 1 pixel or 2 pixels before being sent to the processing unit for comparative electrical signal processing. The processing unit computes the absolute value of the difference between the no delay scan pixel power reading and the delayed (one pixel and two pixel delays) scan pixel power reading provided via the switched port. If this processed power reading is above a certain local threshold, e.g., a given percentage increase over the previous value power level defined by the user, edge detection is registered at this given DMD pinhole scan zone (i.e., pixel) location. Specifically, the location of this pixel on the DMD plane is stored in the control processor. In the case where the differenced power reading is below the threshold, no data is stored. This process continues until the whole image has been scanned by the DMD to enable locating the user defined edges in the target.

The DMD scans the irradiance pattern of the image plane by the smart scan method shown in Fig. 4.2. This smart scan method is designed to catch target edges (like the shaded gray rectangular target shown in Fig. 4.2) that would otherwise be missed if a classic line type horizontal or vertical scan is implemented on the DMD. The Fig. 4.2 smart scan method works as follows. Starting with pinhole location A

the optical power is measured and then the pinhole makes a vertical downward jump so that the pinhole is now at B. Next, the 2×1 switch is set so that the 1 pixel delayed power reading (i.e., power of A) is sent to the processing unit with the value of the power of B. The processing unit then detects whether there is an edge or not. Next the pinhole location moves to C and the 2×1 switch is set so that the 2- pixel delayed signal (i.e., power of A) is sent to the processing unit with the power of C. This step is effectively completes the basic unit of a horizontal scan. Then the pinhole moves to position D of the DMD pixel grid and the power levels of C and D pixel positions are compared. This process continues as shown by the arrows in the picture. In effect the smart scan process performs a combination of a horizontal scan and a vertical scan. Note that for the last row of pixels on the DMD, a classic straight horizontal scan is required to see if there are any horizontal edges from incident target at the bottom pixel row of the DMD. Note that only one DMD-based pinhole exists at any given time on the image plane to capture the actual optical irradiance map of the target and not some average or estimate of the target sparsely populated pixel map produced using many simultaneous pinholes to produce optically compressed sensed (CS) image data with additional interpolative CS algorithmic post-processing [120], [121].

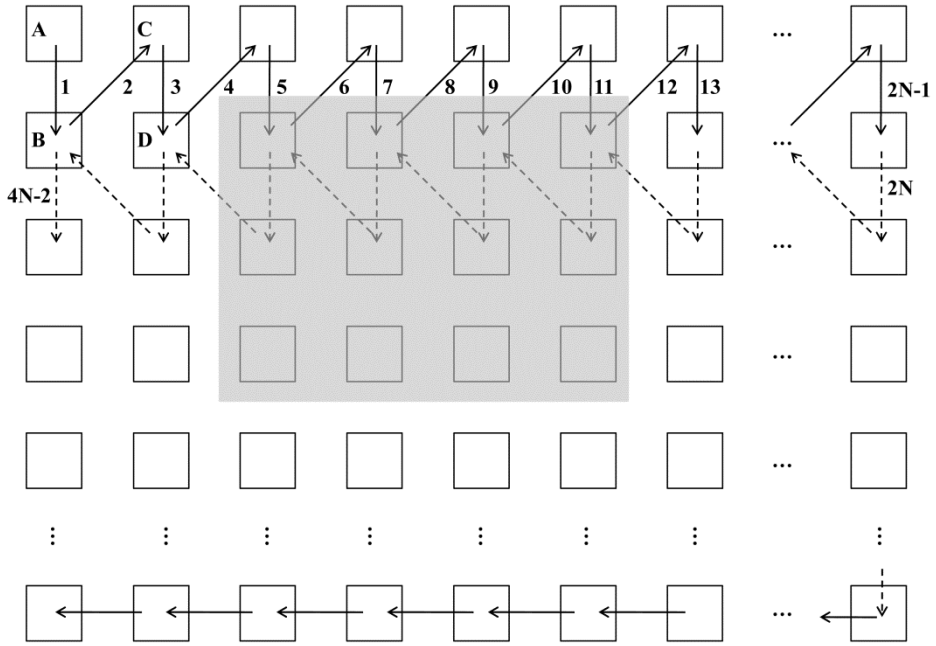

Fig. 4.2. The proposed smart DMD pixel scanning method for the edge detection sensor. The location of the shaded rectangle indicates a possible incident target image with boundaries that could match the axes of the 2-D DMD pixel grid.

The process of detecting an edge is implemented in the Fig. 4.1 sensor as follows. First the detected optical power is normalized to take into account bias light level variations coming from the target, such as those due to changes in sunlight levels or laser targeting source levels. Recall that the normalized optical detected power for the chosen pixel on the DMD pixel grid is given by:

$$P_N = \frac{P_{PD1}}{P_{PD1} + P_{PD2}}, \tag{4.1}$$

where P_{PD1} and P_{PD2} are the optical powers from PD1 and PD2, respectively. To register an edge, the threshold normalized power level T must satisfy the following equation:

$$T < | P_{N1} - P_{N2} | \ , \tag{4.2}$$

where P_{N1} and P_{N2} are the active scan pixel power level and the 2x1 switch provided time delayed pixel power level, respectively. Since $0 \leq P_N \leq 1$, T also ranges from 0 to 1. To determine T, two local threshold levels T_1 and T_2 are defined as:

$$T_1 = R\, P_{N1} \ , \tag{4.3}$$

$$T_2 = R\, P_{N2} , \tag{4.4}$$

where R is a user defined factor to control the required power level jump needed to register an edge. The R value can be manually set for controlled environments where the irradiance of the scene background and target object are well known such as in machine parts inspection and the laboratory experiment that is discussed later. One can also use an adaptive process for R value selection which will be studied in future

work. T_1 and T_2 are recomputed by the sensor processing unit for each scan pixel position in target image scan process since for any general target image, P_{N1} and P_{N2} values are image dependent. For each image scan location, T_1 and T_2 are compared and the lower threshold value is used as T in equation (4.2) to determine if an edge has been detected. In other words, $T_1 < T_2$ leads to $T=T_1$ and $T_1 > T_2$ leads to $T=T_2$. Note that if either T_1 or T_2 was used separately as the definition of T, a problem could occur in the edge detection process. Take for example the Fig. 4.3(a) case of a square target of uniform irradiance, which is brighter than the uniform background. Performing a classic horizontal scan, the first edge detected goes from low optical power (P_L) to high optical power (P_H) and the other side of the target will go from high power (P_H) to low power (P_L). If R = 0.5, P_L = 2 mW, and P_H = 3 mW and equation (4.3) alone was used as the definition for T in equation (4.2), then for the first edge one gets T = 1 mW and for the second edge T = 1.5 mW. Since $|P_H-P_L|$= 1 mW, only the first edge would be detected given the equation (4.2) condition must be met to register an edge. Thus, a problem occurs using a single local threshold value as only one of the edges is detected even though there is the same jump in power level at the second edge in the target image. Thus using equations (4.3) and (4.4) and taking the smaller threshold value, in this case of T = 1 mW at these uniform

background local scan positions, both target edges are registered by the defined sensor operation since both edge locations satisfy equation (4.2).

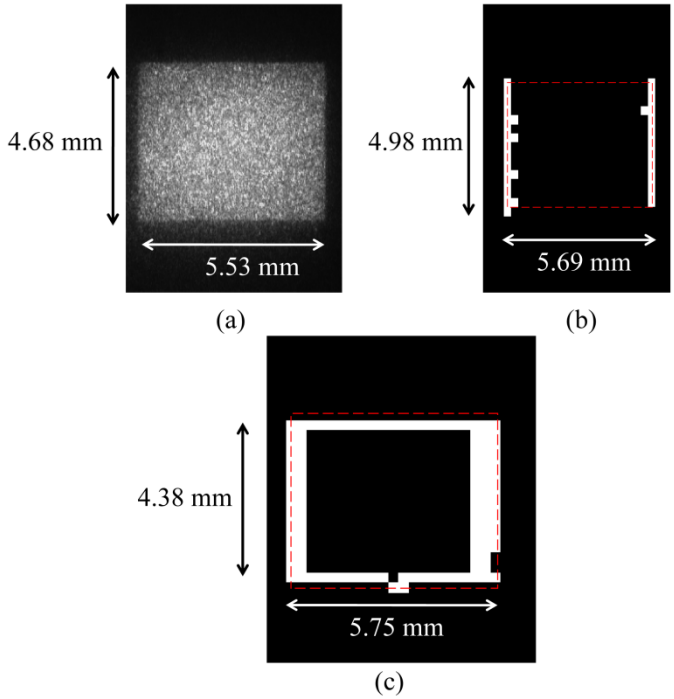

Fig. 4.3. (a) The CCD seen rectangular visible light target that is deliberately rotated such that the target's horizontal and vertical sides align with the horizontal and vertical axes of the DMD pixel grid. (b) The proposed optical attenuation-free sensor edge detection operation implemented using a classic horizontal scan method and (c) the proposed smart scanning method implemented in the sensor that then captures all the target edges. The dashed lines in (b) and (c) indicate the target boundary seen by the CCD when using optical attenuation of the target to prevent CCD saturation.

4.3 Experiment

The Fig. 4.1 sensor is implemented as a first-stage proof-of-principle experiment in the laboratory. An imaging lens S1 having a focal length of 15 cm is used but without the optional ECVFL given a fixed target situation. A visible band TI DMD is used which has 1024 by 768

micromirrors, a pixel pitch of 13.68 μm, and $\theta \pm .12$ Two Newport Model 918 detectors are used that are connected to a Newport 2931-C Power Meter. At present, given the non-custom PC-based hardware of the DMD scan control, the implementation of the electrical delays, switching, and the processing unit computations, i.e., normalization, differencing, and threshold comparison are done in non-real-time using the National Instruments (NI) LabView program. To generate the first luminous imaging object, a collimated 500 mW $\lambda = 532$ nm laser source with a 1.7 mW/cm^2 irradiance level is used to illuminate a rectangular target with a transparent diffuser. Fig. 4.3(a) is an optically attenuated CCD captured image of this optically scattering target at the plane where the DMD is located. The target size as measured by the CCD is 4.68 mm by 5.53 mm. Fig. 4.3(b) shows the detected target edges using the proposed DMD-based boundary mapping sensor when a classic horizontal scan is performed instead of using the Fig. 4.2 smart scan method. The dashed line indicates the actual boundary of the target. In this case, note that the DMD-based sensor does not detect the horizontal edges of the observed target. Similarly, if only a classic vertical scan is performed via the sensor, the vertical edges of the target are not detected. Next, using the smart scanning technique of Fig. 4.2, both the horizontal and vertical edges are detected and the boundary of the target is shown in Fig. 4.3(c). The pinhole size used for the smart scan is 20x20

micromirrors (i.e., 0.2736 mm by 0.2736 mm) and with R=0.45. The size of the object detected by the boundary scan is 4.38 mm by 5.75 mm, which closely matches the size of the target. Higher resolution boundary sensing can be achieved by reducing the size of the scanning pinhole below the presently used 0.2736 mm resolution. Since the experimental sensor operated in non-real-time via the NI LabView program and took approximately 18 minutes to implement its full object scan, the physical DMD-based optical scanning process was susceptible to vibrations in our laboratory environment where no air isolation table or special mechanical building noise reduction precautions were used. Future experiments will deploy an air isolation table. This pixel location sensitive vibration effect caused a few extra pixels to stick out of the sensor detected target edges as seen in Fig. 4.3(c). The experimental scan speed was presently limited as a computer running the LabView program was used to communicate with and process the information from DMD and power meter as opposed to using a faster embedded hardware implementation. Current DMD technology can achieve image reset speeds of 32,552 frames per second. Using a DMD with 1024 by 768 pixels and scan pinhole sizes of 15x15 micromirrors (i.e., 205.2 μm by 205.2 μm) and 5x5 micromirrors (i.e., 68.4 μm by 68.4 μm), the proposed processor image zone scan time is approximately 216 ms and 1.93 seconds, respectively. Improved DMD parallel processing

electronics is envisioned for future versions of advanced digital spatial light modulator technologies, thus providing near real-time image processor target boundary detection speeds that will also minimize pixel offset errors due to sensor platform vibrations or fast target motion blur.

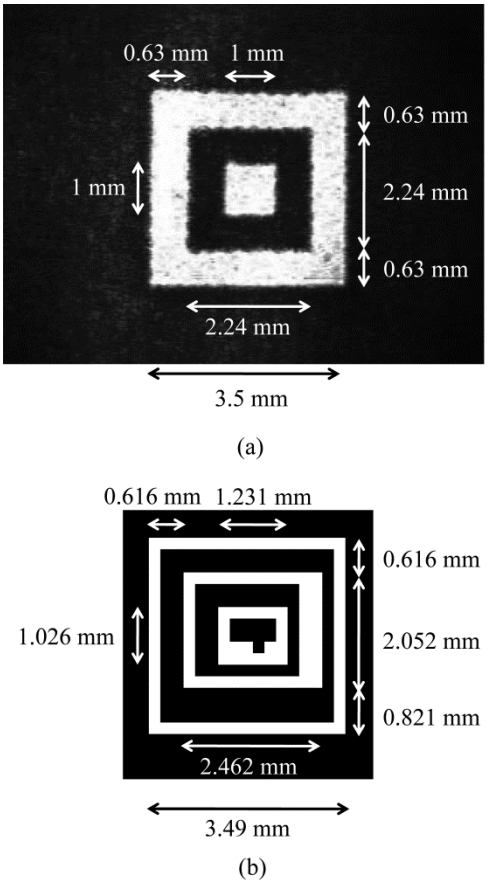

Fig. 4.4. (a) Optical attenuation engaged CCD observed test object with two separate bright areas indicating multiple boundaries and (b) the proposed sensor optical attenuation-free experimentally mapped edges of the test object using the smart scan method. The white zone indicates the presence of a target edge in the image.

For the next demonstration, the rectangular target is replaced by a square frame target with a small square placed inside it. As shown in Fig. 4.4(a), this target's center square side length is 1 mm with the dark

border being 0.62 mm and the bright border being 0.63 mm, giving the outer target square a length of 3.5 mm. This target is illuminated by a λ = 632.8 nm HeNe laser source which has a target plane irradiance of 0.72 mW/cm^2. Fig. 4.4(b) shows the sensor recovered boundaries of the target using the smart scan method. The pinhole size used for scanning was 15x15 micromirror (0.2052 mm by 0.2052 mm) with R = 0.6. As can be seen from Fig. 4.4(b), the demonstrated sensor detects the correct number of target boundaries, mapping the multiple areas of high optical irradiance with a spatial resolution of 0.2052 mm. The first white rectangular frame traces the outermost edge of the target. The second white rectangular frame is the edge between high intensity frame and the low intensity frame surrounding the central square. The innermost white rectangular frame is the detected edge of the square in the middle of the target. The outer length of the target detected from the boundary sensor is 3.49 mm. The asymmetry in the detected target boundary lines is due to the asymmetric overlay of the target image on the chosen DMD scan pixel grid. Specifically in the present experiment, image zones where the areas of high irradiance fell partially on one pixel and fully on the next pixel, a double line occurred. This is due to the size of the chosen pinhole and using a finer scanning pinhole will reduce the image overlay alignment error. In addition, programmable ECVFL powers can be deployed to minimize grid alignment errors.

4.4 Conclusion

For the first time, to the author's knowledge, a novel edge detection sensor using a DMD-based 3-D irradiance mapper and real-time pixel differencing hardware is proposed. A basic experiment has been conducted successfully to demonstrate boundary detection of a rectangular target and a framed square target for visible wavelengths of 633 nm and 514 nm. The proposed sensor features a high optical dynamic range, minimal data processing overhead, intelligent edge processing via smart scans and programmable lenses, and multispectral capabilities for image fusion applications [123]. Applications for the sensor are diverse and range from medical imaging to military and security sensing arenas. Future work relates to the real-time implementation of the overall proposed sensor and its comparison with traditional image processing methods.

http://dx.doi.org/10.1109/JSEN.2011.2172410

CHAPTER 5

POWER SMART IN-DOOR LINE-OF-SIGHT OPTICAL WIRELESS LINK

5.1 Introduction

It was realized in the late 1970's that diffused Infrared (IR) light, much like Radio Frequency (RF) radiation filling a room could be used for wireless data communications [32]. This indoor optical wireless technique is also known as the Diffused Infrared Radiation (DFIR) and is very effective in preventing physical blocking of light to the receiver and tolerant to transmitter/receiver mobility. Since this method uses scattered light in a room, it is highly power inefficient and also limits achievable data rates due to multipath effects. To counter these limitations of the DFIR indoor wireless method, highly directional light beam communication, also known as Line-of-Sight (LOS) infrared communications or the Directed-beam IR (DBIR) technique, was proposed and demonstrated [33], [34]. Today, wireless optical communications is still an active area of research [40], [41], [42].

The use of agile spatially reconfigurable laser beams has been previously proposed for space (i.e., inter-satellite) [124] and indoor wireless applications [37]. Specifically, reference [37] proposed a new hybrid indoor optical wireless method, now called Hybrid Diffused-LOS [40], as it is a combination of the DFIR and DBIR methods. Earlier, a smart free-space link design was proposed and theoretically analyzed for a variety of link ranges varying from short indoor applications [49] to long distance inter-satellite links [125], [126]. In particular, these smart link designs use Transmitter (T) and Receiver (R) electronically agile beam conditioning lens optics that adjust focus based on specific link distance requirements for a given scenario. Within the framework of paraxial optics and beamforming optics device limits, one is able to produce a zero propagation link coupling loss design for a given range of link distances. Recent advances in micro-devices such as laser modules, micro-lenses, Electronically Controlled Variable Focus Lenses (ECVFLs), and Micro-Electro-Mechanical Systems (MEMS) beam directing micro-mirrors points to the realization of a new higher compactness micro-optics scale optical wireless T and R modules that can be readily adapted for use in a smart indoor low loss application link design. For example, the emergence of low cost visible light laser pointers and laser scanning based colour projection displays points to the applicability of low power visible laser sources for indoor optical

wireless link applications. Note that presently, visible light-based indoor wireless communications is considered to be an excellent alternative to IR-based optical wireless, given that visible light usage has benefits such as low cost sources, e.g., white light emission Light Emitting Diodes (LEDs) [44], [127], [128], [129], smaller T and R apertures via use of shorter wavelengths and easier beam alignment due to human and visible CCD camera observation of free-space beams. In addition, low cost visible laser pointers have become available with good beam divergence and beam shape properties. These can be exploited for short range indoor optical wireless links such as the one attempted in this chapter. Nevertheless, one must be careful about eye safety issues when using visible laser-pointer style sources. Hence visible laser power levels should be restricted to low power safe levels such as is done in laser scanning pico-display applications [130]. Given that proposed smart optical link design provides the lowest propagation loss between a transmitter and receiver, the lowest laser power needed can definitely be used for a particular bit rate, thus helping the visible light eye safety issue.

Hence, this chapter will focus on visible laser pointer-like sources for link design, although other eye safe band (e.g., 780 nm, 850 nm, 1300 nm, and 1550 nm) laser sources can also be applied to the proposed smart link concept. The key innovation proposed in this chapter is the

use of the ECVFL to adjust beam parameters for low loss operations with changing link distances as well as use of the ECVFL controlled wide area search beam to initially align the transmitter with the receiver. The rest of the chapter describes the smart link design and a basic visible light proof-of-principle link design experiment.

5.2 Proposed Smart Optical Wireless Link

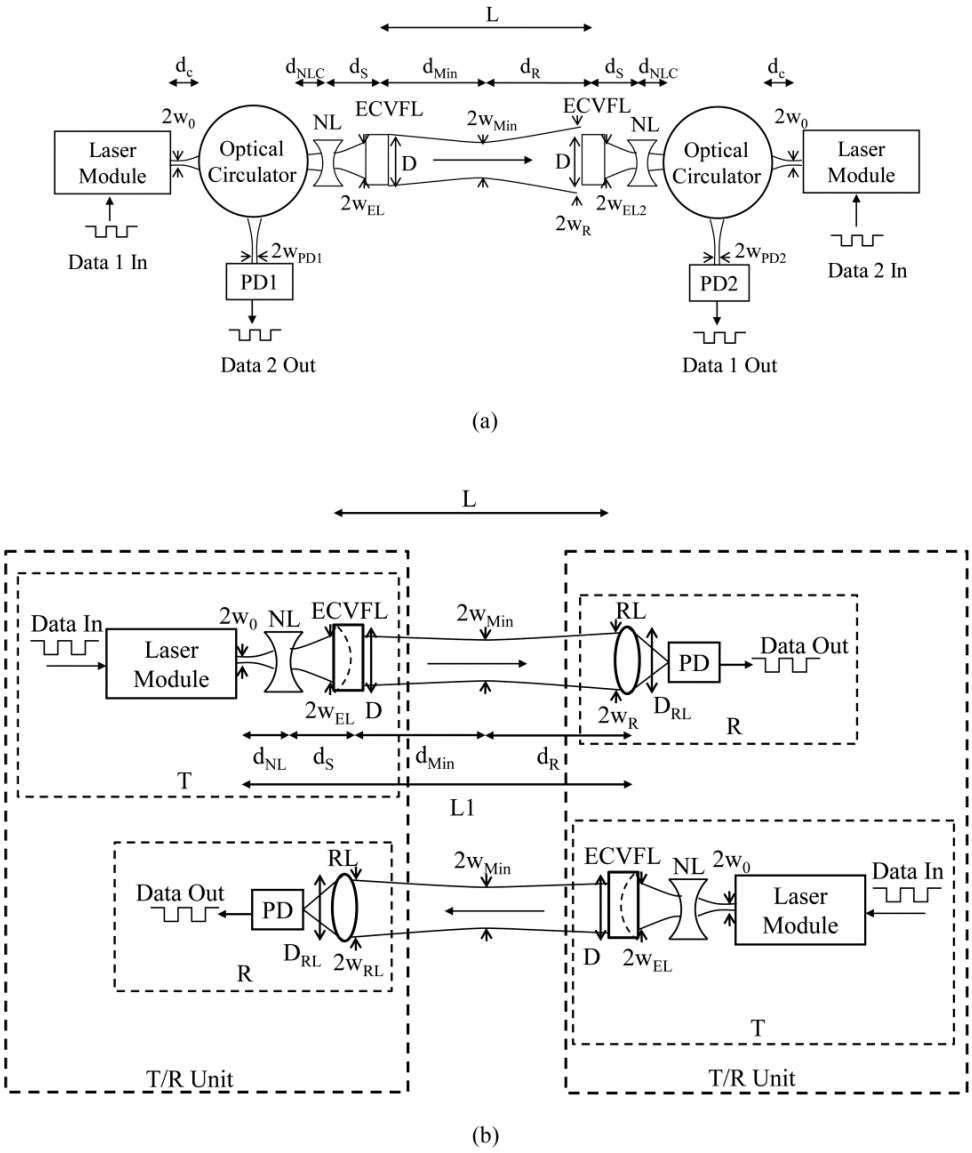

Fig. 5.1. The proposed smart wireless optical data communication link designs. (a) Common Transmit (T) and Receive (R) aperture smart T/R module design. (b) Independent T and R apertures smart T/R module design.

Fig. 5.1 shows the proposed compact and power smart optical wireless link design using two independent transceiver or T/R units. Fig. 5.1(a) link design allows simultaneous T and R communications via a common T/R aperture that uses a FSO circulator device to physically separate the T and R beam paths in each T/R unit. The transmit data signal in Fig. 5.1 electrically modulates the laser module. The received data signal is produced by the photodetector in the T/R unit. The T and R beams are spatially conditioned by the concave lens and the ECVFL in the T/R unit. The concave lens (also called the Negative Lens or NL) of focal length f_{NL} is used to produce beam expansion of the Gaussian beam from the laser module so that the laser light completely illuminates the ECVFL aperture. Typically, the aperture of the ECVFL and other micro-optics in the T/R unit do not exceed a 5 mm diameter, giving a pencil-like compact design to the proposed T/R units. The ECFVL's focal length F, is controlled by an electrical signal (e.g., voltage level or drive frequency) which in-turn controls the minimum beam waist diameter $2w_{Min}$ and its position d_{Min} with respect to the transmitter beam ECVFL location. Depending on the link distance L, F can be controlled to produce the desired Gaussian beam propagation such that it exhibits the self-imaging effect between the two communicating T/R units and thus forms a zero propagation loss link. Other notations for Fig. 5.1 are as follows: w_0: minimum beam waist radius of the laser; w_{EL}: beam waist

radius at the transmit ECVFL; w_{EL2}: beam waist radius after the receive ECVFL; w_R: beam waist radius at the receive ECVFL; w_{PD1}: beam waist at Photo-Detector 1 (or PD1); w_{PD2}: beam waist at Photo-Detector 2 (or PD2); d_c: distance from $2w_0$ position to optical circulator; d_{NLC}: distance from optical circulator position to NL; d_{NL}: distance from $2w_0$ position to NL; d_S: distance from NL to the ECVFL; d_{Min}: distance from the ECVFL to the $2w_{Min}$ position; d_R: distance from $2w_{Min}$ location to the T/R unit receiving the ECVFL conditioned laser beam; D: diameter of ECVFL aperture for a symmetrical link providing the designed lossless beam propagation operations, $d_R = d_{Min}$. The Fig. 5.1(a) link can also be operated in an asymmetrical design where d_R is not equal to d_{Min}. The asymmetrical case where $d_R > d_{Min}$ implies that the beam diameter at the receiving ECVFL lens is larger than the ECVFL diameter at the distant T/R unit; therefore the zero loss condition will not be met, leading to incrementally higher light propagation loss as d_R exceeds d_{Min}. Fig. 5.1(b) shows an alternate link design with two T/R units communicating with physically separate T and R optical apertures. Due to this effect each T/R unit contains physically separate transmitter and receiver modules. D_{RL} is the diameter of the receiver capture lens RL. The Fig. 5.1(b) T/R unit design is suitable when high optical isolation (> 25 dB) is required between the T and R channels and when during an asymmetrical link operation, additional receive light capture is desired

via a receive lens aperture size that exceeds the typical small ECVFL diameter.

The smart link designs can be analysed using ABCD matrix analysis of Gaussian beams. The results of this analysis are presented here, but readers can refer to [131] for details on the derivations. Using ABCD analysis for the setup of Fig. 5.1(b), the beam waist at any location is given as:

$$w(z) = \sqrt{\frac{\lambda}{\pi}\frac{\left(Az_0\right)^2 + B^2}{z_0}}\,. \tag{5.1}$$

where λ is the wavelength of light, z_0 is the Rayleigh range of the laser and A and B are elements of the ABCD matrix. To find w_{EL}, equation (5.1) is used with the ABCD matrix that describes the laser beam propagation to that point where:

$$\begin{bmatrix} A & B \\ C & D \end{bmatrix} = \begin{bmatrix} 1-\frac{d_s}{f_{NL}} & d_s + d_{NL} - \frac{d_s d_{NL}}{f_{NL}} \\ -\frac{1}{f_{NL}} & 1-\frac{d_{NL}}{f_{NL}} \end{bmatrix} \tag{5.2}$$

When a minimum beam waist is formed, the real part of the q-paramteter is zero. Using ABCD Gaussian beam optics leads to:

$$ACz_0^{\,2} + BD = 0\,. \tag{5.3}$$

Now substituting the appropriate ABCD elements for Fig. 5.1(b) gives:

$$aF^2 + bF + c = 0\,, \tag{5.4}$$

where:

$$\begin{aligned} a = \Big[& z_0{}^2 \left(d_{Min} + d_S - f_{NL}\right) + d_{NL}{}^2 \left(d_S + d_{Min} - f_{NL}\right) \\ & + f_{NL}{}^2 \left(d_{NL} + d_S + d_{Min}\right) - 2 d_{NL} f_{NL} \left(d_S + d_{Min}\right) \Big] \end{aligned}$$

$$\begin{aligned} b = \Big[& z_0{}^2 \left(2\left[f_{NL}\left(d_S + d_{Min}\right) - d_S d_{Min}\right] - d_S{}^2 - f_{NL}{}^2\right) \\ & + 2 d_{NL}{}^2 \left(d_S f_{NL} + f_{NL} d_{Min} - d_S d_{Min}\right) \\ & - 2 f_{NL}{}^2 \left(d_{NL} d_S + d_{NL} d_{Min} + d_S d_{Min}\right) + 4 f_{NL} d_{NL} d_S d_{Min} \\ & + 2 d_{NL} d_S{}^2 f_{NL} - f_{NL}{}^2 \left(d_{NL}{}^2 + d_S{}^2\right) - d_{NL}{}^2 d_S{}^2 \Big] \end{aligned} \tag{5.5}$$

$$\begin{aligned} c = \Big[& d_{Min} z_0{}^2 \left(d_S{}^2 + f_{NL}{}^2 - 2 d_S f_{NL}\right) \\ & + 2 d_{NL} d_S d_{Min} \left(f_{NL}{}^2 - f_{NL} d_{NL} - f_{NL} d_S\right) \\ & + \left(d_{NL} d_S\right)^2 d_{Min} + f_{NL}{}^2 d_{Min} \left(d_{NL}{}^2 + d_S{}^2\right) \Big] \end{aligned}$$

Note that larger input beam sizes allow for a larger achievable link distance.

Now the T/R unit link design parameters f_{NL}, d_{NL}, d_S, and d_{Min} should be chosen such that the beam radius w_{EL} described by equation (5.1) is smaller than the radius of the ECVFL. Then equation (5.4) can be solved to give:

$$F = \frac{-b \pm \sqrt{b^2 - 4ac}}{2a}\,. \tag{5.6}$$

Since F should be real, $b^2 \geq 4ac$ for a valid link design. The choice of F will determine the size of the minimum beam waist along with the other

system parameters. Note that the focal length of all lenses in the system must satisfy F# ≥ 1.67 [125] since this analysis is done within the paraxial approximation. Using the two solutions obtained for F, one solves for the minimum beam waist w_{Min} as follows:

$$w_{Min} = \sqrt{\frac{\lambda}{\pi}\frac{z_0}{[Cz_0]^2 + D^2}} \tag{5.7}$$

where

$$\begin{bmatrix} A & B \\ C & D \end{bmatrix} = \begin{bmatrix} 1 & d_{Min} \\ 0 & 1 \end{bmatrix} \times \begin{bmatrix} 1 & 0 \\ -\frac{1}{F} & 1 \end{bmatrix} \times \begin{bmatrix} 1 & d_s \\ 0 & 1 \end{bmatrix} \times \begin{bmatrix} 1 & 0 \\ -\frac{1}{f_{NL}} & 1 \end{bmatrix} \times \begin{bmatrix} 1 & d_{NL} \\ 0 & 1 \end{bmatrix}, \tag{5.8}$$

The size of w_{Min} should be real and less than w_{EL}. Since the purpose of the proposed communication link is to achieve low optical power loss, the solution for F that gives the lowest transmit aperture beam divergence should be used. Although both F solutions have the same loss in the symmetric link case, having a smaller beam divergence reduces the link loss for distances of $d_R > d_{Min}$. Since it is known that the divergence is inversely proportional to the minimum beam waist [131] the F solution that gives the larger w_{Min} minimum beam waist value will give the smaller transmit beam divergence and thus a reduced power loss if $d_R > d_{Min}$. In order to find the beam waist radius at the receiving lens, the ABCD analysis is applied from w_0 to w_R for Fig. 5.1(b) giving:

$$\begin{bmatrix} A & B \\ C & D \end{bmatrix} = \begin{bmatrix} 1 & L \\ 0 & 1 \end{bmatrix} \times \begin{bmatrix} 1 & 0 \\ -\frac{1}{F} & 1 \end{bmatrix} \times \begin{bmatrix} 1 & d_s \\ 0 & 1 \end{bmatrix} \times \begin{bmatrix} 1 & 0 \\ -\frac{1}{f_{NL}} & 1 \end{bmatrix} \times \begin{bmatrix} 1 & d_{NL} \\ 0 & 1 \end{bmatrix} \tag{5.9}$$

Substituting the elements of equation (5.9) into equation (5.1) gives w_R. For low smart link propagation loss, this beam waist radius w_R should be smaller than the diameter of the receiving lens. For the case of a symmetric link, the beam waist at the output of the transmitting ECVFL and the size of the beam at the receiving lens should be the same. Similarly, the equations for Fig. 5.1(a) could be derived given the ABCD matrix of the optical circulator used. The smart link beam propagation can be compared to unconditioned Gaussian beam propagation over the distance $L1$, where $L1 = d_{NL} + d_S + L$. The beam waist for the unconditioned Gaussian beam is given by [131]:

$$w_N(z) = w_0\sqrt{1+\left(\frac{L1}{z_0}\right)^2}\ . \tag{5.10}$$

Now that the beam waist at the receiver location for the smart link and unconditioned Gaussian beam propagation-based link are known, the advantage of the proposed smart link design in terms of optical power at the receiving aperture of the T/R unit can be analyzed. For a Gaussian beam, the receive aperture collected optical power is given by integrating the irradiance over the area of the receiving aperture giving:

$$P(z) = \int_0^{2\pi}\int_0^{a} I_0\,\frac{{w_0}^2}{w^2(z)}\,e^{-\frac{2r^2}{w^2(z)}}\,r\,dr\,d\phi = 2\pi\int_0^{a} I_0\,\frac{{w_0}^2}{w^2(z)}\,e^{-\frac{2r^2}{w^2(z)}}\,r\,dr\ . \tag{5.11}$$

where I_0 is the laser beam peak intensity at the w_0 location at the exit of the laser module, $w(z)$ is the beam waist at a specific location given by substituting equation (5.9) into equation (5.1) for the smart link and by equation (5.10) for the unconditioned Gaussian beam, and a is the radius of the receiving aperture, i.e., the receiving lens in the T/R unit. To compare the results of the smart link and the unconditioned Gaussian beam propagation link, equation (5.11) can be normalized as follows:

$$P_{Norm}(z) = \frac{\int_0^a e^{-\frac{2r^2}{w^2(z)}} r dr}{\int_0^\infty e^{-\frac{2r^2}{w^2(z)}} r dr}. \tag{5.12}$$

Hence, the normalized percentage optical power loss for the FSO link is given by:

$$P_{Loss}(z) = 100\left[1 - P_{Norm}(z)\right]. \tag{5.13}$$

5.3 Experimental Demonstrations

Using the Fig. 5.1(b) link design, a proof of concept demonstration of the smart indoor optical wireless link design is implemented for a visible laser pointer-type source. Since the focus of the chapter is optical propagation loss reduced link design, an unmodulated laser is deployed. It is well known that direct or indirect modulation of today's visible laser diodes is readily possible for high (> 100 Mbps) data rates. Today, a

typical laser pointer module for red light has a beam divergence half-angle of 0.6 mrad and a Gaussian minimum beam waist radius w_0 of 0.5 mm. The visible source deployed has similar characteristics and is a Melles Griot Model 05-LHP-991 10 mW He-Ne laser with $\lambda = 632.8$ nm a beam divergence of 0.62 mrad and $1/e^2$ beam radius $w_{0,}$ of 0.325 mm. Specifically, for the experiment a symmetric (i.e., $w_{EL} = w_{RL}$) agile link is designed with a typical indoor room range of L = 4.01 m where $L = L1-(d_{NL} + d_S)$. The ECVFL used in the link is a Varioptic (France) Aortic Model 320 liquid lens with a D = 3 mm aperture. This ECVFL is a broadband visible light variable focus lens that uses electrowetting technology. Expansion of the laser module beam waist for higher beam collimation is implemented using the concave lens (or NL) that has a f_{NL}= -15 cm. Since the diameter of the ECVFL is 3 mm, the NL and ECVFL are placed with a d_{NL} = 16.55 cm and d_S = 23 cm such that the $1/e^2$ beam diameter at the ECVFL input plane is less than the ECVFL aperture. Specifically, the $1/e^2$ beam diameter $2w_{EL}$ at the ECVFL input plane is chosen to satisfy D= 1.67 x $2w_{EL}$ that corresponds to the ECVFL 3 mm diameter aperture capturing 99.6% of input light intensity with a theoretical w_{EL} = 899.5 μm. Using link design equation (5.4) and solving for d_{Min} gives L = 0.1 m for the shortest positive ECVFL focal length F = 4.4 cm. Using link design equation (5.4) and solving for F for a desired link distance L = 4.1 m gives F = 33.44 cm for the ECVFL.

Note that the deployed ECVFL can be electronically controlled from a negative lens with F= - 19.9 cm to a positive lens with a range of F = 4.4 cm to F = 40 cm. In the experiment, F is controlled by varying the duty cycle from 82.2% to 84.4% for the 40 kHz frequency pulsed wave drive signal. For example, the ECVFL focal lengths are 36.62 cm, 36.3 cm, and 33.4 cm for duty cycles of 82.4%, 82.64%, and 83.12%, respectively. As a moving wireless terminal or agile FSO link connection changes the deployed link distance, the ECFVL F is changed to maintain the lossless link propagation self-imaging condition between the transmit and receive optical terminals. In order to test this smart link idea, a receiver in the form of a laser beam profiler is positioned at the changing L distances to record the receive plane incident laser beam size. Using a highly accurate Digital Micromirror Device (DMD) based beam profiler [67], one can accurately measure the Gaussian beam size and then compute the captured power using equation (5.11) for a given receive lens aperture. In addition, to visualise the effect of the different beam sizes on the receiver plane, a standard visible light CCD camera is used to observe the smart link agile beam.

The percentage optical power loss P_{Loss} due to beam propagation for the wireless optical link is given by equation (5.13). Fig. 5.2 shows the designed percentage optical power loss for the two types of links. Fig. 5.2 was produced using equations (5.12) and (5.13) with equation (5.9)

substituted into equation (5.1) for the smart link and equation (5.10) for the non-smart link conditions. Note that given the deployed ECVFL has a D = 3 mm, the receive aperture radius used for the link receiver lens is set to a=D/2=1.5 mm for equation (5.12). The design plots assume zero transmission and reflection loss for the NL and ECVFL given that these optics can be Anti-Reflection coated for the laser wavelength. Results from the conducted experiment with non-AR coated optical elements shows that the optical losses were 10% and 7% for the NL and ECVFL, respectively. In order to obtain the received optical power measurement, a 3 mm diameter iris is placed just before the 1 cm^2 active area receive photo-detector (Newport 918D-UV) to make an aperture diameter equivalent to the ECVFL aperture. Data points on the Fig. 5.2 plots are shown assuming zero-loss components. Fig. 5.2(a) shows that for the changing link distance *L* from 1 m to 4 m, the experimental smart link provides a low < 7 % optical percentage loss compared to the non-smart link with an experimental 59.07% and theoretical 55.2% loss at *L* = 4 m. Thus a 53.04% improvement over the non-smart link was experimentally observed at L = 4 m. Ideally, the smart link loss should be zero, but experimental non-ideal behaviour of the Varioptic ECVFL (e.g., aberrations, coma, etc) and laser beam Gaussian quality restrict the link performance to meet ideal design theory. Improvements in demonstrated link loss can be achieved by using higher optical and beam quality optics

(i.e., laser and ECVFL) for the smart link. Given that link distances could exceed the designed 4 m smart link distance, Fig. 5.2(b) shows the designed and measured optical loss percentage values for the non-smart and smart wireless optical links operating outside the designed 4 m agile self-imaging range of the link. The low loss benefits of the smart link are clear and shown for link distances up-to 15 m. Data shows that at 15 m, the non-smart link percentage loss is 92.8 % versus the 61.5% for the smart link. In the smart link case, *F* is set for a 4 m link distance.

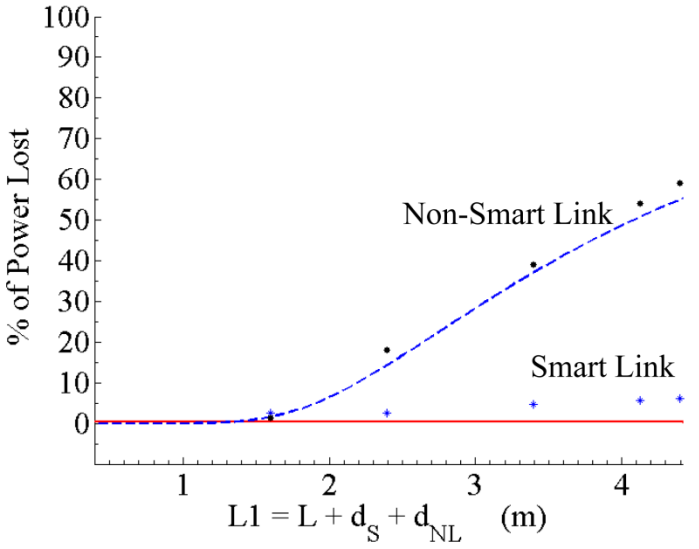

(a)

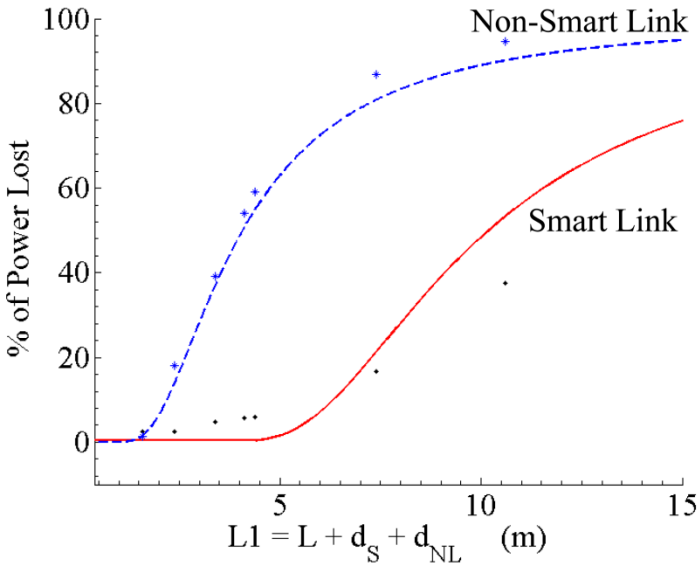

(b)

Fig. 5.2. (a) Shown are the designed and measured optical loss percentage values for the non-smart and smart wireless optical links operating within the designed 4 m agile self-imaging range of the link. The design assumes a 3 mm diameter receive lens that matches the 3 mm diameter of the transmit ECVFL. (b) shows the designed and measured optical loss percentage values for the non-smart and smart wireless optical links operating outside the designed 4 m agile self-imaging range of the link.

Additional range symmetric links can be designed where the link range is defined between the L distance limits of $L_{min} \leq L \leq L_{max}$. For example, a goal can be to design a link with 5 m$\leq L \leq$ 10 m range using hardware such as a laser module with λ = 632.8 nm and w_0 = 500 μm, and a NL with f_{NL} = -10 cm. For the T/R module design, d_{NL} should be less than the Rayleigh range z_0 as then the choice of d_{NL} has a minimal effect on w_{EL}. In order to preserve the compact design, d_{NL} is chosen to be 1 cm. An initial estimate for w_{EL} is made by using $w_{EL} = \sqrt{\lambda L_{max} / \pi}$; this leads to an initial estimate of w_{EL} = 1.42 mm for 10 m link range. Using equation (5.2) to solve equation (5.1) for an initial estimate of d_s it is found to be 27.06 cm. The calculated value of d_s along with the other design parameters and $d_{Min} = L_{max}/2$ = 5 m are substituted into equations (5.5) and (5.6) to provide a value for F that in this case comes out to be imaginary. As F was an imaginary value, increasing the estimate for d_s to 27.43 cm results in the value F to become positive and equal to F = 40.61 cm or F = 40.51 cm. Alternatively if a positive value for d_s is obtained, one can decrease d_s till it cannot be decreased further without F becoming imaginary. Note that the ECVFL chosen must satisfy the condition $2w_{EL}$ < D. Solving equations (5.4) and (5.6) with $d_{Min} = L_{min}/2$ = 2.5 m gives F = 41.8 cm or F = 36.51 cm. Using equations (5.7) and (5.8), the w_{Min} for each focal length pair can be compared. Note that though both solutions of F are valid, the solutions of F that give the

larger w_{Min} (via the longer F value) are chosen as they have less divergence and thus a smaller beam waist when $d_R > d_{Min}$ allowing for low loss link operations when $L > L_{max}$. Hence, the ECVFL for the designed 5 m to 10 m link requires operations with 40.61 cm$\leq F \leq$ 41.8 cm, an achievable ECVFL device performance. The length of the example smart transmit module is given by $d_{NL} + d_S$ = 27.06 cm + 1 cm = 28.06 cm. In comparison, when using the reference [125], [126] low loss wireless link module design for the same design specifications, i.e., L_{min} = 5 m, L_{max} =10 m, w_{EL} = 1.42 mm, λ = 632.8 nm, w_0 = 500 μm, a fixed focal length convex collimating lens of 3.52 m focal length is required to give equivalent values of $d_{NL} + d_S$ = 3.52 m+ 3.52 m =7.04 m with the ECVFL focal length variation from 2.68 m $\leq F \leq$ 10 m. The prior reference [125] module design for a typical visible laser pointer-like source fed low loss link results in a much longer module size in addition to requiring an ECVFL with a larger dynamic range for focal length control. The proposed module design in Fig. 5.1 is highly compact and deploys highly engineered micro-optic components for optimal low loss wireless link designs. The T/R module design in [125], [126] is more suited for Single-Mode Fibre (SMF)-to-freespace coupled light transmission and detection within the module as it uses the much smaller SMF core size w_0 values like $2w_0$ = 9 μm for the 1550 nm near

IR wavelength typical for long distance telecommunications fibre networks.

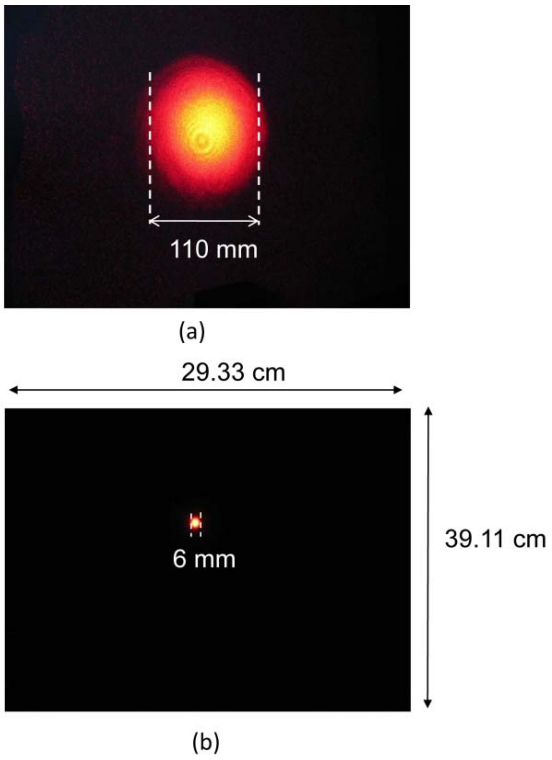

Fig. 5.3. Shown are CCD camera images (at uniform same scale) of the smart link operating in its wide area search beam mode for a link distance parameter of L1 = 280.5 cm. (a) Search beam shown using ECVFL F = 4.4 cm. (b) Non-smart link receive beam.

An important feature of the proposed smart link is its ability to provide a wide area big search beam to establish a search and hand-shake operation with another remote receiving T/R unit. The search mode operation can be achieved by operating the ECFVL as a short focus convex lens so as to spread out the transmit beam into a wider zone to locate a possible T/R unit. Upon establishing an initial detection with a remote T/R unit, the ECVFL focal length is brought to a longer

convex focal length for optimal low loss smart link operations. Fig. 5.3 shows CCD camera images (at uniform scale) of the smart link operating in its wide area search beam mode for a link distance parameter of $L1$ = 280.5 cm. Fig. 5.3(a) shows the 11 cm diameter search beam obtained using ECVFL F = 4.4 cm. and Fig. 5.3(b) shows the non-smart link received beam. The Fig. 5.3 data indicates that using the present liquid lens ECVFL, a search beam that is approximately 18 times bigger in diameter than the unconditioned non-smart link beam can be generated, giving excellent beam search capabilities. In addition, the expanded search beam mode can be used to create spatially controlled cells for optical illumination in an indoor wireless scenario.

5.4 Conclusion

In conclusion, a power smart optical wireless link design is presented for low loss indoor operations with changing link distances. The smart link design uses fixed focal length optics in combination with an ECVFL to adjust Gaussian minimum beam waist location and size for ideal zero propagation loss receive beam capture. The proposed low loss link can be beneficial to energy saving communication operations, for example, in portable devices and data centres where maximum data rates must be sent with minimal power usage. A visible laser smart wireless link is demonstrated for a variable 1 m to 4 m link distance. The spatially

conditional link achieved a < 7 % optical propagation loss over the 4 m range and showed a 53% improvement over an unconditioned laser link. The smart link has the ability to provide a wide area search beam for search and hand-shake operations with other receiving T/R units, easing alignment procedures and beam blocking instances. Future work relates to smart link demonstrations with high data rates.

http://dx.doi.org/10.2971/jeos.2011.11054

CHAPTER 6

SMART MULTIPLE MODES INDOOR OPTICAL WIRELESS DESIGN AND MULTI-MODE LIGHT SOURCE SMART ENERGY EFFICIENT LINKS

6.1 Introduction

Indoor optical wireless communications is an attractive alternative to radio frequency (RF) wireless, including its ability to easily achieve high data rates within an unregulated spectrum [35], [41], [42], [43], [129], [132]. Recently, proposed is the concept of smart indoor visible LOS optical wireless links [51], [133], [134]. The idea behind the smart designs in references [51], [133], [134] is to use the ECVFLs to form a Three Dimensional (3-D) laser beam so that the receiver captures as many transmitted photons as possible [125], [126]. Thus the issues of poor use of limited light energy and limited range are relieved, enabling the optical wireless link to smartly adapt to changes in range to allow for a higher SNR or a reduction in the transmitted optical power. However, since these previously suggested smart link designs are LOS, they are prone to physical blocking. While increasing the number of LOS transmitters [37] does reduce the probability of blocking in a wireless system, it does not achieve the robustness to blocking inherently provided by diffuse [32] or spot diffused [32], [38], [39] light optical

wireless links. Non-LOS links also have the advantage in terms of connecting moving users [135]. Additionally, in today's environment where the number of mobile users and bandwidth of content is increasing, reliable non-blocking high data rate links are increasingly important.

To address these issues, recently proposed is a smart dual mode energy efficient optical wireless data link [136]. While the dual-mode optical wireless system proposed can smartly adapt to changes in link length, number of users, and bandwidth usage, it did not take full advantage of the robustness to blocking, control of bandwidth, or coverage area control that can be achieved using smart optical wireless. It would be beneficial if an optical wireless system could be designed that can smartly adapt to changes in its environment, i.e., link length and physical blocking and the application, i.e., bandwidth usage, number of users, user mobility, and coverage area. Such a smart system would improve the quality of service and reduce the power consumption of optical wireless networks and is the first focus of this chapter. Spatially multi-mode light sources such as LEDs and lasers are high reliability economical components for large scale deployment in industrial settings. Previously, the smart link [51] was demonstrated using single spatial mode lasers. Hence, the second focus of this chapter is to demonstrate the feasibility of using multi-mode LEDs and lasers with ECVFLs to

implement 3-D optical beamforming required to implement smart energy efficient links.

6.2 Proposed Smart Multiple Modes Optical Wireless Design

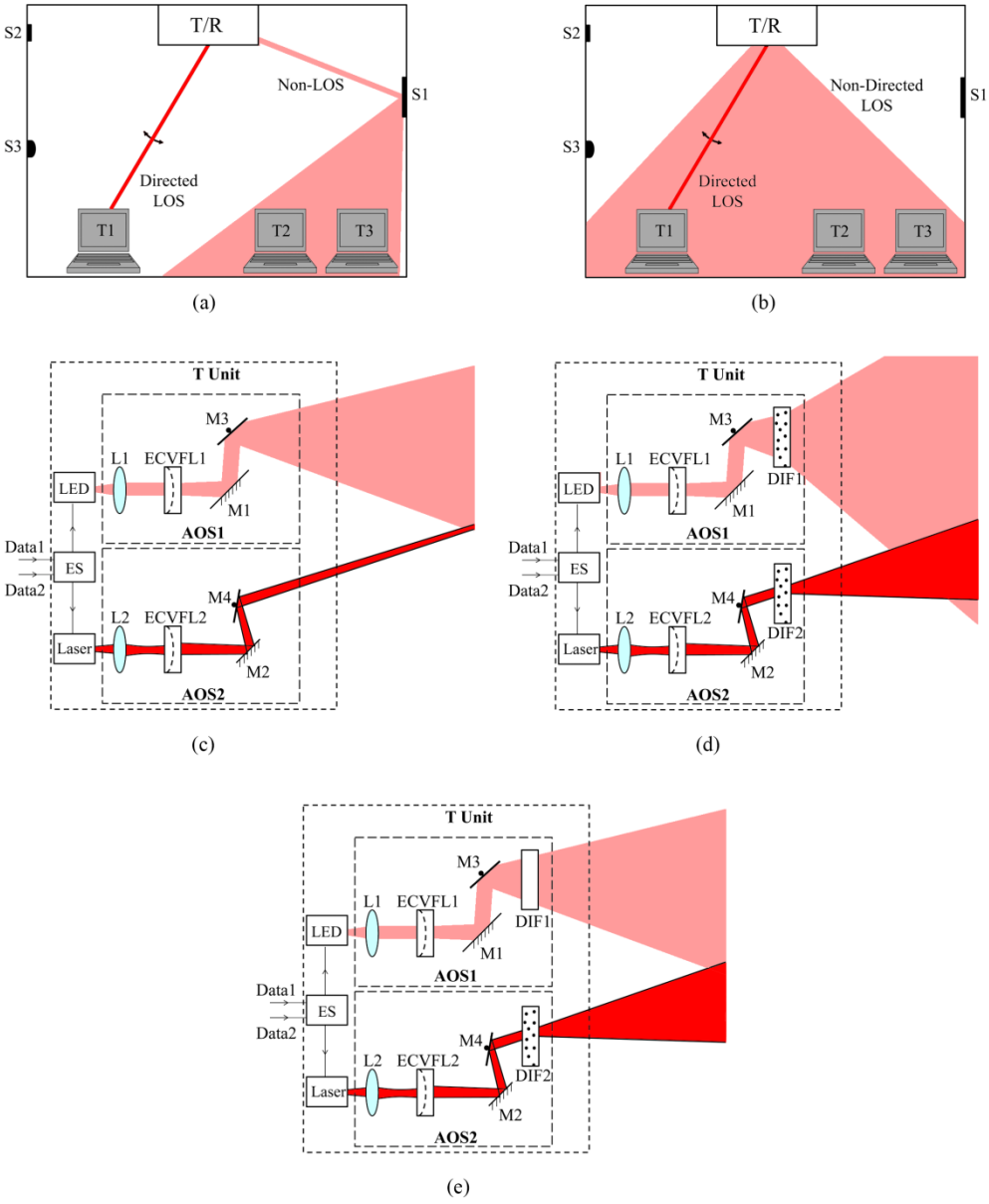

Fig. 6.1. Shown is the proposed smart multi-mode indoor optical wireless approach. Wireless operations are shown using (a) non-LOS diffuse mode and directed LOS mode and (b) directed LOS mode and non-directed LOS mode. (c) A dual-mode transmitter design is shown using a laser, LED, ECVFLs and scan mirrors. (d) and (e) show advanced dual-mode transmitter designs using electronic diffusers. In (d), both electronic diffusers are on and diffuse the light while in (e) only DIF2 is on and diffusing light.

Fig. 6.1 shows the proposed smart multiple modes optical wireless system design that can operate in two modes simultaneously or switch between modes depending upon application requirements and/or changes in the environment. Fig. 6.1(a) shows the optical transmitter on the roof of the room operating simultaneously using a diffuse non-LOS mode and a LOS mode. A diffuse non-LOS mode can be created with a LOS beam striking an optical scattering element S1 so that light spreads in a particular area of the room. Other scatterers or optical antennas (e.g., S2 and S3) can be placed in the room (and adjacent LOS zones) to have a variety of coverage areas of the non-LOS mode. In effect, less optical power is wasted as only the areas requiring wireless connections are covered via the chosen scattering/optical antenna. In Fig. 6.1(a), the diffuse non-LOS link is used to create a non-blocking optical wireless network that can serve multiple stationary users or a moving terminal while the directed LOS link configures itself to establish a high speed link with a stationary terminal that requires additional bandwidth. Simultaneous operation of the mentioned wireless modes can be activated to enable user search or during handover while switching between the LOS and non-LOS modes. An example of the switched mode operation is to smartly switch from the directed LOS mode to diffuse non-LOS mode when physical LOS path blocking occurs. This action keeps communications active and once a LOS path again becomes

available to reconnect communications via the high speed LOS link. The proposed design can also switch between modes for changes in application, such as switching from one user T1 to multiple users T2 and T3 or vice-versa. Thus the proposed design in Fig. 6.1(a) takes advantage of the benefits of LOS and non-LOS diffuse methods since it is able to achieve both the high data rates and the robustness to physical blocking.

Fig. 6.1(b) shows an optical transmitter that is operating in two different LOS modes. Here the non-directed LOS mode (i.e., wide coverage beam) is used to serve multiple user terminals T2 and T3 while the directed LOS mode (i.e., pencil beam) link configures itself to establish a high speed link with the T1 terminal that requires additional bandwidth. Hence, the ability to smartly adapt is achieved giving an overall higher data rate to the users and/or reducing the amount of transmitted power as a smaller area is being covered by the transmitted light.

Fig. 6.1(c) shows the design of a smart zero propagation loss directed LOS optical wireless transmitter [51], [133], [134], [136] combined with a non-directed LOS transmitter. A 2x2 electrical switch ES routes the two possible electrical signals Data 1 and Data 2 to the respective transmitter. Both transmitters contain Agile Optical Systems (AOS) which form their respective light beams. Specifically, the smart directed

LOS link is designed to capture as many photons as were transmitted by the laser beam to produce a lossless transmission channel for communications and minimizing the link gain margin due to laser beam propagation [51], [133], [134], [136]. AOS2 performs 3-D beamforming using a bias lens L2 and ECVFL2 to adapt to changes in link length while mirror M2 is used to direct the light to mirror M4 which is used for scanning in the xy plane. An example experimental implementation of a mechanical tracking system using a rotating mirror was demonstrated to have a BER $<10^{-9}$ for 1 Gbit/s [137]. The beam analysis for the smart directed LOS transmitter has been previously analyzed in detail [51].

In Fig. 6.1(c), AOS1 is used to change the divergence of the LED source so that there can be control over the tradeoff between coverage area and irradiance using ECVFL2 and the scatterers (e.g., S1, S2, S3). As scatterers/optical antennas can be of different sizes, shapes, scattering properties and distances from the transmitter, the ECVFL can also provide the optimal beam size illuminating the optical scatter/antenna for desired illumination of the selected zone. Mirror M1 is used to direct the light to the xy scanning mirror M3 that directs the light to a chosen scatterer (e.g., S1) to make a non-LOS diffuse mode as shown in Fig. 6.1(a) or make a LOS link as shown in Fig. 6.1(b). M3 can also be swept

across the room for search operations or to keep link connections to mobile targets moving too quickly for the directed LOS link.

Fig. 6.1(d) and Fig. 6.1(e) shows novel transmitter designs where electronically controlled optical diffuser devices DIF1 and DIF2 are used within the AOS. In Fig. 6.1(d) both DIF1 and DIF2 are activated and cause both beams to spread over a wider area. Fig. 6.1(e) shows DIF2 activated and DIF1 turned off. In Fig. 6.1(e) only the directed LOS beam is diffused and the other beam passes through the diffuser unmodified. Similarly, DIF1 can be activated and DIF2 turned off. An example of an electronic optical diffuser is a liquid crystal (LC) diffuser similar to those used in privacy walls. AOSs can use any combination of agile optical elements, (e.g., liquid lens, spatial light modulators, LC lens, deformable mirrors) and/or fixed optical elements (e.g., diffusers, scattering surfaces, lenses, mirrors, lenslet arrays, mirror arrays) for 3-D beamforming as long as they meet the specifications of the desired wireless application. An example AOS can use a deformable mirror as the ECVFL and the xy mirror so that a single reflective device performs both the scanning and focusing/defocusing operations.

6.3 Smart Link Beam Propagation Analysis Using Multi-Mode Optical Sources

For the analysis of AOS1 using a non-laser light source, one can use ABCD matrix analysis [56], [131]. In a given cross section along the optical axis (z-axis), a paraxial ray can be characterized by its distance from the optic axis (or its height) h and its ray divergence θ with respect to the optical axis. After traveling through an optical system, the input height and ray divergence are related by [56]:

$$\begin{bmatrix} h_{OUT} \\ \theta_{OUT} \end{bmatrix} = \begin{bmatrix} A & B \\ C & D \end{bmatrix} \begin{bmatrix} h_{IN} \\ \theta_{IN} \end{bmatrix}, \tag{6.1}$$

where A, B, C, and D are the elements of the ABCD matrix (ray transfer matrix) which characterize the system. The ABCD matrix of the system can be obtained by multiplying together the matrices for the optical elements comprising the system.

An example ABCD matrix for AOS 1 using the design of Fig. 6.1(c) with the method of Fig. 6.1(b) is given by:

$$\begin{bmatrix} A & B \\ D & C \end{bmatrix} = \begin{bmatrix} 1 & d_{L1} \\ 0 & 1 \end{bmatrix} \begin{bmatrix} 1 & 0 \\ -\frac{1}{f_{L1}} & 1 \end{bmatrix} \begin{bmatrix} 1 & d_{S1} \\ 0 & 1 \end{bmatrix} \begin{bmatrix} 1 & 0 \\ -\frac{1}{F_1} & 1 \end{bmatrix} \begin{bmatrix} 1 & L \\ 0 & 1 \end{bmatrix}, \tag{6.2}$$

where d_{L1} is the distance from the LED source to L1, f_{L1} is the focal length of L1, d_{S1} is the distance from L1 to the ECVFL, F_1 is the focal length of ECVFL1, and L is the distance from the ECVFL1 to the receiver. Note that the ABCD matrix for deflection from a flat mirror is the identity matrix; thus, it is not shown explicitly in equation (6.2) since

it does not change the result. Notice that the AOS1 ABCD matrix is dependent on F_1, providing control over the ray height and ray divergence, thus enabling control over the coverage area. To find the relationship between the ray height, ray divergence, and F_1, substitute the results of equation (6.2) into equation (6.1):

$$\begin{aligned} h_{OUT} &= Ah_{IN} + B\theta_{IN} \\ \theta_{OUT} &= Ch_{IN} + D\theta_{IN} \end{aligned}, \tag{6.3}$$

where

$$\begin{aligned} A &= 1 - \frac{d_{S1}}{F_1} - \frac{d_{L1}}{f_{L1}}\left(1 - \frac{1}{F_1} - \frac{d_{S1}}{F_1}\right) \\ B &= L + d_{S1} + d_{L1} - \frac{L}{F_1}\left(d_{S1} + d_{L1}\right) - \frac{d_{L1}}{f_{L1}}\left(L + d_{S1} - \frac{d_{S1}L}{F_1}\right) \\ C &= -\frac{1}{f_{L1}}\left(1 - \frac{1}{F_1} - \frac{d_{S1}}{F_1}\right) \\ D &= 1 - \frac{L}{F_1} - \frac{1}{f_{L1}}\left(L + d_{S1} - \frac{d_{S1}L}{F_1}\right) \end{aligned}, \tag{6.4}$$

Thus, using equations (6.3) and (6.4), F_1 can be found to achieve the desired divergence and coverage area.

The smart indoor visible wireless LOS link has already been analyzed for single-mode Gaussian beam lasers [51]. This analysis can be extended to multimode laser sources for AOS2 by using the M^2 propagation parameter [56], [57], [58], [59] , [131]. Specifically, ray optics ABCD matrix method [56], [131] can be used to conduct smart link beam propagation analysis when using multi-mode optical sources for the link. The results of this analysis are presented here and details on

derivations of the ABCD matrices are in references [56] and [131]. The relation between the multimode beam radii and M^2 propagation parameter can be written as [60]:

$$W(z) = Mw(z), \tag{6.5}$$

where *w(z)* is the beam radii of the embedded fundamental mode Gaussian beam at a distance *z* from the source. Thus the Rayleigh range is [60]:

$$z_R = \frac{\pi w_0^{\,2}}{\lambda} = \frac{\pi W_0^{\,2}}{M^2 \lambda}. \tag{6.6}$$

where λ is the wavelength of the laser beam, w_0 is the minimum beam radius of the embedded single mode Gaussian beam, and W_0 is the minimum beam radius of the multimode laser beam. Assuming the same input and output media, the beam waist for a single mode Gaussian laser beam at any location in the optical wireless link can be written as [51]:

$$w(z) = \sqrt{\frac{\lambda}{\pi}\frac{\left(Az_R\right)^2 + B^2}{z_R}}, \tag{6.7}$$

where *A* and *B* are the respective elements of the ABCD matrix. The minimum beam waist size can be written as [51]:

$$w_{Min} = \sqrt{\frac{\lambda z_R}{\pi\left[\left(Cz_R\right)^2 + D^2\right]}}, \tag{6.8}$$

where *C* and D are the respective elements of the ABCD matrix. Substitution of equations (6.5) and (6.6) into equations (6.7) and (6.8) leads to:

$$W(z) = M\sqrt{\frac{\lambda}{\pi}\frac{\left(Az_R\right)^2 + B^2}{z_R}}, \tag{6.9}$$

and

$$W_{Min} = M\sqrt{\frac{\lambda}{\pi}\frac{z_R}{\left[\left(Cz_R\right)^2 + D^2\right]}}, \tag{6.10}$$

Using equations (6.9) and (6.10) instead of equations (6.7) and (6.8), the optical link design can be analysed using the method in reference [51]. Following this method, one can compute the design parameters needed to achieve a low propagation loss link for a given maximum link range and maximum BER for an eye safe maximum laser power level.

6.4 Smart LOS Links Using Multi-Mode Sources: An Experimental Demonstration

Spatially multi-mode optical sources such as multi-mode lasers and LEDs are cost effective high reliability light sources that are suited for large scale industrial deployment. Hence, it is important to demonstrate

the operational principles of the ECVFL-based smart LOS link using multi-mode lasers and LEDs. Using the dual-mode link transmitter design shown in Fig. 6.1(c), a proof of concept link is implemented for a visible laser and a visible LED source. The purpose of this chapter is to demonstrate a new indoor optical wireless approach which combines current optical wireless methods into one smart system that takes advantage of the benefits of each method. The focus of the chapter is on improving the optical design of the smart system. There are several well known data modulation methods for lasers and LEDs. Optical wireless links have been demonstrated based on intensity modulation and direct detection using visible lasers (by Vixar) and LEDs producing data rates of 10 Gbps and 500 Mbps [129], respectively. For a particular modulation technique, a certain average transmitted optical power is needed to achieve a given bit-error rate [135]. Using agile optical beamforming to increase the amount of received optical power from the transmitter means that the BER (or SNR) can be improved or the same BER can be achieved with a lower amount of transmitted power. The specific increase in BER is dependent on the data modulation technique chosen. Thus was decided to use only analogue modulation for this demonstration. Do note that ultimately, the maximum bit rate (or data rate) is limited according to Shannon's Law (or the Shannon-Hartley

Theorem). For channels with additive white Gaussian noise, this is given by:

$$\mathrm{BR} = \Delta f \, log_2(1 + \mathrm{SNR}) \tag{6.11}$$

where Δf is the bandwidth in Hertz (Hz) of the channel. The laser deployed is a Global Laser Beta-Tx Laser Diode Module with λ = 670 nm. This laser module has a built in bias lens (L2) and is capable of being modulated at speeds up to 50 MHz. The 650 nm LED source deployed is the transmitter portion of the Firecomms FS-EDLT Evaluation Board Transmit/Receive (T/R) unit [138]. This T/R unit was originally developed for short range (<50 cm) optical wireless communication with a built in bias lens (L1) and data rates < 125 Mbps. It uses a Silicon (Si) PIN photodiode in its receiver that has a responsivity of 0.3 A/W at 660 nm and 0.45 A/W at 850 nm. Typical responsivity curves for Si, Germanium (Ge), and Indium Gallium Arsenide (InGaAs) photo-diodes versus wavelength are found in reference [139]. Note that Ge and InGaAs photo-diodes have much better responsivity than Si in the infrared region so they are used in infrared applications. AOS1 is composed of an ECVFL placed at a distance of 5 cm from the LED module. AOS2 is setup using an ECVFL placed 8 cm from the laser source. No mirrors or diffusers are used in either AOS. The broadband visible light ECVFLs used in the system are Varioptic (France) Arctic Model 320 liquid lenses based on

electrowetting technology [78]. A Firecomms FS-EDLT Evaluation Board receiver is used as the photo-receiver in the experiment. For optical power measurements a Newport 2931-C power meter is used with a 1 cm^2 active area Newport 918 photo-detector. In the smart link demonstration, the laser is modulated at a lower speed than the LED since this specific laser module's bandwidth is lower than that of the LED module used. In practice, laser links can be modulated at higher data rates than LED links.

First, the directed LOS transmitter and non-directed LOS transmitter operating in separate switchable states is demonstrated. The photo-detected RF signals are presented to visually show the improvement in signal quality that the smart link using the ECVFL provides over the non-smart link. Fig. 6.2 shows the performance of a non-smart link and the smart LOS laser link for a photo-detected signal at 50 MHz. As expected, Fig. 6.2(a) shows good performance for both the smart and non-smart link at a short range of 0.2 m. Now note in Fig. 6.2(b) that as the link range reaches 1.5 m, the non-smart link performance degrades drastically while the smart LOS laser link continues to provide a good signal. In effect, the use of the smart link extends the LOS link range by a factor of 1.7, since the non-smart link only worked up to 0.88 m. Longer link ranges can be achieved if a different bias lens or lens combination is used [51].

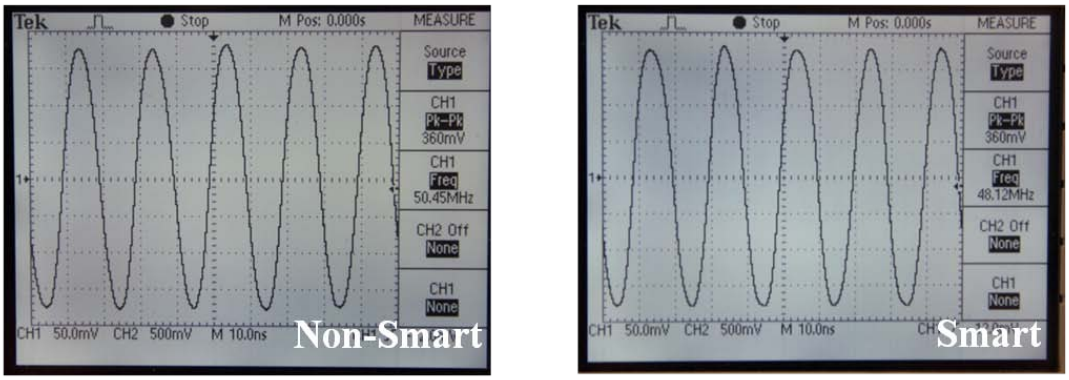

(a)

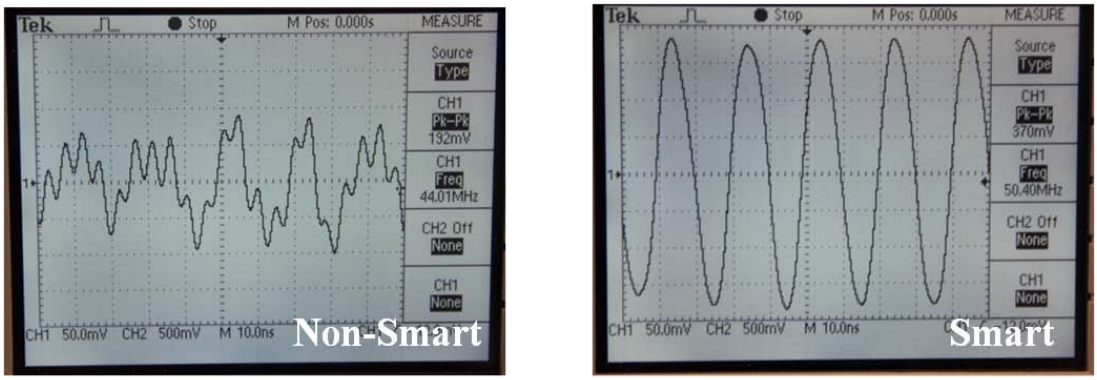

(b)

Fig. 6.2. The photo-detected 50 MHz signals of the non-smart 670 nm multi-mode laser-based and smart directed LOS link at a distance of (a) 0.2 m and (b) 1.5 m.

Fig. 6.3 shows the photo-detected signal for the non-smart and smart LOS LED link operating at 100 MHz. Here again the objective is to get the maximum amount of power achievable using the smart LED link. Fig. 6.3(a) shows good performance for the non-smart link at a short link range of 0.3 m. As shown in Fig. 6.3(b), the smart LED link continues to provide a good signal with link range of 1.1m, a factor of 2 improvement in link range versus the non-smart link which only worked till 0.55 m.

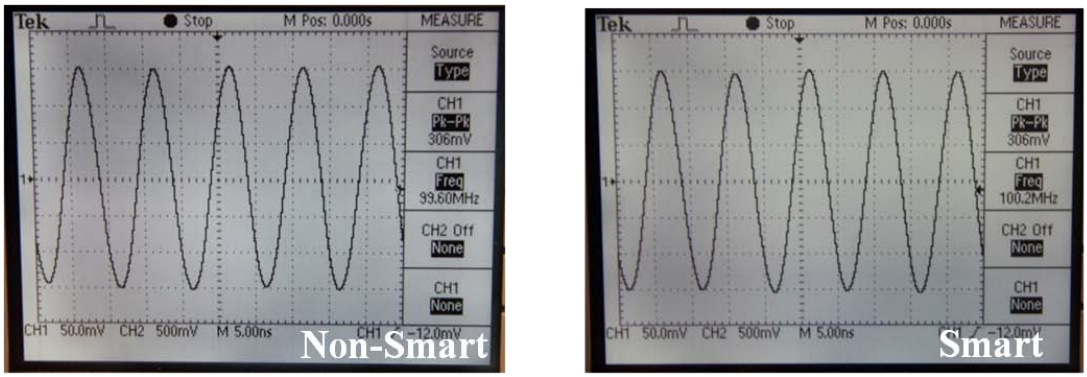

(a)

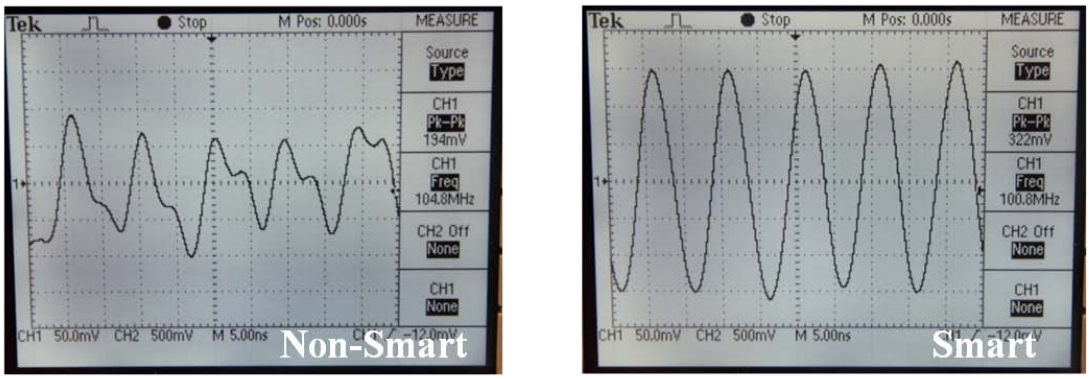

(b)

Fig. 6.3. The photo-detected 100MHz signals of the non-smart 650 nm multi-mode LED and smart non-directed LOS link at a distance of (a) 0.3 m and (b) 1.1 m.

Fig. 6.4 shows the improvement achieved in received optical power at varying distances for the smart link versus the non-smart link using the multi-mode sources. Specifically, Fig. 6.4(a) shows a 1.7X improvement (at 1.3 m) in received optical power for the smart laser link versus the non-smart laser link. Similarly, Fig. 6.4(b) shows a 2.16X improvement (at 1.3m) in received optical power for the smart LED link versus the non-smart LED link.

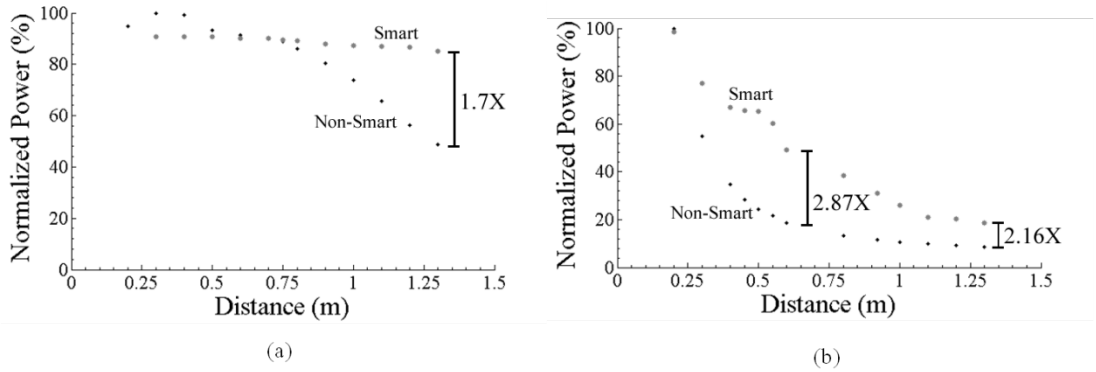

Fig. 6.4. The received optical power detected for the data modulated signals for the non-smart and smart wireless links using a (a) 670 nm multimode laser link and a (b) 650 nm multi-mode LED.

Fig. 6.5 shows simultaneous operation of the directed LOS laser link and the non-directed LOS LED link. Another feature of the Fig. 6.1 transmitters is that ECVFLs can be used to control the amount of RF power generated by the photo-receivers and thus operate with optimal photo-detection power levels for best signal-to-noise (SNR) ratios. Moreover, fine control of optical irradiance at a given range achieved via the ECVFL along with data signal coding methods can reduce the chances for eavesdropping by an unauthorised user. To demonstrate this variable optical attenuation/irradiance control operation, Fig. 6.5(a) and Fig. 6.5(b) shows a 2.7 dB difference in the received RF power levels at a range of 1 m for the non-directed LOS LED link for two different drive settings of the ECVFL.

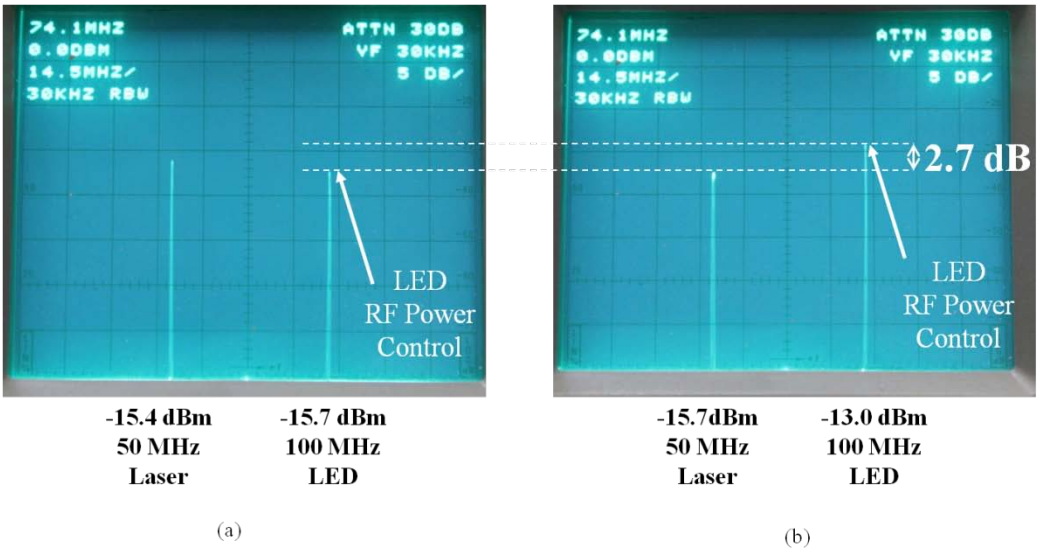

Fig. 6.5. Simultaneous LOS laser and LOS LED link operation demonstrating the use of agile beamforming to control the amount of optical irradiance and hence RF signal produced at a link distance of 1 m. The RF power control shown is for a change of 2.7 dB.

As mentioned, the ECVFL can also be used to provide beam coverage area and irradiance (Watts/m^2) control in the receiver zones. Fig. 6.6 shows LED light beam coverage area control via ECVFL at a link distance of (a) 0.9 m and (b) 2.5 m. Experiments indicate that despite the non-single spatial mode of the LED, the ECVFL is able to produce controllable size beam spots needed to form the smart link. Note that for zero loss smart link operations, the ECVFL should be configured to realize the smallest beam area (or achieve the highest irradiance) possible at the receiver.

Note that for networks with large information capacity that a single proposed transceiver is not able to handle, data transmission can be done

using multiple transmitters, i.e., a transmitter array in conjunction with agile optic lens array, instead of single elements within the transceiver.

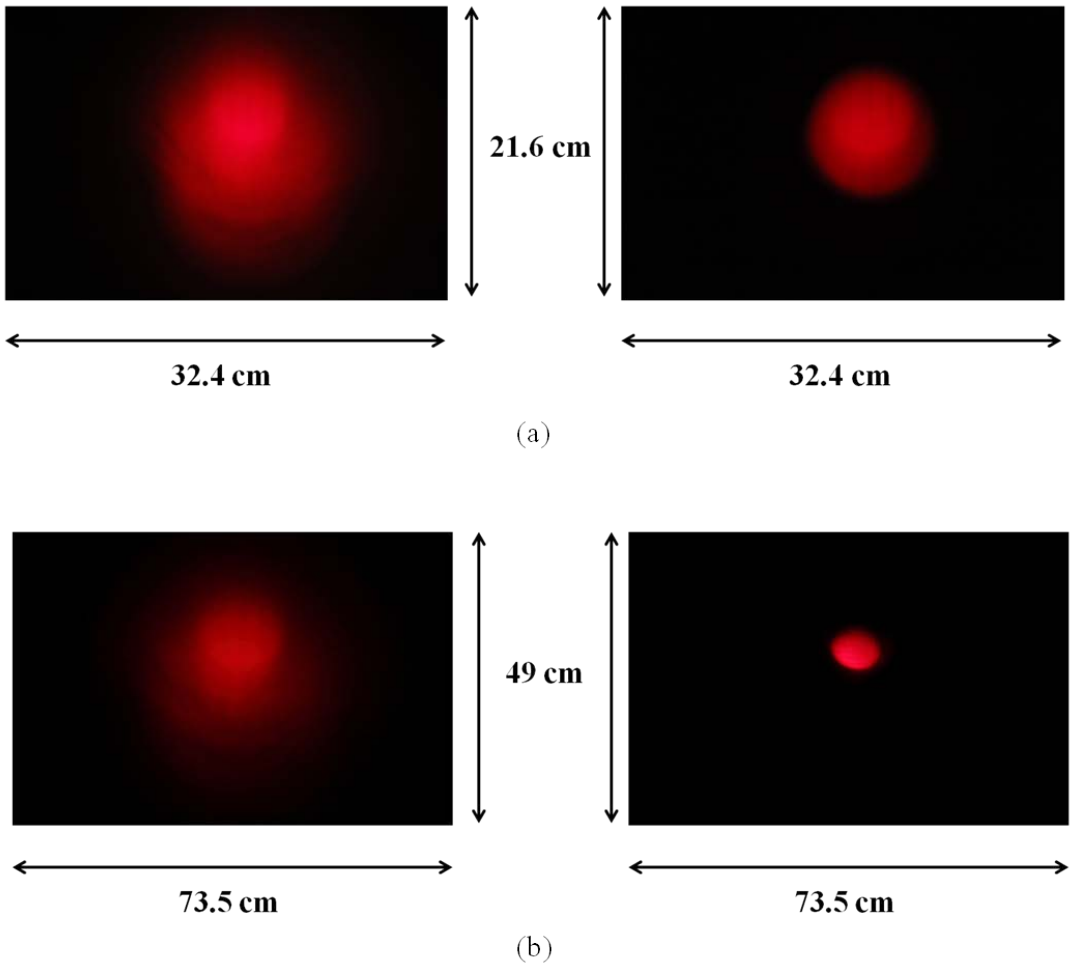

Fig. 6.6. Multi-mode 650 nm LED light beam coverage area control via ECVFL at a link distance of (a) 0.9 m and (b) 2.5 m.

6.5 Conclusion

In conclusion, presented is the design of a smart multiple modes indoor optical wireless system that combines line-of-sight (LOS) and non-LOS optical wireless methods to smartly adapt to changes in environment and application. The proposed design is able to operate in three optical wireless modes called directed LOS, non-directed LOS, and diffuse non-

LOS. These modes smartly accommodate for changes in the number of users/user mobility and optimal coverage area, along with providing an increasing robustness to receive light blocking. By choosing the optimal coverage area and optimizing the transmitted power, the optical wireless system is made energy efficient. Experiments conducted demonstrate for the first time that economical high reliability multi-mode visible light sources such as lasers and LEDs indeed have the spatial properties to implement proposed 3-D beamforming required for energy efficient smart optical wireless LOS links. Applications for the smart multiple mode wireless system includes mobile computing, medical monitoring, data centre computer communications, and wireless sensor networks.

http://dx.doi.org/10.1117/1.OE.52.5.055001

CHAPTER 7

BROADBAND FREE-SPACE OPTICAL AND FIBER-OPTIC SWITCHES USING ELECTRICALLY CONTROLLED LIQUID LENSES

7.1 Introduction

Small port 2 x 2 type optical switching modules are extensively used in laser-based systems including optical communication systems and test and measurement instrumentation. A variety of 2 x 2 free-space optical switching technologies with a wide range of switch performance numbers in terms of switching speed, polarization dependence, crosstalk, loss, and cost have been demonstrated. Some of these free-space switch technologies include nematic [9], [141] and ferroelectric liquid crystals [142], bulk Cadmium Telluride electro-optic crystals [143], ferroelectric photorefractive crystals [144], silicon elastomer optofluidics [145], acousto-optics [146], exciton absorption reflection switch arrays [147], electroholography [148], and Micro-Electro-Mechanical-Systems (MEMS) [149]. Today, MEMS switches have indeed shown excellent overall performance specifications given their simplicity in broadband optical designs and maturity of MEMS device fabrication. Recently, another micro-device technology suitable for broadband light called liquid lenses has had commercial success via use in miniature cameras

and cell phones [150], [151]. The robustness of these electronically controlled liquid lenses has inspired their recent use in fiber-optic attenuation [152], [153]. In this letter, these electro-wetting technology liquid lenses are shown to realize and demonstrate a 2 x 2 freespace optical switch with a simple two optical component design that can provide features such as low power consumption, broadband operation, and moderate loss, crosstalk, and isolation values. Fiber coupled versions are also possible as shown by a basic 1 x 2 switch design and test. Given the promise and mature development of electro-wetting liquid lens device technology, the proposed switch could find applications in test instrumentation systems as well as fiber-coupled modules. Do note that as early as 1982, electro-wetting device technology has been used in optical switching such as to form a 1 x 2 multi-mode fiber switch where the fluidic motion of a mercury slug acting as a mirror encased in a capillary tube fluidic device forms the active switch control [154]. In the present chapter, the focus is to show how any ECVFL technology such as today's commercialized electro-wetting device technology can be used to realize 2 x 2 and 1 x 2 switches.

7.2 Proposed Switch Designs

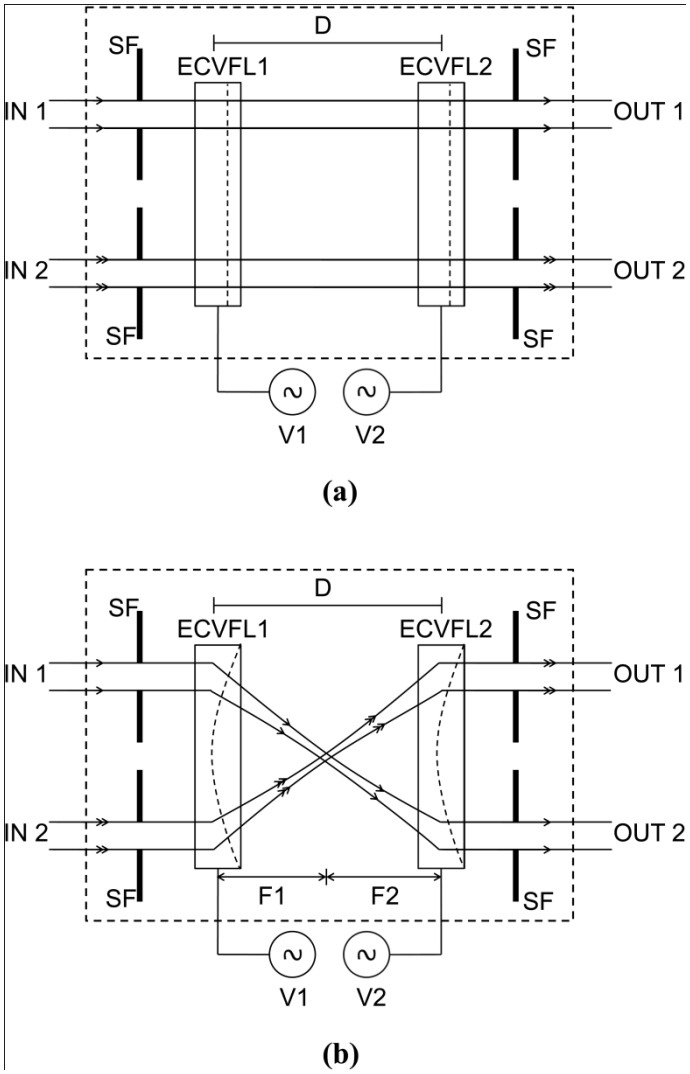

Fig. 7.1. The top view of the proposed liquid lens-based 2 x 2 free-space optical switch design. (a) Straight state and (b) crossed state of switch.

Fig. 7.1 shows the proposed 2 x 2 free-space optical switch design that engages programmable image inversion optics [52]. The input laser beams are aligned so that they run parallel to each other and are positioned symmetrically about the center positions of the two liquid lenses, ECVFL1 and ECVFL2, separated by a distance D. Iris Spatial Filters (SF) are used to form the same size input and output beam ports

for the switch. The SFs also act to remove unwanted optical noise in the switch. If the input beams are highly collimated and spatially clean, one does not require the use of the SFs. For example, SFs can be removed if light is fed by optical fibers. V1 and V2 are the voltage control for ECVFL1 and ECVFL2, respectively. This voltage control can produce straight beam passes (no input image inversion) with no liquid lensing to produce the straightpath state of the 2 x 2 switch, as shown in Fig. 7.1(a). On the contrary in Fig. 7.1(b), V1 and V2 voltage control of the liquid lenses can produce beam deflections that result in the 2 x 2 crossed beam switching state or image inversion for the input image. In addition, with appropriate liquid lens voltage control, one can also produce an analog-mode attenuation of the input light beams. Furthermore, if the output beam ports are placed right next to each other, one can also realize a 1 x 2 variable tap coupler operation.

Fig. 7.1(b) shows that the ECVFL1 and ECVFL2 focal lengths are adjusted to F1 and F2, respectively. Thus, the input beams can be magnified or de-magnified by this F1/F2 liquid lens-based imaging system. If no input beam spatial modification is desired, which is typical for 2 x 2 switching operations, then F1 should be equal to F2 for the switch crossed state. Note that the proposed design uses minimal components in an in-line geometry for ease of assembly. Also note that although the Fig. 7.1 design is shown for free-space input and output

ports, one can use fiber-fed light into the same switching structure to form a 2 x 2 fiber-optic switch. The size of the switch can be minimized using short D values and ECVFLs with focal lengths as short as 0.5D. Do note that the proposed 2 x 2 switching design shown in the Fig. 7.1 dashed-line box operates in a classic switch mode and not as a light deflection module; in which case input–output light beams do not maintain collinear aligned paths.

7.3 Proposed Switch Demonstrations

To demonstrate the concept of proposed switch, the Fig. 7.1 design is set-up in the laboratory with D = 14 cm. Two 30mW 633- nm He–Ne lasers are collimated and used as switch input beams with a lateral separation of 2.09 mm. Manual rotation style optical attenuators are used to equalize the power levels of the two input beams. Arctic Model 320 liquid lenses by Varioptic are used for the experiment with specified 400–700 nm broadband wavelength operation. Fig. 7.2 shows the two different operational states of the switch for (a) Input 1 port fed by the laser and Input port 2 not fed by the laser beam and (b) Input port 2 fed by the laser and Input port 1 not fed by the laser beam. This process of data acquisition using a single input beam at a time is implemented to accurately measure contributions of the given input optical power to the two output ports. The Fig. 7.2 switch output plane photograph taken by a

CCD camera shows in the photos on the left the switch straight state and the right photos the crossed switch state. For the straight switch state V1 = 41.3 V and V2 = 41.7 V while for the crossed switch state, V1 = 51.3 V and V2 = 53.8 V. The slight difference in voltages indicates that no two liquid lenses are identical and furthermore, analog voltage control of the lenses allows for correction of possible alignment errors in the 2 x 2 switch structure. A free-space optical detector is used at the OUT 1 and OUT 2 port locations for measuring the optical beam powers. The Varioptic lens radius of curvature varies from 32.10 mm at 41 V to 5.62 mm at 54 V.

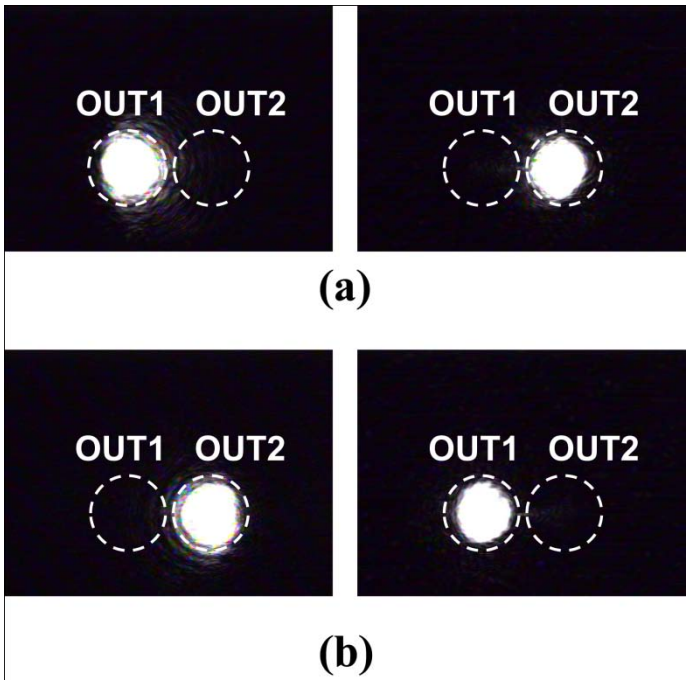

Fig. 7.2. Shown are the switch output port camera views of the two different states of demonstrated Fig. 7.1 2 x 2 switch. The left photos show the straight switch state and the right photos show the crossed switch state. (a) Demonstrates the switch operation with Input 1 on and Input 2 off and (b) with Input 2 on and Input 1 off.

Table 7-I. 2x2 Free-Space Switch Measured Results

	Operating Channel	Crosstalk (dB)	Within Channel Isolation (dB)	Loss (dB)
Straight Switch State	IN1 → OUT1	27.6	24.1	1.1
	IN2 → OUT2	26.3	23.0	1.0
Crossed Switch State	IN2 → OUT1	28.5	23.0	1.1
	IN1 → OUT2	27.7	24.2	1.0

Table 7-I gives the experimentally measured switch crosstalk, within-channel isolation, and port-to-port loss. Switch crosstalk in dB is defined as 10 log [Optical Signal Power in Desired OutputPort/Optical Power in the Other Output Port]. Within-channel isolation in dB is defined as 10 log [Optical Signal Power in DesiredOutput Port/Optical Power in the Same Output Port but coming from the Other Input Port]. Rotation of a Half-Wave Plate (HWP) in the input beam path is used to determine PDL. PDL in dB is defined as 10 log [Maximum Output Power due to rotation of the HWP/Minimum Output Power due to rotation of the HWP]. The PDL is measured to be <0.2 dB. The worst case values for the switch loss, crosstalk and within-channel isolations are 1.1 dB, 26.3 dB and 23.0 dB, respectively. Each ECVFL contributes a 0.5 dB loss to the switch loss. The experiment was next repeated with a 514-nm laser giving a lower optical loss of 0.9 dB, a 25.1 dB average within-channel isolation, and a 25.9 dB average crosstalk. Note that these crosstalk and within-channel isolation levels can be improved by using smaller input beam sizes or larger aperture ECVFL devices to produce larger output

beam separations. The switching speed of the optical switch is <100 ms given by the present electro-wetting technology Arctic liquid lens response time. Do note that recently, sub-milliseconds switching speed [155] has been demonstrated for communication application electro-wetting devices; thus speed improvements for ECVFL devices can be expected with improved device designs, materials, and electric drive conditions. The null-to-null input beam diameters for the 633 nm and 514 nm laser beams are 1.58 mm and 1.52 mm, respectively.

To test the switch design with applicability to infrared telecommunication bands (e.g., 1500–1600 nm) Single Mode Fiber (SMF) feeds, a 1 x 2 fiber-optic switching module was tested using standard 1550 nm center wavelength SMFs with coupled fiber Graded Index (GRIN) lenses for beam collimation [156]. The GRIN lens is a standard telecom C-band 1550 nm center band device with a 1.8 mm diameter and 9 mm length producing a null-to-null IR beam of 1.38 mm diameter. The 1 x 2 switch design uses a single ECVFL is shown in Fig. 7.3. Fig. 7.3(a) shows the 1 x 2 switch operation when the coupling between the input port SMF and OUT 1 requires no lensing. In the 1 x 2 switch state shown in Fig. 7.3(b), the voltage of the ECVFL is adjusted to deflect the beam to couple into output port 2. This 1 x 2 switch was measured to have a within-channel SNR of 32.87 dB. The switch bandwidth was measured using an Optical Spectrum Analyzer (OSA)

with a built-in wideband infrared source. First the output source of the OSA was connected to the input of the OSA to characterize the power spectrum of the source in dBm. Then the OSA output source was connected to the 1 x 2 switch input and the OSA was used to measure the output of the switch. This measurement and the source power spectrum were subtracted to give the broadband spectral response of the switch. The 3 dB bandwidth was then measured using the 1550 nm wavelength as the central reference and found to be from 1469.13 nm to 1644.8 nm. The measured optical insertion loss was 8 dB for the 1 x 2 switch. This number is presently high due to the large (>6.5 dB) optical losses produced by the ECVFL at the test infrared (IR) wavelengths using a direct light transmission test through the Varioptic lens device. Note that the deployed ECVFLs are designed for visible light and have a visible band antireflection coating, and indeed can give low loss performances as demonstrated for the 2 x 2 free-space switch using visible band lasers. Thus, custom ECVFLs need to be designed for the IR band to achieve a low loss performance for the proposed ECVFL-based switch designs. In addition, the fiber lenses can be optimized to minimize free-space to SMF coupling losses [49], [157].

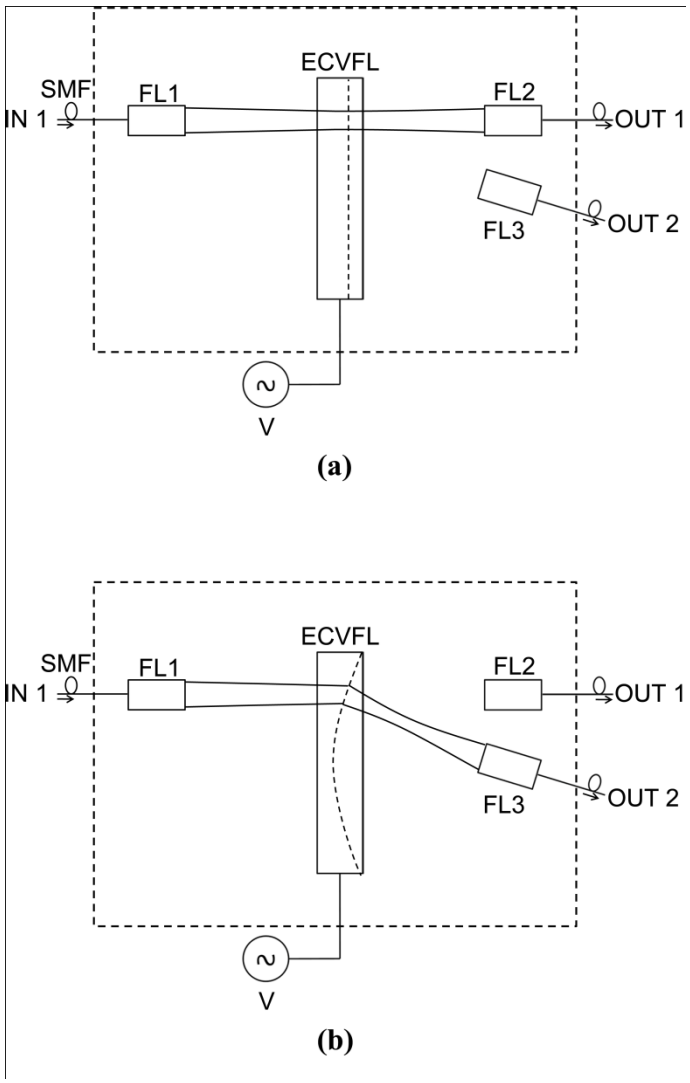

Fig. 7.3. The top view of the proposed liquid lens-based 1 x 2 fiber-optic switch design. (a) Straight state and (b) crossed state of switch.

7.4 Conclusion

First proposed is the design of a novel broadband 2 x 2 freespace optical switch using ECVFLs based on electro-wetting liquid lens technology. This electrically controlled switch is demonstrated showing 26.3 dB crosstalk, 23 dB within-channel isolation, and 1.1 dB optical loss. The deployed ECVFL devices can operate over broad visible wavelengths giving the switch its broad 400 nm to 700 nm range. The switch also

functions as an attenuator via the analog-mode operation of the ECVFL. Also presented and tested is a fiber-optic infrared version of a 1 x 2 switch, proving the operation principles are valid for SMFs. This 1 x 2 switch can find applications in laser-based systems as well as fiber-based test and measurement systems.

http://dx.doi.org/10.1016/j.optcom.2009.12.058

CHAPTER 8

SMART TWO DIMENSIONAL LASER-BASED DISPLAYS

8.1 Introduction

Optical displays are omnipresent in the fields of entertainment, business, military, medicine, and consumer electronics. Today, the dominant display technologies include Liquid Crystal Displays (LCDs) [158] and Digital Micromirror Device (DMD) displays [159], [160]. Another kind of display is the Laser Scanning Display (LSD) [161], [162], [163], [164], [165], [166], [167] that is commonly used in laser shows and more recently has been proposed as portable projection displays. Fundamentally, a LSD is formed when a laser beam (or three in-line laser beams, one for red, one for green, and one for the blue color) is scanned in 2-D space by scanning optics (e.g., mirrors) so that the human eye on temporal integration indirectly sees a 2-D image on the projection screen or directly on the human retina. Each laser is independently temporally modulated in order to produce color and gray-scale in the pixelated display. Compared to LCD and DMD based

displays that have a fixed number of hard-wired pixels with the display optical chip, the LSD can provide complete flexibility in screen distance, pixel count, aspect ratio, brightness and color. Nevertheless, a problem with prior-art laser scanning projection displays is that the farther the distance of the screen from the laser scan optics, the poorer the spatial resolution of the image due to the natural diffraction-based spreading of the Gaussian laser beam that forms the individual pixel/spot in the pixelated display.

Ideally, one would like to design a laser scanning projection display that does not have a drastic reduction in display spatial resolution as the distance of display screen from laser optics increases. In addition, for any given screen distance, one would like to produce a display with an increased pixel count without sacrificing the pixel size. To the best of the authors' knowledge, in this chapter, for the first time is proposed is a smart laser scanning-based display that reduces the limitations associated with the conventional laser scanning display approach. This chapter describes the optical design of the LSD and implements a proof-of-principle experiment demonstrating the basics of the display operations.

8.2 Proposed Smart 2-D Laser-Based Display

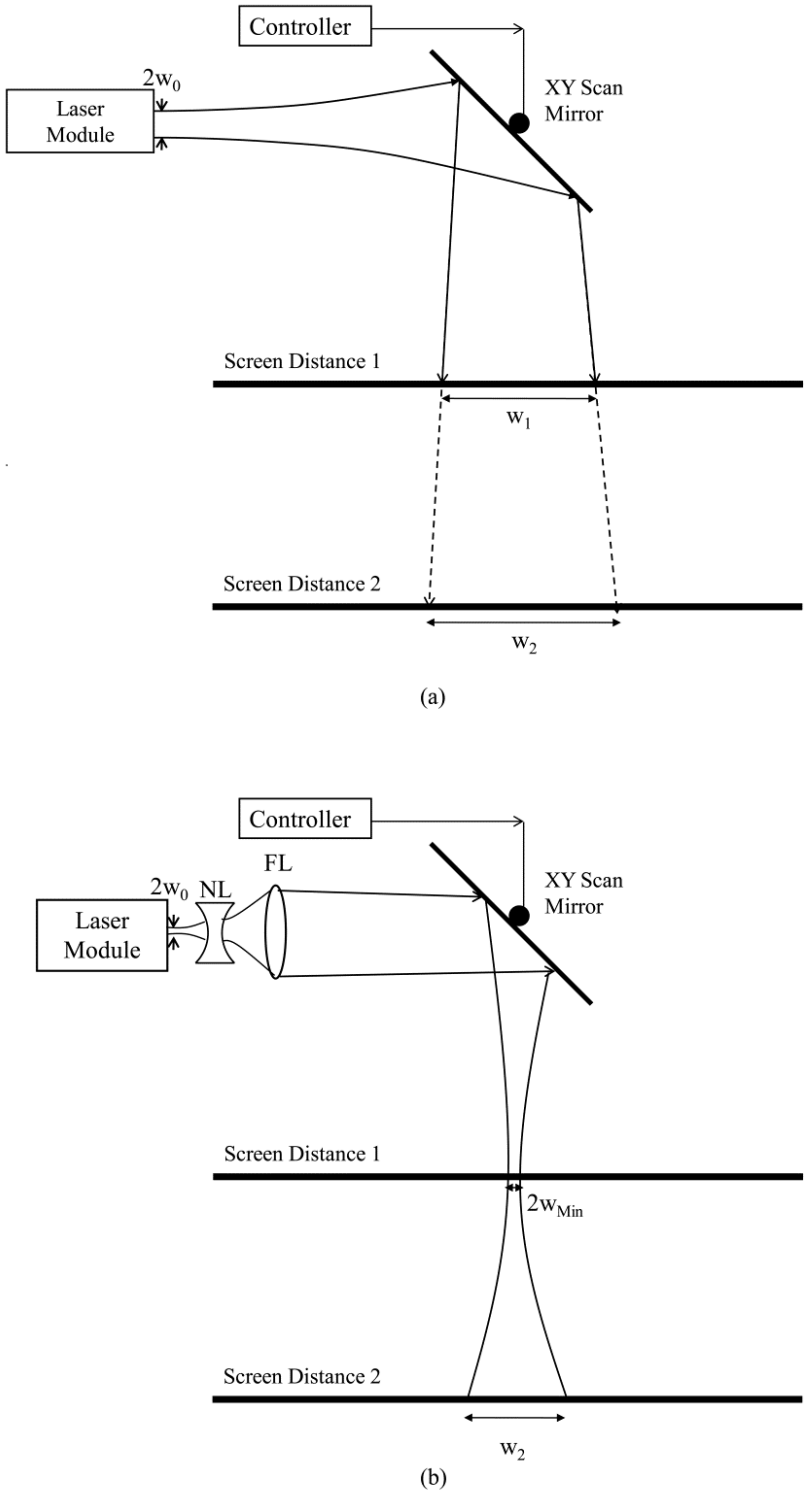

Fig. 8.1. Shown are conventional laser scanning display designs using (a) an unconditioned laser beam and (b) a conditioned laser beam using fixed lenses for optimal high resolution operation at screen distance 1.

Fig. 8.1(a) shows the conventional laser scanning 2-D display design where the laser beam spot size increases for increasing distance of screen from laser optics. A single x-y scanning mirror is shown to produce the scanning pixels on the 2-D screen. Note that other kinds of beam scanning optics can be deployed such as separate x and y scan mirrors, acousto-optic scanners, and spinning polygons. Fig. 8.1(b) shows an alternate fixed lens LSD design for a given fixed screen distance where the spot size is the smallest. Typically, this fixed lens optics in the LSD display is a focusing lens that brings the beam to a tight focus on the screen at the designed fixed screen distance [166]. Note that when the screen is moved farther away in both Fig. 8.1 designs, the spot size gets bigger and hence the display resolution suffers making it a non-optimal display.

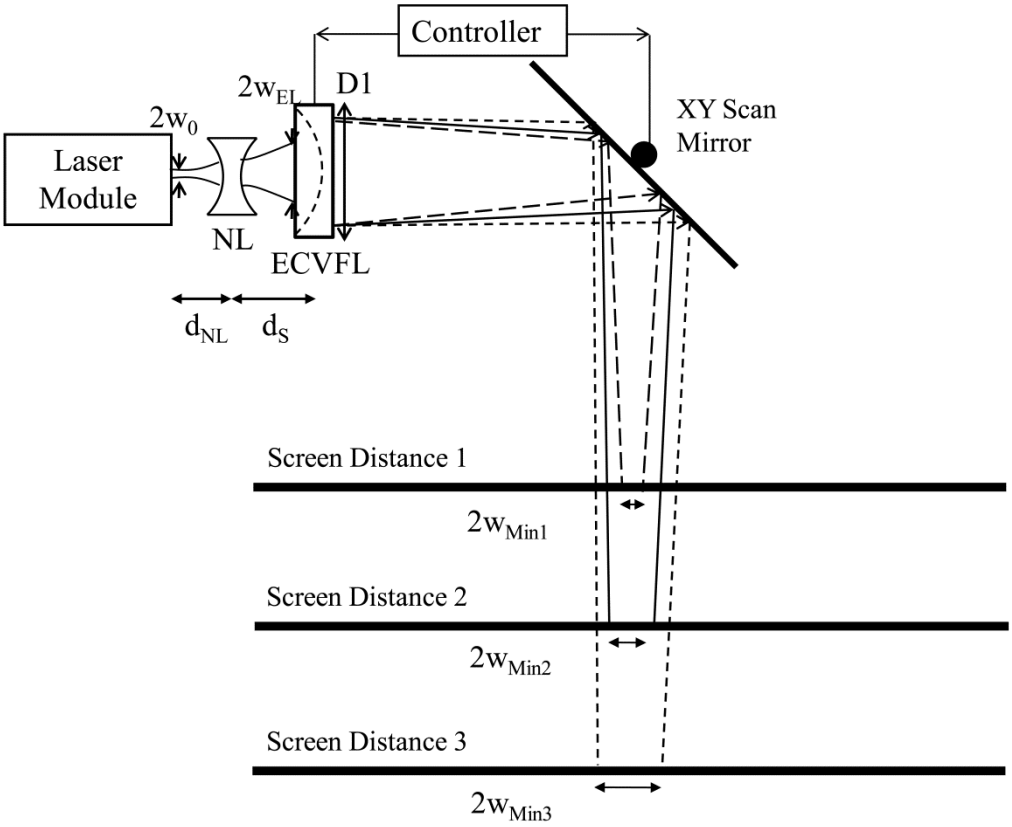

Fig. 8.2. Shown is the proposed smart laser scanning display design using electronically programmable beamforming optics that is able to produce the high resolution beam spots for the entire range of designed screen distances, e.g., from screen distance 1 to screen distance 3.

Fig. 8.2 shows the proposed smart display design where the pixel at the screen forms a minimum beam waist for the given screen distance, thus forming an optimal high resolution LSD [55]. A laser beam (can be a three color beam) with a $1/e^2$ minimum beam radius w_0 emerging from a laser module propagates a distance, d_{NL}, to the Negative Lens (NL) with a f_{NL} focal length that gives the beam a higher divergence.

Next, the beam travels a distance d_s to the ECVFL that has been set for an F focal length. For a given designed display screen distance L from the ECVFL, F is adjusted such that the minimum beam waist

occurs on the display screen. Fig. 8.2 shows the LSD operation for three screen distances, i.e., with minimum beam waists of w_{Min1}, w_{Min2}, and w_{Min3}, respectively. The electronically controlled XY mirror is used for raster scanning the laser beam to create the image on the screen via time integrating of the human eye. D1 is the diameter of the ECVFL and w_{EL} the beam waist hitting the ECVFL. Note that for reader viewing clarity, the beam spots formed on the screens in Fig. 8.1 and Fig. 8.2 are drawn big relative to both the screen size and screen distance L. Also, as a first approximation, it is assumed that L stays the same for the entire scan region of the beam for a given display size and screen distance. A variety of ECVFL technologies such as liquid crystal lenses, liquid lenses, and micro-machined or MEMS-based lenses can be used to form the smart LSD.

To find the appropriate values of F for different lengths, the ABCD matrix method for Gaussian beam propagation is used to give the laser's electric field as [56]:

$$E(r,z) = E_0 \frac{q(0)}{q(z)} e^{-\frac{jkr^2}{2q(z)}}, \tag{8.1}$$

$$\text{where} \quad \frac{1}{q(z)} = \frac{1}{R(z)} - j\frac{\lambda}{\pi w^2(z)}. \tag{8.2}$$

Here $q(z)$ is the complex q-parameter, $k = 2\pi/\lambda$, λ is the wavelength of the light, $r = \sqrt{x^2 + y^2}$, where x and y are Cartesian coordinates in the

plane of the optical field, E_0 is the amplitude of the impinging wave, and z is the distance traveled along the direction of propagation from the minimum beam waist. This analysis is done within the paraxial approximation and must satisfy the relation F #≥ 1.67 [125]. Gaussian beam propagation at another point along the laser beam travel path can be represented by:

$$q_1 = \frac{Aq_0 + B}{Cq_0 + D} \quad , \tag{8.3}$$

where A, B, C, and D are elements of the ABCD matrix for the optical system and q_0 is the initial minimum beam waist q-parameter represented by:

$$q_0 = jz_0 = j\frac{\pi w_0^2}{\lambda}, \tag{8.4}$$

where w_0 is the $1/e^2$ beam waist radius and z_0 is the Rayleigh range, i.e., the distance at which the beam radius is $\sqrt{2}\, w_0$. With reference to Fig. 8.2, the ABCD matrix of the system can be formed as follows:

$$\begin{bmatrix} A & B \\ C & D \end{bmatrix} = \begin{bmatrix} 1 & L \\ 0 & 1 \end{bmatrix} \times \begin{bmatrix} 1 & 0 \\ -\frac{1}{F} & 1 \end{bmatrix} \times \begin{bmatrix} 1 & d_s \\ 0 & 1 \end{bmatrix} \times \begin{bmatrix} 1 & 0 \\ -\frac{1}{f_{NL}} & 1 \end{bmatrix} \times \begin{bmatrix} 1 & d_{NL} \\ 0 & 1 \end{bmatrix} . \quad (8.5)$$

This leads to the elements of the ABCD matrix being:

$$\begin{aligned} A &= 1 - \frac{d_S}{f_{NL}} - \frac{L}{f_{NL}} - \frac{L}{F} + \frac{d_S L}{f_{NL} F} \\ B &= d_{NL} + d_S + L - \frac{d_{NL} d_S}{f_{NL}} - \frac{d_{NL} L}{f_{NL}} \\ &\quad - \frac{d_{NL} L}{F} - \frac{d_S L}{F} + \frac{d_{NL} d_S L}{f_{NL} F} \\ C &= -\frac{1}{f_{NL}} - \frac{1}{F} + \frac{d_S}{f_{NL} F} \\ D &= 1 - \frac{d_{NL}}{f_{NL}} - \frac{d_{NL}}{F} - \frac{d_S}{F} + \frac{d_{NL} d_S}{f_{NL} F} \end{aligned} \quad (8.6)$$

According to equation (8.4), the minimum beam waist q-parameter is purely imaginary. Thus by substituting equation (8.4) into equation (8.3) and setting the real part equal to zero leads to:

$$AC{z_0}^2 + BD = 0 \quad (8.7)$$

Substituting equation (8.6) into equation (8.7) and simplifying with respect to F gives:

$$aF^2 + bF + c = 0, \quad (8.8)$$

where:

$$
\begin{aligned}
a = \Big[& z_0{}^2 \left(L + d_S - f_{NL} \right) + d_{NL}{}^2 \left(d_S + L - f_{NL} \right) \\
& + f_{NL}{}^2 \left(d_{NL} + d_S + L \right) \\
& - 2 d_{NL} f_{NL} \left(d_S + L \right) \Big]
\end{aligned}
$$

$$
\begin{aligned}
b = \Big[& z_0{}^2 \left(2 \left[f_{NL} \left(d_S + L \right) - d_S L \right] - d_S{}^2 - f_{NL}{}^2 \right) \\
& + 2 d_{NL}{}^2 \left(d_S f_{NL} + f_{NL} L - d_S L \right) \\
& - 2 f_{NL}{}^2 \left(d_{NL} d_S + d_{NL} d_{Min} + d_S L \right) \\
& + 4 f_{NL} d_{NL} d_S L + 2 d_{NL} d_S{}^2 f_{NL} \\
& - f_{NL}{}^2 \left(d_{NL}{}^2 + d_S{}^2 \right) - d_{NL}{}^2 d_S{}^2 \Big]
\end{aligned}
$$

$$
\begin{aligned}
c = \Big[& L z_0{}^2 \left(d_S{}^2 + f_{NL}{}^2 - 2 d_S f_{NL} \right) \\
& + 2 d_{NL} d_S L \left(f_{NL}{}^2 - f_{NL} d_{NL} - f_{NL} d_S \right) \\
& + \left(d_{NL} d_S \right)^2 L + f_{NL}{}^2 L \left(d_{NL}{}^2 + d_S{}^2 \right) \Big]
\end{aligned}
\qquad (8.9)
$$

Solving equation (8.8) leads to:

$$
F = \frac{-b \pm \sqrt{b^2 - 4ac}}{2a}
$$

(8.10)

where *a*, *b*, and *c* are given by equation (8.9). For valid solutions, *F* must be positive and real. This condition in-turn gives two valid solutions for *F*. Since the design goal of the smart LSD is to achieve a higher display

resolution, the stronger F is chosen since it makes a smaller minimum beam waist size w_{Min} at L. Using equation (8.4), the minimum beam waist w_{Min} after the ECVFL is represented by:

$$q_{Min} = jz_{Min} = j\frac{z_0}{[Cz_0]^2 + D^2} = j\frac{\pi w_{Min}^2}{\lambda} \tag{8.11}$$

Rearranging Eq. (8.11) leads to the relation:

$$w_{Min} = \sqrt{\frac{\lambda}{\pi}\frac{z_0}{[Cz_0]^2 + D^2}} \quad , \tag{8.12}$$

where C and D are described by equation (8.6). To make sure that ECVFL aperture diameter D1 > $2w_{EL}$, first the ABCD matrix (with elements A_{EL}, B_{EL}, C_{EL}, D_{EL}) from the laser minimum beam waist to the ECVFL must be found. Here w_{EL} is the $1/e^2$ radius of the beam at the ECVFL.

$$\begin{aligned}\begin{bmatrix} A_{EL} & B_{EL} \\ C_{EL} & D_{EL} \end{bmatrix} &= \begin{bmatrix} 1 & d_s \\ 0 & 1 \end{bmatrix} \times \begin{bmatrix} 1 & 0 \\ -\dfrac{1}{f_{NL}} & 1 \end{bmatrix} \times \begin{bmatrix} 1 & d_{NL} \\ 0 & 1 \end{bmatrix} \\ &= \begin{bmatrix} 1 - \dfrac{d_s}{f_{NL}} & d_s + d_{NL} - \dfrac{d_s d_{NL}}{f_{NL}} \\ -\dfrac{1}{f_{NL}} & 1 - \dfrac{d_{NL}}{f_{NL}} \end{bmatrix}\end{aligned} \tag{8.13}$$

By taking the inverse of equation (8.3) and substituting this result into equation (8.2), it is found that:

$$\frac{1}{q_{EL}} = \frac{A_{EL}C_{EL}z_0^{\,2} + B_{EL}D_{EL} - jz_0\left(A_{EL}D_{EL} - B_{EL}C_{EL}\right)}{B_{EL}^{\,2} + \left(z_0 A_{EL}\right)^2} = \frac{1}{R_{EL}(z)} - j\frac{\lambda}{\pi w_{EL}^{\,2}(z)} \tag{8.14}$$

The determinant of equation (8.13) is 1 [56]. Now equating the imaginary parts of (8.14), it is found that $w_{EL}(z)$ is given by:

$$w_{EL}(z) = \sqrt{\frac{\lambda}{\pi}\frac{\left(A_{EL}z_0\right)^2 + B_{EL}^{\,2}}{z_0}}\,. \tag{8.15}$$

To design the LSD system, the system parameters f_{NL}, d_{NL}, w_0 and the maximum L must be chosen. Choice of d_{NL} less than z_0 has not much effect on beam size at ECVFL, hence d_{NL} can be chosen to be small to reduce system size. Using an initial estimate of d_S and the chosen system parameters, one substitutes them into equation (8.9) and then solves equation (8.8) using equation (8.10). If F is imaginary, increase d_S until it reaches its smallest value which gives a positive real value of F.

Consider a smart LSD example with a desired screen distance of 20 cm $\leq$ L $\leq$ 150 cm and f_{NL} = -15 cm and d_{NL} = 16.55 cm. To get an

estimate for d_S , assume that a Gaussian beam is propagating back towards the ECVFL from its w_{Min} location at the maximum L or L_{max} distance. Assuming that $z_{Min} = L_{max}$ is the Rayleigh range for this beam, one can write $w_{EL} = \sqrt{2}\, w_{Min}$ and using equation (8.11) leads to:

$$w_{EL} = \sqrt{\frac{2\lambda L_{max}}{\pi}}\,. \tag{8.16}$$

Now setting equation (8.16) equal to equation (8.15), an initial estimate for d_S is found to be 17.47 cm. Substitution of this estimate into equations (8.9) and (8.10) gives an imaginary root; so the estimate for d_S is increased. A valid value for d_S via this process is found to be 17.49 cm, giving F = 27.92 cm or F = 28.14 cm. Taking the lower value of F of 27.92 cm as explained earlier and substituting it into Eqn (8.15) gives w_{EL} = 0.778 mm. Next, as d_S is known, the value of F for the minimum range can be found using equations (8.9) and (8.10) with $L = L_{min}$= 20 cm to give F = 12.18 cm and F = 30.71 cm. Thus for the given smart LSD example, the ECVFL needs an operation range that satisfies 12.18 cm $\leq F \leq$ 27.92 cm. With these F results, along with the given laser module values of z_0 substituted into equation (8.12), one finds the desired smart LCD pixel size given by w_{Min}. To determine the smart LCD pixel size improvement in comparison to the conventional unconditioned LSD design of Fig. 8.1(a), Gaussian laser beam

propagation through air is assumed giving the $w_{air}(z)$ beam size at the display screen distance of $L1$ by [56]:

$$w_{air}(z) = w_0\sqrt{1+\left(L1/z_0\right)^2}\ . \tag{8.17}$$

where $L1 = L + d_S + d_{NL}$. Thus equations (8.12) and (8.17) give the pixel sizes for the smart LSD and conventional unconditioned LSD, respectively.

The fixed lens LSD design uses the same parameters as the smart LSD design, but with a fixed F value via the FL convex lens instead of a changing F ECVFL. The derivation of *w(z)* is the same as that for equation (8.15). Thus the expression *w(z)* for the Fig. 8.1(b) fixed lens LSD design pixel radii is given as:

$$w(z) = \sqrt{\frac{\lambda}{\pi}\frac{(Az_0)^2 + B^2}{z_0}}\ , \tag{8.18}$$

where A and B are given in equation (8.6).

To compare the improvement in screen pixel diameter, the reduction factor R is defined as:

$$R = \frac{w_{air}}{w_{Min}}\ . \tag{8.19}$$

The pixel number increase factor R^2 of a rectangular image is given by:

$$R^2 = \left(\frac{w_{air}}{w_{Min}} \right)^2 . \tag{8.20}$$

8.3 Experimental Demonstration

For a proof of concept demonstration for the smart LSD, the Fig. 8.2 system is assembled using a Melles Griot Model 05-LHP-991 10 mW He-Ne laser with λ = 632.8 nm and a w_0 = 325 μm. For the ECVFL, an Electrowetting technology-based broadband visible light band variable focus liquid lens, the Varioptic Artic Model 320 with a D1 = 3 mm, is used. The NL has f_{NL} = -15 cm and the separation distances between components are d_{NL} = 16.55 cm and d_S = 17.49 cm. Given these experimental parameters and the LSD design equations in the previous section, one computes a $2w_{EL}$ = 1.56 mm which is less than the condition $2w_{EL}$ < D1. The XY scan mirror is not used in the demonstration as the present focus is LSD pixel size optimization based on screen distance range. The demonstration smart LSD optics is designed for with a maximum L = 150 cm. The ECVFL focal length F is required to range from 12.18 cm to 27.92 cm which is well within the range of the chosen ECVFL which works well from 4.4 cm to 40 cm.

Using the smart and fixed lens LSD design values for w_0, f_{NL}, d_{NL}, d_S and F, Fig. 8.3 shows the theoretical and experimental values for the LSD pixel size representation given as the Gaussian beam waist radius at the different screen positions of L. The Gaussian beam pixel radii of the

conventional unconditioned LSD design is found using equation (8.17). As shown in Fig. 8.3, the beam waist radius expands slowly with increasing screen distance. For the fixed lens LSD design of Fig. 8.1(b) with F = 19.47 cm, the display pixel radii are found using equation (8.18). This design produces a minimum beam waist at L = 51.5 cm that is equal to the smart LSD design beam radius at the same distance. After the L = 51.5 cm screen position, the pixel size expands rapidly with increasing L. Fig. 8.3 indeed shows that the smart LSD design drastically reduces the size of the beam waist over most of the link range when compared to the LSD designs of Fig. 8.1. For example, as shown in

Table **8-I** at L = 20 cm the theoretical beam waist diameters at the screen for the conventional unconditioned LSD design and the smart LSD design are $2w_{air}$ = 933.38 μm and $2w_{Min}$ = 103.83 μm, respectively. These beam waist diameter numbers give a screen pixel diameter reduction factor R of 8.99. Other screen distance examples can be seen in Table **8-I**.

Table 8-I. The Relationship of Factor R and R^2 with Screen Distance L for Design with L_{max} = 150 cm

L (cm)	**$2w_{air}$ (μm)**	**$2w_{Min}$ (μm)**	**R**	**R^2**
20	933.38	103.83	8.99	80.81
100	1784.11	554.42	3.22	10.35
150	2372.06	1076.29	2.2	4.85

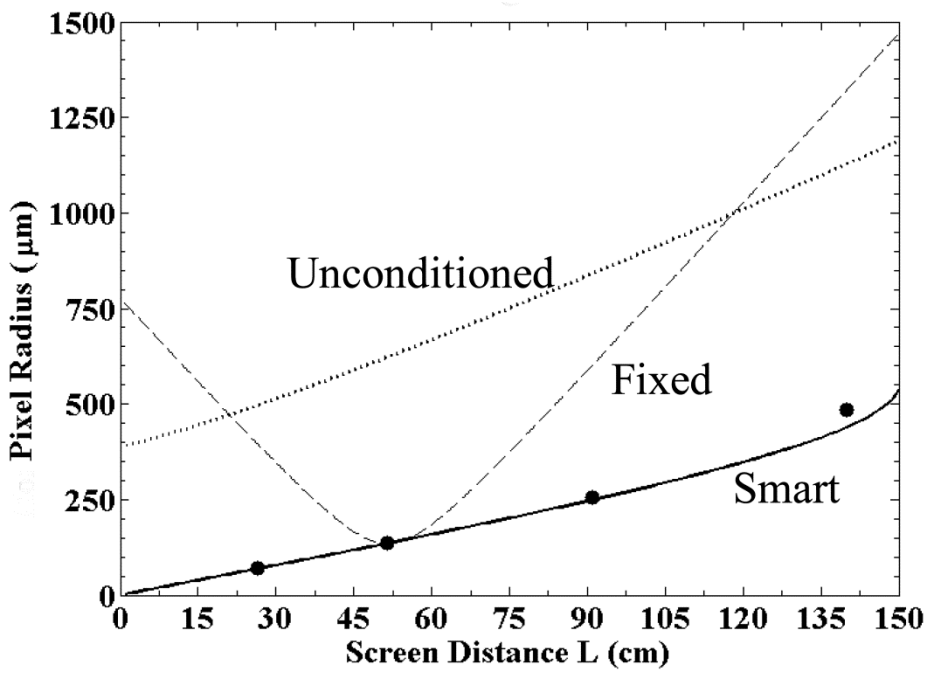

Fig. 8.3. The pixel radius for various screen distances. Plotted are theoretical curves for the unconditioned LSD, the fixed LSD, and the smart LSD. Experimental data for the smart LSD are represented by dots.

Fig. 8.3 also shows that the DMD profiler [70] measured smart LSD beam sizes match up well with the smart LSD design theory. The DMD profiler has the capability to measure the cross-sectional or screen plane vertical and horizontal direction beam sizes; hence Fig. 8.3 shows the beam radii. In theory, the beam spot on the LSD screen is symmetric and hence the horizontal and vertical direction radii are equal. Note that experimentally the beam radii measurements were the same within the tolerance of the measuring device, so only the beam radius for the horizontal direction is shown in Fig. 8.3. A visual representation of the comparative reduction in LSD pixel size using the smart design versus the conventional unconditioned LSD design is shown in Fig. 8.4 for a

link with L = 140 cm. At L = 140 cm, the measured w_{air} and w_{Min} gives R = 2.38 which is a close match to the theoretical result R = 2.56 obtained using equations (8.12), (8.18), and (8.19). Because of the laser beam saturating the CCD imager, the Fig. 8.4 beam photographs were taken using two Neutral Density (ND) filters to reduce light power by 99.99%. Note that the beams are a bit skewed due to the deployed ND filters.

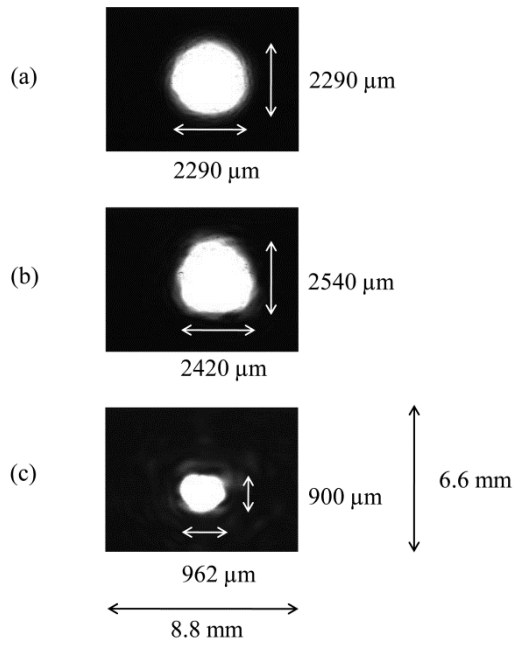

Fig. 8.4. Shown are CCD images taken at L=140 cm for the (a) Conventional unconditioned LSD, (b) Conventional fixed lens LSD using the conditioned laser beam deploying a fixed lens that forms a minimum beam waist at L = 51.5 cm, and (c) proposed smart LSD with the ECVFL programmed for L = 140 cm. The images of the shown laser beams were attenuated using neutral density filters.

When comparing the smart LSD design to the conventional unconditioned LSD design for a fixed screen size, the smart LSD can provide a higher number of pixels in the image. On the other hand when

the pixel count in an image is fixed per video protocol, the smart LSD provides the image within a smaller screen size compared to a conventional LSD-based image. Today, wide-screen televisions have an aspect ratio of 16:9. As an example, assume that there are N = 404,496 pixels or 848 x 477 pixels display with the screen at L = 150 cm. Using the conventional unconditioned LSD design for these image design parameters gives W_x = 2.01 m and W_y = 1.13 m, where W_x and W_y are the horizontal and vertical screen lengths, respectively. With the smart LSD using the W_x = 2.01 m and W_y = 1.13 m screen size, the smaller pixel size at the L=150 cm distance produces an image capacity of N = 1,963,268 or 1868 by 1051 pixels, a pixel number increase factor of R^2=4.85, or a R^2 times improvement in the number of pixels fitting the screen size of the conventional unconditioned LSD image. Other examples indicate for L = 100 cm and L = 20 cm, the values of R^2 are 10.35 and 80.8 times, respectively. Fig. 8.5(a) shows the pixel number increase factor R^2 for the smart LSD compared to the conventional unconditioned LSD of Fig. 8.1(a). Note that the R^2 factor can be increased even further if the designed L_{max} for the smart LSD is greater than the experimentally deployed operational LSD screen range. For example, one can design the smart LSD for L_{max} = 750 cm and operate it with L ranging from 20 cm to 150 cm. For this design, one can choose f_{NL} = -15 cm, d_{NL} = 16.55 cm, λ = 632.8 nm and w_0 = 325 μm. Now

setting equation (8.16) equal to equation (8.15), an initial estimate for d_S is found to be 55.57 cm. Substitution of this d_S estimate into equations (8.9) and (8.10) gives a real root; so the estimate for d_S is decreased until it reaches its smallest value which gives a positive real value of F. The value for d_S via this process is found to be the initial estimate of 55.57 cm giving F = 68.50 cm or F = 47.33 cm. Taking the lower value of F of 47.33 cm as explained earlier and substituting it into Eqn (8.15) gives $2w_{EL}$ = 3476.4 μm. Next, as d_S is known, the value of F for the minimum range is found using equations (8.9) and (8.10) with $L = L_{min}$= 20 cm giving F = 15.50 cm and F = 68.78 cm. Taking the F value that gives the smallest minimum beam waist at each location for the given smart LSD example, the ECVFL needs an operation range that satisfies the condition 15.50 cm$\leq$ $F \leq$ 47.33 cm, component parameters that are achievable using present-day hardware. To see the improvement of using this smart LSD design for the range 20 to 150 cm, R for the different L positions is computed to plot the R^2 versus L plot in Fig. 8.5(b). One can see that R^2 ranges from 65.56 to 803.5, indicating a large improvement in the smart LSD viewing image quality versus a conventional unconditioned LSD. In addition, if one operates this smart LSD up to the maximum design range of L = 750 cm, the improvement in image pixel count is still a very reasonable R^2 = 17.53. Thus by judicious choice of the smart LSD design parameters, the projected image quality

and resolution can be greatly improved over images provided by conventional LSDs.

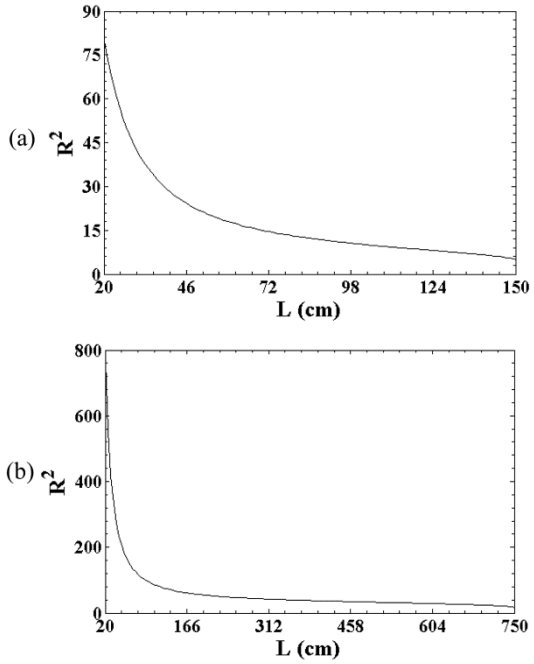

Fig. 8.5. Shown is a design plot for the image pixel count enhancement factor R2 versus display screen distance L with the smart LSD designed for an (a) L_{max} = 150 cm and (b) L_{max} = 750 cm.

8.4 Conclusion

In conclusion, a smart LSD design is proposed that implements high spatial resolution image projection with variable screen distances. The proposed system achieves a high image resolution on the screen by programmable optical beamforming implemented via a cascade of an ECVFL with fixed lenses that in-turn leads to a minimum beam waist (or image pixel size) at the screen location. A proof-of-principle smart LSD optic is designed and demonstrated for a screen distance varying from 20 cm to 150 cm. For example, at a screen distance of 140 cm, the smart LSD shows a 42% pixel size reduction compared to a conventional

unconditioned LSD design. Design analysis shows that the smart LSD can provide a significant enhancement in projected image total pixel count compared to conventional LSD designs. Extension to Three Dimensional (3-D) LSD designs is also possible such as by using infrared laser sources and visible light emission non-linear materials [168]. Another extension is the formation of a compressive laser-scanned display. In this case for a given desired image and fixed screen distance, a minimal number of laser spot beams are scanned in the display screen zone using ECVFL-based spot size and shape control and laser-based optical beam power control [111], [169]. Future work relates to the design of the smart and compressive LSDs incorporating red, blue, and green lasers and required beam scan optics to realize a fully functional color image projection system.

AUTHOR'S PUBLICATION LIST

JOURNAL PUBLICATIONS

1. P. J. Marraccini and N. A. Riza, "Smart Multiple Modes Indoor Optical Wireless Design and Multi-Mode Light Source Smart Energy Efficient Links," *Optical Engineering*, vol. 52, no. 5, May 2013.
   http://dx.doi.org/10.1117/1.OE.52.5.055001

2. N. Riza, P. Marraccini, and C. Baxley, "Data Efficient Digital Micromirror Device-Based Image Edge Detection Sensor using Space-Time Processing," *IEEE Sensors Journal*, Vol. 12, No. 5, pp. 1043-1047, May 2012.
   http://dx.doi.org/10.1109/JSEN.2011.2172410

3. P. J. Marraccini and N. A. Riza, "Power Smart In-door Optical Wireless Link Design," *Jour. Of the European Opt. Society: Rapid Publications*, Vol. 6, Paper 11054, December 2011.
   http://dx.doi.org/10.2971/jeos.2011.11054

4. P. J. Marraccini and N. A. Riza, "Multimode Laser Beam Analyzer Instrument using Electrically Programmable Optics," *AIP Review of Scientific Instruments*, Vol. 82, No. 12, pp. 123107, 2011.
   http://dx.doi.org/10.1063/1.3669535

5. N. A. Riza and P. J. Marraccini, "Smart Two-Dimensional Laser-Based Display," *IEEE Journal of Display Technology*, Vol. 7, No 2, pp. 90-95, February 2011.
   http://dx.doi.org/10.1109/JDT.2010.2093120

6. N. A. Riza, S. A. Reza, and P. J. Marraccini, "Digital Micro-Mirror Device-Based Broadband Optical Image Sensor for Robust Imaging Applications," *Optics Communications*, Vol. 284, No. 1, pp. 103-111, 2011.
   http://dx.doi.org/10.1016/j.optcom.2010.08.078

7. N. A. Riza, S. A. Reza, and P. J. Marraccini, "Electronically Controlled Agile Lens-Based Broadband Variable Photonic Delay Line for Photonic and RF Signal Processing," *Applied Optics*, Vol. 49, No 35, pp. 6718-6725, December 2010. http://dx.doi.org/10.1364/AO.49.006718

8. N. A. Riza and P. J. Marraccini, "Broadband 2 x 2 Free-Space Switch Using Electronically Controlled Liquid Lenses," *Optics Communication*, Vol. 283, No 9, pp. 1711- 1714, May 2010. http://dx.doi.org/10.1016/j.optcom.2009.12.058

CONFERENCES

1. P. J. Marraccini and N. A. Riza, "Dual Mode Indoor Optical Wireless Data Link Design using Micro-Optics for Robust Energy Efficient Operation," *European Optical Society Annual Meeting (EOSAM)*, Aberdeen, October 2012.

2. N. A. Riza and P. J. Marraccini, "Power Smart In-door Optical Wireless Link Applications," *The 8th International Wireless Communications and Mobile Computing Conference (IWCMC)*, Cyprus, 27-31 August 2012.

3. P. J. Marraccini and N. A. Riza, "Reconfigurable Visible Wireless Optical Link for Indoor Applications," *Royal Irish Academy Research Colloquium on Communications and Radio Science into the 21st Century*, Dublin, 28-29 March 2012.

4. P. J. Marraccini, C. Baxley, and N. A. Riza, "Digital micromirror device-based robust object boundary mapping sensor," *Proc. SPIE Vol. 8026: SPIE Security Defense and Sensing International Conf. Photonic Applications for Aerospace, Transportation, and Harsh Environment II*, Edited by A. A. Kazemi, B. Kress, E. Y. Chan, N. A. Riza, and L. U. Kempen, 80260C, 25-29 April 2011.

5. P. J. Marraccini and N. A. Riza, “Multimode laser beam characterization using agile digital-analog photonics,” *Proc. SPIE Vol. 8026: SPIE Security Defense and Sensing International Conf. Photonic Applications for Aerospace, Transportation, and Harsh Environment II*, Edited by A. A. Kazemi, B. Kress, E. Y. Chan, N. A. Riza, and L. U. Kempen, 80260E, 25-29 April 2011.

6. P. J. Marraccini and N. A. Riza, “High resolution wide dynamic range distance sensor using spatial signal processing,” *Proc. SPIE Vol. 8026: SPIE Security Defense and Sensing International Conf. Photonic Applications for Aerospace, Transportation, and Harsh Environment II*, Edited by A. A. Kazemi, B. Kress, E. Y. Chan, N. A. Riza, and L. U. Kempen, 80260D, 25-29 April 2011.

7. N. A. Riza, M. Sheikh, and P. J. Marraccini, “Laser Beam Characterization using Agile Digital-Analog Photonics” Proc. SPIE 7675, 767508, *Photonics in the Transportation Industry: Auto to Aerospace III*,5-9 April 2010.

8. N. A. Riza and P. J. Marraccini, “Broadband Fiber-Optic 1x2 Switch Using an Electrically Controlled Liquid Lens” *Proc. SPIE 7675, 76750M Photonics in the Transportation Industry: Auto to Aerospace III*,5-9 April 2010.

OTHER PUBLICATIONS

1. P. J. Marraccini, “Faster wireless for your home and beyond – smart optical wireless communication,” *The Boolean*, Vol. 3, pp. 57-62, October 2012.
   http://publish.ucc.ie/boolean/2012/00/Marraccini/13/en

LIST OF ABBREVIATIONS

λ	Wavelength
π	Pi
ω	Angular Frequency (Radians per Second)
Ω	Ohm
1D	One-Dimension, One-Dimensional
2D	Two-Dimensions, Two-Dimensional
3D	Three-Dimensions, Three -Dimensional
AC	Alternating Current
AO	Acousto-Optic
AOD	Acouto-Optic Device
AOS	Agile Optical System
AOTF	Acousto-optic Tunable Filter
AR	Anti-Reflection
BDP	Beam Displacement Prism
BS	Beam Splitter
C	Circulator
CCD	Charge Coupled Device
CL	Cylindrical Lens
CMOS	Complementary Metal-Oxide-Semiconductor
CP	Control Processor
CREOL	The College of Optics and Photonics at UCF
dB	Decibel
DC	Direct Current
DE	Diffraction Efficiency

DF	Diffuse
DIF	Diffuser
DLP	Digital Light Processing
DMD	Digital Micro-Mirror Device
DR	Dynamic Range
DWDM	Dense Wavelength Division Multiplexed
EDFA	Erbium Doped Fiber Amplifier
ECVFL	Electronically Controlled Variable Focus Lens
EMI	Electro-Magnetic Interference
ESA	Electrical Spectrum Analyzer
Eq.	Equation
f	Frequency (Hertz), Focal Length
F	Focal Length
Fig.	Figure
FL	Fiber Lens
FO	Fiber-optic
fps	Frames per Second
FWHM	Full-Width at Half-Maximum
GHz	Giga-Hertz
GRIN	Graded Refractive Index
HeNe	Helium-Neon
HWP	Half Wave Plate
Hz	Hertz
IF	Interference Filters
IOC	Integrated Optic Combiner

IR	Infrared
kHz	Kilo-Hertz
LC	Liquid Crystal
LCD	Liquid Crystal Display, Liquid Crystal Device
LD	Laser Diode
LED	Light Emitting Diode
LOS	Line-of-Sight
LS	Laser Source
LSD	Laser Scanning Display
LWIR	Long Wave Infra-Red
m	Meter
M	Mirror
M_{xy}	Scanning Mirror in xy Plane
MEMS	MicroElectroMechanical Systems
MHz	Mega-Hertz
NIR	Near Infra-Red
NL	Negative Lens
OA	Optical Amplifier
OE	Optical Equipment
OPR	Optical Power Ratio
OSA	Optical Spectrum Analyzer
PBS	Polarization Beam Splitter
PC	Polarization Controller
PCX	Plano Convex
PD	Photo-Detector

PDL	Polarization Dependent Loss
POF	Plastic Optical Fiber
Q	Quarter Wave Plate
QWP	Quarter Wave Plate
R	Receiver
Ref.	Reference
RF	Radio Frequency
RMS	Root Mean Squared
s	Second
S	Spherical Lens, Scatter
SA	Spectrum Analyzer
SLM	Spatial Light Modulator
SMF	Single Mode Fiber
SMP	Spatially Multiplexed Processing
SNR	Signal to Noise Ratio
SWIR	Short Wave Infra-Red
T	Transmitter
TE	Transverse Electric, Test Equipment
TEM	Transverse Electromagnetic
TF	Tunable Filter
TI	Texas Instruments, Inc.
TNLC	Twisted Nematic Liquid Crystal
TL	Tunable Laser
TM	Transverse Magnetic
T/R	Transmitter/Receiver

UCC	University College Cork, National University Ireland – Cork
UCF	University of Central Florida
UV	Ultra-Violet
VAM	Value Added Module
VBG	Volume Bragg Grating
VC	Voltage Controller
VLSI	Very Large Scaled Integrated
VOA	Variable Optical Attenuator
VFOA	Variable Fiber Optical Attenuator
VPDL	Variable Photonic Delay Line
WDM	Wavelength Division Multiplexing
XGA	Extended Graphics Array (Graphics standard that has 1024 x 768 pixels)

LIST OF FIGURES

REFERENCES

[1] S. Sumriddetchkajorn and N. A. Riza, "Micro-Electromechanical System-Based Digitally Controlled Optical Beam Profiler," *Applied Optics*, vol. 41, no. 18, pp. 3506-3510, June 2002.

[2] N. A. Riza and M. J. Mughal, "Optical Power Independent Optical Beam Profiler," *Optical Engineering*, vol. 43, no. 4, pp. 793-797, April 2004.

[3] N. A. Riza and M. J. Mughal, "An Approach Towards the Holy Grail in All-Optical Circuit Switching: The Monster All-Optical Crossconnect," in *Proc SPIE vol 5260*, USA, Jan. 1 2003, pp. 33-40.

[4] S. K. Nayar, V. Branzoi, and T. E. Boult, "Programmable Imaging Using a Digital Micromirror Array," in *Proceedings of the 2004 IEEE Computer Society Conference on Computer Vision and Pattern Recognition (CVPR)*, Washington D.C. USA, June 27th-July 2nd 2004, pp. 436-443.

[5] S. Sumriddetchkajorn, *Fiber-Optic Beam Control Systems using MicroElectroMechanical Systems (MEMS)*, Nabeel A. Riza, Ed. Orlando, FL, USA: University of Central Florida, 2000, Ph. D. Dissertation.

[6] F. N. Ghauri, *Hybrid Photonic Signal Processing*, Nabeel A. Riza, Ed. Orlando, FL, USA: University of Central Florida, 2007, Ph. D. Dissertation.

[7] M. A. Sheikh, *Silicon Carbide and Agile Optics Based Sensors for Power Plant Gas Turbines, Laser Beam Analysis and Biomedicine*, Nabeel A. Riza, Ed. Orlando, FL, USA: University of Central Florida, 2009, Ph. D. Dissertation.

[8] S. A. Reza, *Micro-Electro-Mechanical Systems (MEMS) and Agile Lensing-Based Modules for Communications, Sensing and Signal Processing*, Nabeel A. Riza, Ed. Orlando, FL, USA, 2010, Ph. D Thesis.

[9] N. A. Riza, "High-Optical-Isolation Low-Loss Moderate-Switching-Speed Nematic Liquid-Crystal Optical Switch," *Optics Letters*, vol. 19, no. 21, pp. 1780-1782, Nov. 1994.

[10] S. A. Khan, *Liquid Crystal Optics for Communications, Signal Processing and 3-D Microscopic Imaging*, Nabeel A. Riza, Ed. Orlando, FL, USA: University of Central Florida, 2005, Ph. D. Dissertation.

[11] J. N. Mait, "A History of Imaging: Revisiting the Past to Chart the Future," *Optics and Photonics News*, vol. 17, no. 2, pp. 22-27, Feb. 2006.

[12] T. Wedgewood, "An Account of a Method of Copying Paintings Upon Glass and of Making Profiles by the Agency of Light upon Nitrate of Silver, invented by T. Wedgwood Esq., with Obersvations by H. Davy," *Journals of the Royal Institution*, vol. i, p. 170, 1802.

[13] A. Davenport, *The History of Photography: An Overview*, 2nd ed. Albuquerque, NM, USA: The University of New Mexico Press Printing, 2000.

[14] R. V. Jenkins, "Technology and the Market: George Eastman and the Origins of Mass Amateur Photography," *Technology and Culture*, vol. 16, no. 1, pp. 1-19, Jan. 1975.

[15] H. Iams and A. Rose, "Television Pickup Tubes with Cathode-Ray Beam Scanning," *Proceedings of the Institute of Radio Engineers*, vol. 25, no. 8, pp. 1048-1070, Aug. 1937.

[16] M. Knoll and F. Schroeter, *Physics Z*, vol. 88, no. 9, p. 330, 1937.

[17] H. Miller and J. W. Strange, "The Electrical Reproduction of Images by the Photoconductive Effect," *Proceedings of the Physical Society*, vol. 50, no. 3, pp. 374-384, May 1938.

[18] M. Riordan and L. Hoddeson, "The Origins of the pn Junction," *IEEE Spectrum*, vol. 34, no. 6, pp. 46-51, June 1997.

[19] W. S. Boyle and G. E. Smith, "Charge Coupled Semiconductor Devices," *Bell Systems Technical Journal*, vol. 49, pp. 587-593, April 1970.

[20] S. K. Mendis, R. H. Nixon, and E. R. Fossum, "Design of a Low-Ligh-Level Image Sensor with On-Chip Sigma-Delta Analog-to-Digital Conversion," in *Proc. of SPIE vol. 1900*, July 1993, pp. 31-39.

[21] S. K. Mendis, S. E. Kemey, and E. R. Fossum, "A 128×128 CMOS Active Pixel Image Sensor for Highly Integrated Imaging Systems," in *Technical Digest of the IEEE International Electron Devices Meeting (IEDM)*, Washington D.C. USA, Dec. 5-8 1993, pp. 583-586.

[22] K. Murari, R. Etienne-Cummings, N. Thakor, and G. Cauwenberghs, "Which Photodiode to Use: A Comparison of CMOS-Compatible Structures," *IEEE Sensors Jounal*, vol. 9, no. 7, pp. 752-760, July 2009.

[23] V. N. Selivanov, V. N. Govorov, A. S. Titov, and V. P. Chemodanov, "Lunar Station Television Camera," Jet Propulsion Laboratory (JPL), 1968.

[24] S. J. Katzberg, F. O. Huck, and S. D. Wall, "Photo-sensor Aperture Shaping to

Reduce Aliasing in Optical-Mechanical Line-Scan Imaging Systems," *Applied Optics*, vol. 12, no. 5, pp. 1054-1060, May 1973.

[25] M. Sheikh and N. A. Riza, "Motion-Free Hybrid Design Laser Beam Propagation Analyzer Using a Digital Micro-Mirror Device and a Variable Focus Liquid Lens," *Applied Optics*, vol. 49, no. 16, pp. D6-D11, January 2010.

[26] P. J. Marraccini and N. A. Riza, "Multimode Laser Beam Analyzer Instrument using Electrically Programmable Optics," *AIP Review of Scientific Instruments*, vol. 82, no. 12, pp. 123107-1 to 1230107-6, Dec. 2011.

[27] N. A. Riza, S. A. Reza, and P. J. Marraccini, "Digital Micro-Mirror Device-Based Broadband Optical Image Sensor for Robust Imaging Applications," *Optics Communications*, vol. 284, no. 1, pp. 103-111, January 2011.

[28] Texas Instruments Inc., "Laser Power Handling for DMDs," Dallas, TX, USA, White Paper DLPA027, 2012.

[29] N. A. Riza, P. J. Marraccini, and C. R. Baxley, "Data Efficient Digital Micromirror Device-Based Image Edge Detection Sensor using Space-Time Processing," *IEEE Sensors Journal*, vol. 12, no. 5, pp. 1043-1047, May 2012.

[30] A. G. Bell, "Upon the Production and Reproduction of Sound by Light," *Journal of the Society of Telegraph Engineers*, vol. 9, no. 34, pp. 404-426, Aug. 1880.

[31] T. K. Sarkar, R. J. Mailloux, A. A. Oliner, M. Salazar-Palma, and D. L. Sengupta, *History of Wireless*, Kai Cheng, Ed. New Jersey USA: John Wiley & Sons, 2006.

[32] F. R. Gfeller and U. H. Bapst, "Wireless In-House Data Communication via Diffuse Infrared Radiation," *Proceedings of the IEEE*, vol. 67, no. 11, pp. 1474–1486, Nov. 1979.

[33] C. S. Yen and R. D. Crawford, "The Use of Directed Optical Beams in Wireless Computer Communication," in *IEEE Global Communications Conference (GlobeCom)*, New Orleans USA, December 2-5 1985, pp. 1181-1985.

[34] Y. Nakata, J. Kashio, T. Kojima, and T. Noguchi, "In-House Wireless Communication System using Infrared Radiation," in *Proc. of the 7th International Conference on Computer Communications*, Sydney Australia, 1984, pp. 333-337.

[35] J. M. Kahn and J. R. Barry, "Wireless Infrared Communications," *Proceedings of the IEEE*, vol. 85, no. 2, pp. 265-298, Feb. 1997.

[36] S. Miyamoto, Y. Hirayama, and N. Morinaga, "Indoor Wireless Local Area Network System using Infrared and Radio Communications," in *Fifth Asia-Pacific Conference on Communications and Fourth Optoelectronics and Communications Conference vol. 1*, Beijing China, Oct. 18- 22 1999, pp. 790-793.

[37] N. A. Riza, "Reconfigurable Optical Wireless," in *IEEE Lasers and Electro-Optics Society (LEOS) Annual Meeting vol. 1*, San Francisco USA, Nov. 8-9 1999, pp. 70-71.

[38] G. Yun and M. Kavehrad, "Spot Diffusing and Fly-Eye Receivers for Indoor Infrared Wireless Communications," in *IEEE Intl. Conference on Selected Topics in Wireless Communications*, Vancouver Canada, June 25-26 1992, pp. 262-265.

[39] A. G. Al-Ghamdi and J. M. H. Elmirghani, "Spot Diffusing Technique and Angle Diversity Performance for High Speed Indoor Diffuse Infra-Red Wireless Transmission," *IEE Proceedings - Optoelectronics*, vol. 151, no. 1, pp. 46-52, Feb. 2004.

[40] A. Mahdy and J. S. Deogun, "Wireless Optical Communications: A Survey," in *IEEE Wireless Communications and Networking Conference (WCNC) vol. 4*, Atlanta USA, March 21-25 2004, pp. 2399-2404.

[41] R. J. Green, H. Joshi, M. D. Higgins, and M. S. Leeson, "Recent Developments in Indoor Optical Wireless Systems," *IET Communications*, vol. 2, no. 1, pp. 3-10, 2008.

[42] H. Elgala, R. Mesleh, and H. Haas, "Indoor Optical Wireless Communication: Potential and State-of-the-Art," *IEEE Communications Magazine*, vol. 49, no. 9, pp. 56-62, Sept. 2011.

[43] D. C. O'Brien et al., "Visible Light Communications: Challenges and Possibilities," in *IEEE 19th International Symposium on Personal, Indoor and Mobile Radio Communications (PIMRC)*, Cannes France, Sept. 15-18 2008, pp. 1-5.

[44] Y. Tanaka, S. Haruyama, and M. Nakagawa, "Wireless Optical Transmissions with White Colored LED for Wireless Home Links," in *The 11th IEEE International Symposium on Personal, Indoor and Mobile Radio Communications vol. 2*, London UK, Sept. 18-21 2000, pp. 1325-1329.

[45] Q. Zhao and B. M. Sadler, "A Survey of Dynamic Spectrum Access [Signal Processing, Networking, and Regulatory Policy]," *IEEE Signal Processing Magazine*, vol. 24, no. 3, pp. 79-89, May 2007.

[46] M. Sherman, A. N. Mody, R. Martinez, C. Rodriguez, and R. Reddy, "IEEE Standards Supporting Cognitive Radio and Networks, Dynamic Spectrum Access, and Coexistence," *IEEE Communications Magazine*, vol. 46, no. 7, pp. 72-79, July 2008.

[47] P. Leaves et al., "Dynamic Spectrum Allocation in Composite Reconfigurable Wireless Networks," *IEEE Communications Magazine*, vol. 42, no. 5, pp. 72-81, May 2004.

[48] W. Webb, "Dynamic Spectrum Access is the Solution: What's the Problem?," *Journal of Signal Processing Systems*, vol. 69, no. 1, pp. 5-9, Oct. 2012.

[49] M. van Buren and N. A. Riza, "Foundations for Low-Loss Fiber Gradient-Index Lens Pair Coupling with the Self-Imaging Mechanism," *Applied Optics*, vol. 42, no. 3, pp. 550-565, Jan. 2003.

[50] P. J. Marraccini, "Faster Wireless for Your Home and Beyond – Smart Optical Wireless Communication," *The Boolean*, vol. 3, p. 57062, Oct. 2012, http://publish.ucc.ie/boolean/2012/00/Marraccini/13/en.

[51] P. J. Marraccini and N. A. Riza, "Power Smart In-door Optical Wireless Link Design," *Journal of the European Optical Society - Rapid Publications (JEOS:RP) [Online]*, vol. 6, pp. 11054, https://jeos.org/index.php/jeos_rp/article/view/11054, Dec. 2011.

[52] N. A. Riza and P. J. Marraccini, "Broadband 2x2 Free-Space Switch Using Electronically Controlled Liquid Lenses," *Optics Communciations*, vol. 283, no. 9, pp. 1711-1714, May 2010.

[53] Joshua Yumibe, *Moving Color: Early Film, Mass Culture, and Modernism*. USA: Rutgers University Press, 2012.

[54] E. J. Muybridge, "Picture-Feeding Device for Magic Laterns," 251,127, December 20, 1881.

[55] N. A. Riza and P. J. Marraccini, "Smart Two-Dimensional Laser-Based Display," *IEEE Journal of Display Technology*, vol. 7, no. 2, pp. 90-95, Feb. 2011.

[56] H. Kogelnik and T. Li, "Laser Beams and Resonators," *Applied Optics*, vol. 5, no. 10, pp. 1550-1567, October 1966.

[57] M. W. Sasnett, "Propagation of Multimode Laser Beams-the M2 Factor," in *The Physics and Technology of Laser Resonators*, D. R. Hall and P. E. Jackson, Ed. New York, NY, USA: Taylor & Francis Group, 1989, ch. 9, pp. 132-142.

[58] A. E. Siegman, "How to (Maybe) Measure Laser Beam Quality," in *Vol. 17 of OSA Trends in Optics and Photonics*, Washington D.C., 1998, pp. 184-199.

[59] P. A. Bélanger, "Beam Propagation and the ABCD Ray Matrices," *Optics Letters*, vol. 16, no. 4, pp. 196-198, February 1991.

[60] T. F. Johnston, "Beam Propagation (M2) Measurements Made as Easy as it Gets: The Four Cuts Method," *Applied Optics*, vol. 37, no. 21, pp. 4840-4850, July 1998.

[61] Jr., T. F. Johnston and M. W. Sasnett, "Apparatus for Measuring the Mode Quality of a Laser Beam," 5,214,485, May 25, 1993.

[62] A. E. Siegman and S. W. Townsend, "Output Beam Propagation and Beam Quality from a Multimode Stable-Cavity Laser," *IEEE Journal of Quantum Electronics*, vol. 29, no. 4, pp. 1212-1217, April 1993.

[63] W. Li et al., "Matrix Formulation of the Beam Quality of the Hermite-Gaussian Beam," *Laser Physics*, vol. 19, no. 3, pp. 455-460, March 2009.

[64] O. Mendoza-Yero, "Effects of Off-Axis Laser Beam Propagation on Beam Parameters," in *Proc. SPIE vol. 5622, 5th Iberoamerican Meeting on Optics and 8th Latin American Meeting on Optics, Lasers, and Their Applications*, Porlamar, Venezuala, October 21, 2004, pp. 1094-1099.

[65] M. Sheikh, P. J. Marraccini, and N. A. Riza, "Laser Beam Characterization using Agile Digital-Analog Photonics," in *Proc. SPIE vol. 7675, SPIE Defense Security and Sensing*, Orlando USA, 2010, pp. 767508-01 - 767508-06.

[66] N. A. Riza, "Digital Optical Beam Profiler," 6,922,233, July 26, 2005.

[67] N. A. Riza and F. N. Ghauri, "Super Resolution Hybrid Analog-Digital Optical Beam Profiler Using Digital Micro-Mirror Device," *IEEE Photonics Technology Letters*, vol. 17, no. 7, pp. 1492-1494, July 2005.

[68] N. A. Riza and M. J. Mughal, "Digital Optical Beam Profiler," 7,092,079, August 15, 2006.

[69] M. Gentili and N. A. Riza, "Wide Aperture No Moving Parts Optical Beam Profiler Using Liquid Crystal Displays," *Applied Optics*, vol. 46, no. 4, pp.

506-512, Feb. 2007.

[70] M. Sheikh and N. A. Riza, "Demonstration of Pinhole Laser Beam Profiling Using a Digital Micromirror Device," *IEEE Photonic Technology Letters*, vol. 21, no. 10, pp. 666-668, May 2009.

[71] Coherent Inc., ModeMaster PC M2 Beam Propagation Analyzer, 2011, Datasheet.

[72] "Lasers and Laser-Related Equipment — Test Methods for Laser Beam Widths, Divergence Angles and Beam Propagation Ratios," International Standards Organization, Geneva Switzerland, ISO/TC 172/SC9/WG1, ISO/DIS 11146, 2005.

[73] A. E. Siegman, How to (Maybe) Measure Laser Beam Quality, 1997, Tutorial presentation at the OSA Annual Meeting, Long Beach, California.

[74] T. Fang, X. Ye, J. Niu, and J. Xu, "Definition and Measurement of the Beam Propagation Factor M2 for Chromatic Laser Beams," *Chinese Optics Letters*, vol. 4, no. 10, pp. 586-588, October 2006.

[75] Q. Cao and X. Deng, "Spatial Parametric Characterization of General Polychromatic Light Beams," *Optics Communications*, vol. 142, no. 1-3, pp. 135-145, October 1997.

[76] P. M. Mejías and R. Martínez-Herrero, "Time-Resolved Spatial Parametric Beam Characterization of Pulsed Light Beams," *Optics Letters*, vol. 20, no. 7, pp. 660-662, April 1995.

[77] C. Paré and P. A. Bélanger, "Propagation Law and Quasi-Invariance Properties of the Truncated Second-Order Moment of a Diffracted Laser Beam," *Optics Communications*, vol. 123, no. 4-6, pp. 679-693, February 1996.

[78] Varioptic , Model Arctic 320 Liquid Lens Technical Datasheet: Optical and Opto-mechanical Data, 2006, Datasheet from Varioptic SA, Lyon, France..

[79] P. J. Marraccini and N. A. Riza, "Multimode Laser Beam Characterization using Agile Digital-Analog Photonics," in *Proc. SPIE vol. 8026, SPIE Defense Security and Sensing*, Orlando USA, April 25th 2011, pp. 80260E-1 - 80260E-4.

[80] W. S. Boyle and G. E. Smith, "Charge Coupled Semiconductor Devices," *Bell System Technical Journal*, vol. 49, pp. 587-593, April 1970.

[81] J. Janesick and G. Putnam, "Developments and Applications of High-

Performance CCD and CMOS Imaging Arrays," *Annual Review of Nuclear and Particle Science*, vol. 53, pp. 263-300, December 2003.

[82] Y. Bai et al., "Development of Hybrid CMOS Visible Focal Plane Arrays at Rockwell," in *Proc. SPIE vol. 4028*, Orlando USA, April 24th 2000, p. 174.

[83] D. E. Groom et al., "Quantum Efficiency of a Back-illuminated CCD Imager: An Optical Approach," in *Proc. SPIE vol. 3649*, San Jose USA, January 23rd 1999, pp. 80-90.

[84] Ophir-Spiricon Inc., NIR Camera Data Sheet, 2009.

[85] J. B. Barton, R. F. Cannata, and S. M. Petronio, "InGaAs NIR Focal Plane Arrays for Imaging and DWDM Applications," in *Proc. SPIE vol. 4721*, Orlando USA, April 1st 2002, pp. 37-47.

[86] J. S. Pearlman et al., "Hyperion, a Space-Based Imaging Spectrometer," *IEEE Transactions on Geoscience and Remote Sensing*, vol. 41, no. 6, pp. 1160-1173, Jun 2003.

[87] A. Rogaliski, Ed., *SPIE Milestone Series Volume MS 149 Selected Papers of Semiconductor Infrared Detectors*. USA: SPIE - The International Society for Optical Engineering, 1992.

[88] L. J. Kozlowski et al., "Recent Advances in Staring Hybrid Focal Plane Arrays: Comparison of HgCdTe, InGaAs, and GaAs/AlGaAs Detector Technologies," in *Proc. SPIE vol. 2274*, San Diego USA, July 24th 1994, pp. 93-116.

[89] A. I. D'souza et al., "VSWIR to VLWIR MBE Grown HgCdTe Material and Detectors for Remote Sensing Applications," *Journal of Electronic Materials*, vol. 26, no. 6, pp. 656-661, June 1997.

[90] K. Wardell, A. Jakobsson, and G. E. Nilsson, "Laser Doppler Perfusion Imaging by Dynamic Light Scattering," *IEEE Transactions on Biomedical Engineering*, vol. 40, no. 4, pp. 309-316, Apr. 1993.

[91] R. A. Hicks, V. T. Nasis, and T. P. Kurzweg, "Programmable Imaging with Two-Axis Micromirrors," *Optics Letters*, vol. 32, no. 9, pp. 1066-1068, May 2007.

[92] H. Grüger et al., "Pushbroom NIR Hyperspectral Imager using MOEMS Scanning Grating Chips," in *Proc. of SPIE vol. 6887*, San Jose USA, Jan. 19th 2008, pp. 68870E-68870E-9.

[93] N. A. Riza and Y. Huang, "High Speed Optical Scanner for Multi-Dimensional Beam Pointing and Acquisition," in *Proc. IEEE Lasers and Electro-Optics Society (LEOS) 12th Annual Meeting*, San Franscisco USA, Nov. 8th-11th 1999, pp. 184-185.

[94] N. A. Riza, "Multiplexed Optical Scanner Technology," 6,687,036, Feb. 3, 2004.

[95] N. A. Riza, "Photonically Controlled Ultrasonic Arrays: Scenarios And Systems," in *Proc. IEEE Ultrasonics Symposium vol. 2*, San Antonio USA, Nov 3rd-6th 1996, pp. 1545-1550.

[96] G. J. Tearney, R. H. Webb, and B. E. Bouma, "Spectrally Encoded Confocal Microscopy," *Optics Letters*, vol. 23, no. 15, pp. 1152-1154, Aug. 1998.

[97] N. A. Riza and Z. Yaqoob, "High Speed Fiber-Optic Probe for Dynamic Blood Analysis Measurements," in *Proc. SPIE vol. 4163*, Amsterdam Netherlands, July 4th 2000.

[98] Z. Yaqoob, A. A. Rizvi, and N. A. Riza, "Free-Space Wavelength-Multiplexed Optical Scanner," *Applied Optics*, vol. 40, no. 35, pp. 6425-6438, Dec. 2001.

[99] G. J. Tearney, M. Shishkov, and B. E. Bouma, "Spectrally Encoded Miniature Endoscopy," *Optics Letters*, vol. 27, no. 6, pp. 412-414, March 2002.

[100] Z. Yaqoob, M. Arain, and N. A. Riza, "High-Speed Two-Dimensional Laser Scanner Based on Bragg Gratings Stored in Photothermorefractive Glass," *Applied Optics*, vol. 42, no. 26, pp. 5251-5262, Sept. 2003.

[101] Z. Yaqoob and N. A. Riza, "High-Speed Scanning Wavelength-Multiplexed Fiber-Optic Sensors for Biomedicine," in *Proc. IEEE Sensors 2002 vol. 1*, Orlando USA, Nov. 7th 2002, pp. 325-330.

[102] K. Goda, K. K. Tsia, and B. Jalali, "Amplified Dispersive Fourier-Transform Imaging for Ultrafast Displacement Sensing and Barcode Reading," *Applied Physics Letters*, vol. 93, no. 13, p. 131109, October 2008.

[103] K. Goda, K. K. Tsia, and B. Jalali, "Serial Time-Encoded Amplified Imaging for Real-Time Observation of Fast Dynamic Phenomena," *Nature*, vol. 458, pp. 1145-1149, April 2009.

[104] K. K. Tsia, K. Goda, D. Capewell, and B. Jalali, "Performance of Serial Time-Encoded Amplified Microscope," *Optics Express*, vol. 18, no. 10, pp. 10016-10028, May 2010.

[105] D. Takhar et al., "A New Compressive Imaging Camera Architecture Using Optical-Domain Compression," in *Proc. SPIE vol. 6065*, San Jose USA, 2006, p. 606509.

[106] N. A. Riza, "Agile Optical Image Sensing, Control, and Measurement Modules," Patent Pending.

[107] P. Yeh and C. Gu, *Optics of Liquid Crystal Displays*, 2nd ed. Hoboken, USA: John Wiley & Sons, 2010.

[108] M. Irani and S. Peleg, "Motion Analysis for Image Enhancement: Resolution, Occlusion and Transparency," *Journal of Visual Communication and Image Representation*, vol. 4, no. 4, pp. 324-335, Dec. 1993.

[109] N. A. Riza and M. Sheikh, "Liquid Lens Confocal Microscopy with Advanced Signal Processing for Higher Resolution 3D Imaging," in *Proc. SPIE vol. 7258*, Lake Buena Vista USA, Feb. 7th 2009, p. 725848.

[110] N. A. Riza and S. A. Reza, "Noncontact Distance Sensor Using Spatial Signal Processing," *Optics Letters*, vol. 34, no. 4, pp. 434-436, Feb. 2009.

[111] N. A. Riza and S. A. Reza, "Smart Agile Lens Remote Optical Sensor for Three-Dimensional Object Shape Measurements," *Applied Optics*, vol. 49, no. 7, pp. 1139-1150, March 2010.

[112] N. A. Riza, "Advances in Hybrid Optics Physical Sensors for Extreme Environments," in *Proc. SPIE vol. 7726*, Brussels Belgium, April 12th 2010, pp. 77260L-77260L-12.

[113] D. Ziou and S. Tabbone, "Edge Detection Techniques - An Overview," *International Journal of Pattern Recognition and Image Analysis*, vol. 8, no. 4, pp. 537-539, 1998.

[114] D. Mumford and J. Shah, "Boundary Detection by Minimizing Functionals, I," in *IEEE Conference on Computer Vision and Pattern Recognition*, San Fransciso USA, 1985, pp. 22-26.

[115] L. Fan, P. L. Von Behren, and T. S. Sumanaweera, "Border Detection for Medical Imaging," 7,022,073, April 4, 2006.

[116] J. S. Amidei, "Image Boundary Detection for a Scanned Image," 5,995,661, Nov. 30, 1999.

[117] W. Xiong, "Shot Boundary Detection," 7,123,769, Oct. 17, 2006.

[118] X. Zhang and E. Y. Lam, "Edge Detection of Three-Dimensional Objects by Manipulating Pupil Functions in an Optical Scanning Holography System," in *Proc. IEEE 17th International Conference on Image Processing*, Hong Kong China, Sept 26-29, 2010, pp. 3661-3664.

[119] D. Stoppa, A. Simoni, A. Baschirotto, M. Vatteroni, and A. Sartori, "A 120-dB Dynamic Range CMOS Image Sensor with Programmable Power Responsivity," in *Proceedings of the 32nd European Solid-State Circuits Conference*, Montreux Switzerland, Sept. 19-21 2006, pp. 420-423.

[120] E. J. Candès, J. Romberg, and T. Tao, "Robust Uncertainty Principles: Exact Signal Reconstruction from Highly Incomplete Frequency Information," *IEEE Transactions on Information Theory*, vol. 52, no. 2, pp. 389-509, Feb. 2006.

[121] D. L. Donoho, "Compressed Sensing," *IEEE Transactions on Information Theory*, vol. 52, no. 4, pp. 1289-1306, April 2006.

[122] Texas Instruments, Inc., "DMD Discovery 1100 Chip Set," Texas, Datasheet on DLP Technology 2004.

[123] P. J. Marraccini, C. Baxley, and N. A. Riza, "Digital Micromirror Device-Based Robust Object Boundary Mapping Sensor," in *Proc. SPIE vol. 8026*, Orlando USA, April 25 2011.

[124] N. A. Riza, "Switchboard in the Sky: Freespace Optics Platform for Communications and Processing," in *IEEE Lasers and Electro-Optics Society (LEOS) Annual Meeting vol. 2*, Orlando USA, Dec. 3-4 1998, pp. 211--212.

[125] N. A. Riza and S. A. Khan, "Ultra-Low Loss Laser Communications Technique using Smart Beamforming Optics," *Optics Communications*, vol. 257, no. 2, pp. 225-246, Jan. 2006.

[126] N. A. Riza and S. A. Khan, "Erratum to “Ultra-Low Loss Laser Communications Technique using Smart Beamforming Optics” [Opt. Commun. 257 (2) (2006) 225–246]," *Optics Communications*, vol. 259, no. 2, pp. 888-890, March 2006.

[127] J. Grubor, S. Randel, K. -D. Langer, and J. W. Walewski, "Bandwidth-Efficient Indoor Optical Wireless Communications with White Light-Emitting Diodes," in *Proceedings for the 6th International Symposium on Communication Systems, Networks and Digital Signal Processing*, Graz Austria, July 25 2008, pp. 165-169.

[128] Y. Tanaka, T. Komine, S. Haruyama, and M. Nakagawa, "Indoor Visible Light Data Transmission System Utilizing White LED Lights," *IEICE Transactions*

on Communications, vol. E86-B, no. 8, pp. 2440–2454, Aug. 2003.

[129] J. Vučić, C. Kottke, S. Nerreter, K. -D. Langer, and J. W. Walewski, "513 Mbit/s Visible Light Communications Link Based on DMT-Modulation of a White LED," *IEEE Journal of Lightwave Technology*, vol. 28, no. 24, pp. 3512-3518, Dec. 2010.

[130] J. Alwan, "Eye Safety and Wireless Optical Networks," AirFiber, Inc., April 24 2001.

[131] J. T. Verdeyen, *Laser Electronics*, 3rd ed., N. Holonyak Jr., Ed. New York USA: Prentice Hall, 1994.

[132] J. Grubor, O. C. Gaete Jamett, J. W. Walewski, S. Randel, and K. -D. Langer, "High-Speed Wireless Indoor Communication via Visible Light," in *Proceedings of the Conference on Broadband Coverage in Germany – Diversity for All, ITG-Fachbericht 198*, (VDE-Verlag, Berlin, 2007), 2007, pp. 203-208.

[133] P. Marraccini and N. Riza, "Reconfigurable Visible Wireless Optical Link for Indoor Applications," in *Royal Irish Academy Research Colloquium on Communications and Radio Science into the 21st Century, Proceedings*, Dublin Ireland, March 28-29 2012.

[134] N. A. Riza and P. J. Marraccini, "Power Smart In-Door Optical Wireless Link Applications," in *The IEEE 8th International Wireless Communications and Mobile Computing (IWCMC) Conference*, Limassol Cyprus, August 26-31 2012, pp. 327-332.

[135] J. B. Carruthers and J. M. Kahn, "Modeling of Nondirected Wireless Infrared Channels," *IEEE Transactions on Communications*, vol. 45, no. 10, pp. 1260-1268, Oct. 1997.

[136] P. J. Marraccini and N. A. Riza, "Dual Mode Indoor Optical Wireless Data Link Design using Micro-Optics for Robust Energy Efficient Operation," in *European Optical Society Annual Meeting (EOSAM) Conference Digest*, Aberdeen, Sept. 25-28 2012, pp. Topical Meeting TOM 4 - Micro-Optics Paper 5888.

[137] D. R. Wisely, "A 1 Gbit/s Optical Wireless Tracked Architecture for ATM Delivery," in *IEE Colloquium on Optical Free Space Communication Links*, London, UK, 19 Feb. 1996, pp. 14/1-14/7.

[138] Firecomms Ltd. (Cork, Ireland), FS-EDLT Preliminary Product Specification “650 nm 100 Mbps Ethernet Fiber Optic Transceiver for Free Space Optical

Links”, 2011.

[139] D. J. Sterling, *Technician’s Guide to Fiber Optics*, 4th ed. Clifton Park, New York USA: Delmar, Cengage Learning, 2004.

[140] P. J. Marraccini and N. A. Riza, "Smart Multiple Modes Indoor Optical Wireless Design and Multi-Mode Light Source Smart Energy Efficient Links," *Optical Engineering*, vol. 52, no. 5, pp. 055001-1 to 055001-7, May 2013.

[141] R. A. Soref, "Low-Cross-Talk 2×2 Optical Switch," *Optics Letters*, vol. 6, no. 6, pp. 275-277, June 1981.

[142] L. R. McAdams and J. W. Goodman, "Liquid Crystal 1×N Optical Switch," *Optics Letters*, vol. 15, no. 20, pp. 1150-1152, Oct. 1990.

[143] P. Boffi, D. Piccinin, A. Tonini, A. Zappettini, and M. Martinelli, "Polarization-Independent Bidirectional Optical Switch for Communication Signals," in *Proc. SPIE vol. 4089*, Quebec City Canada, June 18 2000, pp. 297-303.

[144] D. M. Gookin, "Optical Switch using the Photorefractive and Ferroelectric Polarization Reversal," *Optics Letters*, vol. 12, no. 3, pp. 196-198, March 1987.

[145] K. Campbell et al., "A Microfluidic 2×2 Optical Switch," *Applied Physics Letters*, vol. 85, no. 25, pp. 6119-6121, Dec. 2004.

[146] D. O. Harris, "Multichannel Acousto-Optic Crossbar Switch," *Applied Optics*, vol. 30, no. 29, pp. 4245-4256, Oct. 1991.

[147] M. Yamaguchi et al., "Experimental Investigation of a Digital Free-Space Photonic Switch that Uses Exciton Absorption Reflection Switch Arrays," *Applied Optics*, vol. 33, no. 8, pp. 1337-1344, March 1994.

[148] B. Pesach et al., "Free-Space Optical Cross-Connect Switch by use of Electroholography," *Applied Optics*, vol. 39, no. 5, pp. 746-758, Feb. 2000.

[149] B. Staple and R. Roth, "MEMS-Based Noncontacting Free-Space Optical Switch," 6,701,037, March 2, 2004.

[150] B. Berge and J. Peseux, "Variable Focal Lens Controlled by an External Voltage: An Application of Electrowetting," *European Physics Journal E*, vol. 3, pp. 159-163, Dec. 2000.

[151] S. Kuiper and B. H. W. Hendriks, "Variable-Focus Liquid Lens for Miniature

Cameras," *Applied Physics Letters*, vol. 85, no. 7, pp. 1128-1130, 2004.

[152] S. A. Reza and N. A. Riza, "A Liquid Lens-Based Broadband Variable Fiber Optical Attenuator," *Optics Communications*, vol. 282, no. 7, pp. 1298-1303, April 2009.

[153] S. A. Reza and N. A. Riza, "High Dynamic Range Variable Fiber Optical Attenuator using Digital Micromirrors and Opto-Fluidics," *IEEE Photonics Technology Letters*, vol. 21, no. 13, pp. 845-847, July 2009.

[154] J. L. Jackel, S. Hackwood, and G. Beni, "Electrowetting Optical Switch," *Applied Physics Letters*, vol. 40, no. 1, pp. 4-5, Jan. 1982.

[155] R. Shamai and U. Levy, "On Chip Tunable Micro Ring Resonator Actuated by Electrowetting," *Optics Express*, vol. 17, no. 2, pp. 1116-1125, Jan. 2009.

[156] N. A. Riza and P. J. Marraccini, "Broadband Fiber-Optic 1x2 Switch Using an Electrically Controlled Liquid Lens," in *Proc. SPIE vol. 7675*, Orlando USA, April 5-9 2010.

[157] S. Yuan and N. A. Riza, "General Formula for Coupling-Loss Characterization of Single-Mode Fiber Collimators by use of Gradient-Index Rod Lenses," *Applied Optics*, vol. 38, no. 15, pp. 3214-3222, May 1999.

[158] Y. Ishii, "The World of Liquid-Crystal Display TVs – Past, Present, and Future," *IEEE Journal of Display Technology*, vol. 3, no. 4, pp. 351-360, Dec. 2007.

[159] P. F. van Kessel, L. J. Hornbeck, R. E. Meier, and M. R. Douglass, "A MEMS-Based Projection Display," *Proceedings of the IEEE*, vol. 86, no. 8, pp. 1687-1704, Aug. 1998.

[160] M. S. Brennesholtz and E. H. Stupp, *Projection Displays*, 2nd ed. Chichester, UK: John Wiley & Sons, 2008.

[161] R. Sprague et al., *"Mobile Projectors using Scanned Beam Displays" in Mobile Displays: Technology and Applications*. Chichester, UK: John Wiley & Sons, 2008, Chap. 21.

[162] W. O. Davis, R. Sprague, and J. Miller, "MEMS-Based Pico Projector Display," in *IEEE/LEOS International Conference on Optical MEMS and Nanophotonics*, Freiburg Germany, Aug. 11-14 2008, pp. 31-32.

[163] D. Lashmet, D. Baty, and M. Nichols, "A Single-Mirror Laser-Based Scanning Display Engine," *SID Information Display Magazine, Projection Displays*

Issue, vol. 24, no. 12, pp. 26-28, Dec. 2008.

[164] M. Freeman, M. Champion, and S. Madhavan, "Scanned Laser Pico Projectors: Seeing the Big Picture (with a Small Device)," *Optics and Photonics News*, vol. 20, no. 5, pp. 28-34, May 2009.

[165] J. -H. Lee et al., "Laser TV for Home Theater," in *Proc. SPIE vol. 4567*, San Jose USA, Jan 19 2002, pp. 138-145.

[166] R. A. Conant et al., "A Raster-Scanning Full-Motion Video Display Using Polysilicon Micromachined Mirrors," *Sensors and Actuators A: Physical*, vol. 83, no. 1-3, pp. 291-296, May 2000.

[167] J. Kränert, C. Deter, T. Gessner, and W. Dötzel, "Laser Display Technology," in *The 11th Annual International Worshop on Micro Electro Mechanical Systems*, Heidelberg Germany, Jan. 25-29 1998, pp. 99-104.

[168] E. Downing, L. Hesselink, J. Ralston, and R. Macfarlane, "A Three-Color, Solid-State, Three-Dimensional Display," *Science*, vol. 273, no. 5279, pp. 1185-1189, Aug. 1996.

[169] N. A. Riza, US Patent Pending.

[170] Z. Yaqoob and N. A. Riza, "Smart Free-Space Optical Interconnects and Communication Links using Agile WDM Transmitters," in *Digest of the IEEE LEOS Summer Topical Meetings*, Copper Mountain USA, July 30-Aug 1 2001.

[171] N. A. Riza and S. Yuan, "Demonstration of a Liquid-Crystal Adaptive Alignment Tweeker for High-Speed Infrared Band Fiber-Fed Free-Space Systems," *Optical Engineering*, vol. 37, no. 6, pp. 1876-1880, June 1998.

[172] N. A. Riza and M. C. DeJule, "A Novel Programmable Liquid Crystal Lens Device for Adaptive Optical Interconnect and Beamforming Applications," in *Presented at the International Conference on Optical Computing*, Edinburgh UK, Aug. 22-25 1994.

[173] N. A. Riza, "Flexible Agile Hybrid Optical-RF Antenna System for Communications and Radar," in *he IEEE 19th International Conference on Microwave Radar and Wireless Communications (MIKON) vol. 2*, Warsaw Poland, May 21-23 2012, pp. 668-673.

[174] N. A. Riza, Flexible Agile Optical-RF Antenna System, 2002, SBIR Phase 1 Contract, US Air Force Wright Labs, AF 02-233.

[175] G. P. Agrawal, *Fiber-Optic Communication Systems*, 3rd ed., Kai Cheng, Ed.

New York USA: John Wiley & Sons, 2002.

[176] N. A. Riza and M. J. Mughal, "The NU-POWER All-Digital Beam Profiler: A Powerful New Tool for Spatially Characterizing Laser Beams," in *Proc. of SPIE vol. 5260*, USA, Jan. 1 2003, pp. 87-95.

[177] E. J. Muybridge, "Improvement in the Method and Apparatus for Photographing Objects in Motion," 212,865, March 4, 1879.